Theoretical and Experimental Analysis of Adsorption in Surface-based Biosensors

Hansen, Rasmus; Hassager, Ole; Callisen, Thomas H,; Bruus, Henrik

Publication date:
2012

Theoretical and Experimental Analysis of Adsorption in Surface-based Biosensors

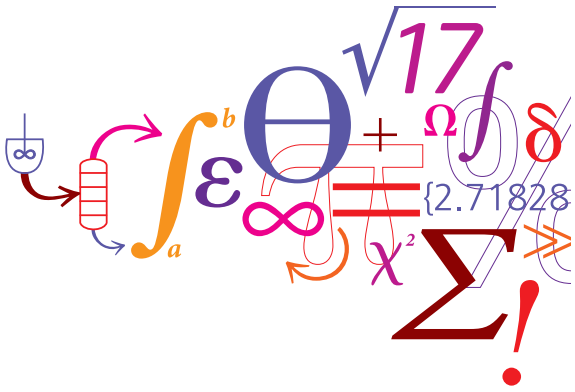

Rasmus Hansen

Ph.D. Thesis

January 2012

DTU Chemical Engineering

Department of Chemical and Biochemical Engineering

Theoretical and Experimental Analysis of Adsorption in Surface-based Biosensors

Rasmus Hansen

Department of Chemical and Biochemical Engineering

Technical University of Denmark

A thesis submitted for the degree of

Philosophiae Doctor (Ph.D.)

2012 January

DTU Chemical Engineering
Department of Chemical and Biochemical Engineering

Title of the thesis:
Theoretical and Experimental Analysis of Adsorption in Surface-based Biosensors

Author:
Rasmus Hansen
E-mail: rah@kt.dtu.dk

Address:
Department of Chemical and Biochemical Engineering
Danish Polymer Center
Technical University of Denmark
Søltofts Plads, Building 227
DK-2800 Kongens Lyngby, Denmark

Supervisors:
Ole Hassager, Professor, DTU Chemical Engineering
E-mail: oh@kt.dtu.dk

Thomas H. Callisen, Senior Manager, Novozymes A/S
E-mail: call@novozymes.com

Henrik Bruus, Professor, DTU Nanotech
E-mail: henrik.bruus@nanotech.dtu.dk

Print:
J og R Frydenberg København august 2012

ISBN 978-87-92481-75-7

Preface

This thesis is submitted in partial fulfillment of the requirements for obtaining the Ph.D. degree in chemical engineering at the Technical University of Denmark (DTU). The Ph.D. project was carried out partially at the Department of Chemical and Biochemical Engineering at DTU, and partially at Novozymes A/S, in the period January 1st 2009 - January 13st 2012.

I would like to express my gratitude to my three supervisors for their support during the project. Thanks to Lene Bjørg Cesar and Diane Falk Rasmussen at Novozymes for their careful laboratory assistance. Thanks also to my colleagues at the Danish Polymer Centre at DTU, especially Yanwei Wang with whom I have had many interesting hours, and Anders Egede Daugaard for encouraging conversations. I am also thankful to Stig Wedel at DTU Chemical Engineering for discussions on mathematical issues. I finally wish to thank my wife for indispensable support and indulgence during the project period.

The Ph.D. project has been funded by the The Danish Council for Independent Research - Technology and Production Sciences and by Novozymes A/S.

Kongens Lyngby, March 13st 2012.

Rasmus Hansen

Resumé (in Danish)

Teoretisk og eksperimentel analyse af adsorption i overfladebaserede biosensorer

Denne Ph.D. afhandling vedrører anvendelse af overflade-plasmon-resonans (SPR) spektroskopi, som er en overfladebaseret biosensorteknologi, til studier af adsorptionsdynamik. Afhandlingen indeholder eksperimentelt og teoretisk arbejde. I den teoretiske del udvikles teorien for konvektion, diffusion, og adsorption i overfladebaserede biosensorer generelt. Vi studerer transportdynamikken i en modelgeometri af en Biacore SPR sensor. Vi præsenterer en gennemgang samt en analytisk løsning til en approksimativ kvasi-stationær teori, som bliver taget hyppigt i brug i SPR litteraturen for at indfange konvektiv og diffusiv massetransport. Det dimensionsløse Damköhler tal, som naturligt parameteriserer den kvasi-stationære teori, udledes i termer af den dimensionsløse adsorptionskonstant (Biot tallet), den dimensionsløse strømningshastighed (Peclet tallet), samt modelgeometrien. Derudover udvikles og præsenteres en teoretisk to-komponent model, som er designet til at indfange kompetitiv adsorptionsdynamik af to slags adsorberende specier. Vi foretager en numerisk undersøgelse af transient dynamik, hvor vi kvantificerer fejlen ved at bruge den kvasi-stationære teori til eksperimentel datafitting, i både det kinetisk begrænsede og det konvektions-diffusions-begrænsede regime. Resultaterne tydeliggør, under hvilke betingelser den kvasi-stationære teori er pålidelig, og hvor den ikke er. Foruden det velkendte faktum at gyldighedsintervallet for teorien er begrænset under konvektions-diffusions-begrænsede betingelser, vises det, hvorledes forholdet imellem indløbskoncentrationen og den maksimale overfladekapacitet er kritisk for pålidelig brug af den kvasi-stationære teori. Vores teoretiske resultater tilvejebringer brugere af overfladebaserede biosensorer et væktøj til at korrigere adsorptionskonstanter opnået ved at fitte den kvasi-stationære teori til eksperimenter. Endelig undersøges konsekvensen af adsorption på alle overfladerne, udover sensoroverfladen, i biosensorens flowcelle. I den del af afhandlingen der vedrører eksperimentelt arbejde bruger vi en Biacore SPR sensor til at studere adsorption af lipaser på

modeloverflader der imiterer substrat, samt at studere kompetitiv adsorption af lipase og overfladeaktive molekyler (surfactant). En del af den eksperimentelle data målt under projektperioden præsenteres og diskuteres. Denne del tilvejebringer tilsyneladende kinetiske adsorptions- og desorptionkonstanter, og forsøger at give et overblik over de vigtigste elementer der udfordrer brugen af den eksperimentelle data til datadrevet teoretisk modellering. Vi fremhæver nogle vigtige betingelser som skal være opfyldt for at opnå en udførlig forbindelse mellem eksperimental data og teoretisk modellering.

Abstract

The present Ph.D. dissertation concerns the application of surface plasmon resonance (SPR) spectroscopy, which is a surface-based biosensor technology, for studies of adsorption dynamics. The thesis contains both experimental and theoretical work. In the theoretical part we develop the theory for convection, diffusion, and adsorption in surface-based biosensors in general. In particular, we study the transport dynamics in a model geometry of a Biacore SPR sensor. An approximate quasi-steady theory, which has been widely adopted in the SPR literature to capture convective and diffusive mass transport, is reviewed, and an analytical solution is provided. The important nondimensional Damköhler number, inherent in the quasi-steady theory, is derived in terms of the nondimensional adsorption coefficient (Biot number), the nondimensional flow rate (Péclet number), and the model geometry. Also, a two-component theoretical model, designed to capture competitive adsorption dynamics of two adsorbing species, is developed and presented. Transient dynamics is investigated numerically, and we quantify the error of using the quasi-steady theory for experimental data fitting in both kinetically limited and convection-diffusion-limited regimes. The results clarify the conditions under which the quasi-steady theory is reliable or not. In extension to the well known fact that the range of validity is limited under convection-diffusion-limited conditions, we also show how the ratio of the inlet concentration to the maximum surface capacity is critical for reliable use of the quasi-steady theory. Our theoretical results provide users of surface-based biosensors with a tool of correcting experimentally obtained adsorption rate constants, based on the quasi-steady theory. Finally, the consequence of adsorption on all surfaces present in the flow cell of the surface-based biosensor, in addition to the sensor surface, is investigated. In the experimental part of the thesis we use a Biacore SPR sensor to study lipase adsorption on model substrate surfaces, as well as competitive adsorption of lipase and surfactants. A part of the experimental data obtained during the project is presented and discussed. In particular, this part provides apparent kinetic adsorption/desorption rate constants, and gives an overview of the major challenges of basing theoretical modeling on this data. We emphasize the importance of some conditions, which necessarily have to be fulfilled in order

to attain a comprehensive link between the experimental data and the theoretical modeling.

Contents

List of Figures

Chapter 1

Introduction

1.1 Outline of the Ph.D. project

The present Ph.D. project was set up as a collaboration between the Technical University of Denmark (DTU) and Novozymes. The theoretical developments were primarily carried out at DTU under supervision of Professor Ole Hassager, DTU Chemical Engineering, and Professor Henrik Bruus, DTU Nanotech. All experiments analyzed during the project were designed in close collaboration with Senior Manager Thomas H. Callisen, Novozymes A/S, and were carried out with laboratory support from Lene Bjørg Cesar, and Diane Falk Rasmussen at Novozymes.

The aim of the project was to develop theoretical models of molecular transport to support interpretation of data from surface plasmon resonance (SPR) biosensor experiments. In this way, the project has been primarily data driven, and the effort put on interpreting data has been pronounced. In the majority of the project the typical working procedure was to obtain SPR data, and thereafter attempt to understand it by using theoretical calculations.

The aim of the Ph.D. project turned out to be challenging. As presented in chapter 5 the SPR experiments and the corresponding experimental protocols, albeit of good quality and at the level typically reported in peer-reviewed papers, were found not to be sufficiently developed for the pupose of forming the basis for rigorous theoretical analysis. Even though the experimental work has not yet been submitted for publication, it has been a fruitful process to link experiments and theory. The goal of combining rigorous theory with experiments on biological matter is hard, but the process of approaching that goal has implied experience and insight, which may be applied in future work. The theoretical work has spawned a manuscript submitted for publication, which concerns the

capabilities, as well as shortcomings, of a widely used model in the SPR literature.

Moreover, in addition to the Ph.D. courses followed and the teaching assistance done at DTU, I have co-authored two manuscripts written and published during the project period. Both are outside the scope of the main project defined in collaboration with Novozymes, and are therefore simply appended in the end of the dissertation.

1.2 Dissertation structure

The objective of this thesis is to provide both a general overview of the work done during the Ph.D. project period, as well as detailed descriptions of developed methods and obtained results. The main part of the thesis is directly related to the project scope of obtaining tools for better interpretation of data obtained from surface plasmon resonance (SPR) spectroscopy, with the ultimate goal of better utilization of the data in research and development.

Chapter 2: Introduction to SPR spectroscopy

This chapter provides background information related to the setup and application of SPR spectroscopy in the field of biomolecular interactions. The main principle of SPR spectroscopy and some fundamental physics related to its mode of operation are described. The chapter also provides a brief review of the use of SPR spectroscopy for interactions at lipid surfaces.

Chapter 3: Mathematical modeling of transport phenomena in surface-based biosensors

This chapter is concerned with the theory of mass transport, i.e. convection, diffusion, and adsorption in surface-based biosensors. A particular scope of the work presented in this chapter is to form a theoretical basis for analysis of data obtained from the Biacore apparatus. However, due to its fundamental and theoretical nature, the work in this chapter can be somewhat generalized to surface-based biosensors, and more broadly to similar transport problems in other technical fields.

Chapter 4: Numerical analysis

The mathematical models developed in chapter 3 are investigated numerically in a model geometry, designed to mimic the actual geometry used by Biacore in the

experimental SPR setup. A basis for physical intuition is provided by visualizing the evolution of the concentration field in the modeled geometry. This is followed by quantitative analysis and comparison of the mathematical models. Focus is on the typical quantifiers used in the application of SPR spectroscopy. The main results of this chapter have been summed up in a manuscript submitted for publication in *Langmuir*, see appendix [P1].

Chapter 5: SPR experiments of lipase adsorption

This chapter is concerned with SPR experiments. The experimental conditions and the experimental results are presented. The challenges of using the data for rigorous mathematical modeling are discussed.

Chapter 6: Concluding remarks

This chapter concludes the work. In addition to summing up the main theoretical results, some focus is on the lessons learned in relation to the SPR experiments. Some ideas for future work are presented in the end of this chapter.

1.3 Publications

Articles in peer reviewed journals written during the Ph.D.

- R. Hansen, H. Bruus, T. H. Callisen, and O. Hassager. Transient convection, diffusion, and adsorption in surface-based biosensors. Submitted to *Langmuir*, January 2012.
- O. Hassager and R. Hansen. Constitutive equations for the Doi-Edwards model without independent alignment. *Rheologica Acta*, 49(6):555-562, March 2010.
- K. H. Jensen, E. Rio, R. Hansen, C. Clanet, and T. Bohr. Osmotically driven pibe flows and their relation to sugar transport in plants. *Journal of Fluid Mechanics*, 636:371-396, April 2009.

Popular articles

- R. Hansen, T. H. Callisen, and O. Hassager. Enzymer udnytter kaos til grundig afsøgning af overflader. *Dansk Kemi* **5**. 2009. (Danish).

Conference contributions

- R. Hansen, H. Bruus, T. H. Callisen, and O. Hassager. Competitive adsorption dynamics of lipase and surfactants. *Annual Polymer Day*. DTU, Lyngby, Denmark, November 2011.

- R. Hansen, H. Bruus, T. H. Callisen, and O. Hassager. Adsorption dynamics of enzymes on substrate surfaces. *Molecular Processes at Solid Surfaces, 10th Annual Surface and Colloid Symposium*. Lund University, Sweden, November 2011.

- R. Hansen, H. Bruus, T. H. Callisen, and O. Hassager. Adsorption dynamics of globular proteins in surface-based biosensors. *Annual Polymer Day*. DTU, Lyngby, Denmark, November 2010.

- R. Hansen, H. Bruus, T. H. Callisen, and O. Hassager. Adsorption of proteins on substrate surfaces. *Annual Polymer Day*. DTU, Lyngby, Denmark, November 2009.

- R. Hansen, T. H. Callisen, and O. Hassager. Enzymer udnytter kaos til grundig afsøgning af overflader. *Novo Symposium*. January, 2009, Bagsværd, Denmark (Danish)

Chapter 2

Introduction to SPR spectroscopy

Surface plasmon resonance (SPR) spectroscopy is an advanced optical sensing method that enables label free monitoring of macromolecular interactions. The technique is now widely used in biomolecular research, medical diagnostics, food analysis, and environmental monitoring (Homola, 2008). The experimental part of this thesis investigates adsorption of a wild type and a mutant lipid-hydrolyzing enzyme to a hydrophobic surface. This was carried out using a Biacore SPR reader, which by far is the most common SPR platform (Besenicar et al., 2006). This chapter provides a general introduction to the principle of SPR spectroscopy and presents the main parts of SPR biosensors. Finally, the use of SPR for analyzing interactions between proteins and lipid surfaces is reviewed.

2.1 The overall principle of SPR

SPR sensors are used to study macromolecular interactions at the surface of a sensor chip, where so called ligand molecules have been immobilized. The overall principle of SPR is that binding of analyte molecules to the immobilized ligand changes the refractive index of the sensor chip surface, which is detected by an optical reader. SPR sensors are based on the generation of surface plasmons (SP), and a coupled light wave, at the interface between a metal surface and a dielectric substance. SPs arise when light is directed through a highly refractive medium at an incidence angle that establishes total internal reflection of the light at the metal surface. SPs propagate along the metal surface, and the electromagnetic field probes the adjacent medium, i.e. the sensor chip surface. Upon changes in the refractive index of the surface in close proximity to the metal surface, the velocity of surface plasmons changes. This change also alters the characteristics

of the coupled light wave, which is registered by the optical reader. Thus, interaction between the immobilized ligand, and the analyte molecule in solution, is monitored immediately and no tags are required.

Numerous different SPR readers are commercially available, but they all consist of: (a) an optical reader, (b) a sample preparation and delivery system, and (c) a biorecognition element (Piliarik et al., 2009), which are described in more details in the following sections.

2.2 The optical reader

This section provides the fundamentals of surface plasmons, and the optical detection, of SPR. Since design of SPR sensors varies considerably, focus is on the general principles common for SPR sensors. Surface plasmons (SPs) are electromagnetic waves that arise at metal-dielectric interfaces. In principle, several metals can generate SPs at optical frequencies, but the chemical stability of gold makes it particularly favorable. SPs propagate along the metal surface, and can be characterized by two parameters, the propagation constant and the electromagnetic field distribution. The propagation constant β_{SP} is given by

$$\beta_{\mathrm{SP}} = \frac{\omega}{c} n_{\mathrm{eff}} = \frac{\omega}{c} \sqrt{\frac{\epsilon_{\mathrm{M}} n_{\mathrm{D}}^2}{\epsilon_{\mathrm{M}} + n_{\mathrm{D}}^2}}, \tag{2.1}$$

where ω and c are the angular frequency, and the speed of light in vacuum, respectively. Thus, the propagation constant is determined by the permittivity of the metal ϵ_{M}, and the refractive index of the dielectric n_{D}. The effective refractive index of the surface plasmon is denoted n_{eff}. The electrical field of surface plasmons is transverse magnetic polarized, mainly localized to the dielectric, and decreases exponentially with a penetration depth of approximately $150 - 400\,\mathrm{nm}$, depending on the specific wavelength used.

Detection of SPR by optical readers in SPR sensors is based on coupling of a light wave to the surface plasmon. Upon changes in the effective refractive index of a surface plasmon, the characteristics of the coupled light wave changes, and the optical reader detects these changes. Coupling of light waves can be established several ways, most frequently by attenuation of total reflection (Piliarik et al., 2009). Fig. 2.1 illustrates the widely used Kretschmann geometry of the attenuated total reflection method (Homola, 2008). This method relies on a highly refractive prism, which is coated with gold at its base. A light wave is directed through the prism at an angle that ensures total reflection of the light wave at

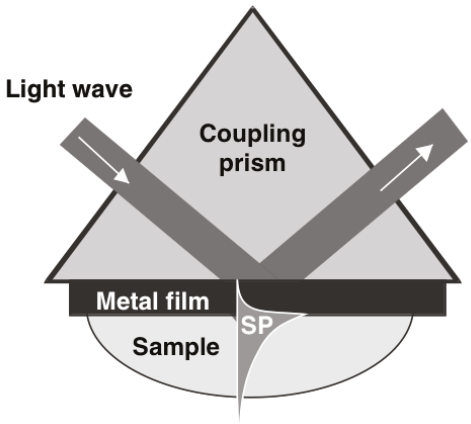

Figure 2.1: Excitation of surface plasmons in the Kretschmann geometry of the attenuated total reflection method. - Figure taken from Piliarik et al. (2009).

the prism base. The incoming light evanescently tunnels though the metal film. If the incidence light wave is closely phase-matched to the SP, an SP is excited on the outer surface of the gold. The coupling conditions that must be met can be expressed as

$$n_{\mathrm{p}} \sin\theta = n_{\mathrm{eff}}, \tag{2.2}$$

where the refractive index of the prism is denoted n_{p}, and θ is the incidence angle. When coupling of SP and a light wave occurs, energy is transferred from the light wave. Hence the characteristics of the reflected light are changed, which is visible as a SPR dip in the reflected light spectrum or intensity. SPR sensors can be classified based on the optical reader sensor output as seen in Fig. 2.2. SPR sensors with modulation of angle of incidence use a fixed monochromatic wavelength of the incidence light, and vary the angle of incidence in response to changes in the reflected light. SPR readers based on modulation of wavelength have a fixed angle of incidence and change the coupling wavelength, while readers with intensity modulation have both wavelength and angle of incidence fixed, and modulate the incidence light intensity. As evident from Eq. (2.2) a change in the effective refractive index of the SP changes the coupling conditions (Raether, 1997). In SPR sensors with wavelength or angular modulation this is recorded as a shift in the SPR dip of the angle (or wavelength)-dependent reflectance. In SPR sensors with intensity modulation a change in reflected light intensity is recorded.

Adsorption of analyte molecules to the SPR sensor surface gives rise to a

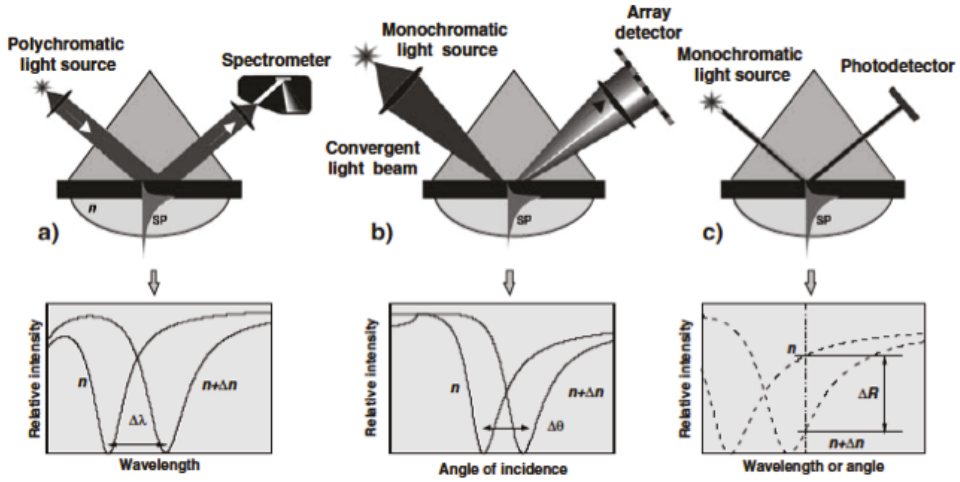

Figure 2.2: SPR sensors based on modulation of (a) wavelength, (b) angle of incidence, and (c) light intensity. - Figure taken from Piliarik et al. (2009).

change in the effective refractive index of the surface plasmon, hence the coupling conditions changes, and adsorption of analyte is detected as a change in the reflected light spectrum (wavelengths and angular modulating SPR sensors) or in the reflected light intensity (intensity modulating SPR sensors). A change in refractive index is commonly measured in resonance units (RU). The recorded signal has been demonstrated to be proportional to the surface concentration of macromolecules with 1 RU corresponding to approximately $1\,\mathrm{pgmm}^{-2}$ (Stenberg et al., 1991). In this way, SPR sensors directly measure the mass concentration of adsorbed analyte, without the need for labeling of interaction partners.

2.3 The sample preparation and delivery system

The preparation and delivery system of SPR sensors ensure that the solubilized analyte molecules are delivered to the SPR sensor chip. In general, SPR sensors function either via a cuvette system or a flow cell system (Ward and Winzor, 2000). In cuvette-based SPR sensors, a fixed volume of sample is injected into a cuvette, where the analyte interacts with the ligand on the sensor surface under no-flow conditions. Stirring while measuring is typical to reduce the effect of mass transport on the data. In flow cell based sensors, the sensor surface is

placed in a flow cell unit, which is continuously perfused with sample at flow rates ranging from $1 - 100\,\mu\text{Lmin}^{-1}$. The analyte diffuses to the sensor surface where it interacts with the ligand molecules. The latter setup is the focus point of the present thesis.

2.4 The biorecognition element

The biorecognition element of SPR readers constitutes ligand molecules, which have been immobilized on the solid surface of the SPR reader. The biorecognition element is brought in contact with analyte molecules in solution via the delivery system to allow complex formations. The choice of ligand molecule (or biorecognition element), and the method of immobilization, have important consequences for the sensitivity and detection limit of the SPR sensor (Piliarik et al., 2009). They should be carefully chosen for the purpose of ones study, taking factors such as affinity and specificity for the analyte, and stability of biological function, into consideration. Antibodies are the most frequently used biorecognition element (Robelek, 2009), but numerous biosensor chips are commercially available with various immobilized ligands, including protein, low molecular weight molecules, membrane-associated molecules, carbohydrates, virus particles, and nucleic acids.

2.5 Analysis of interactions at lipid surfaces by use of SPR spectroscopy

Molecular interactions can be detected and analyzed by an array of techniques. SPR sensors hold the advantage that labeling of the interaction partners is not necessary. This is particularly important when studying proteins, where the attachment of labels can interfere with protein function (Kodoyianni, 2011). Moreover, the technique allows one to analyze the kinetics of molecular interactions, i.e. the association and dissociation (or similarly adsorption and desorption) constants. Two major fields where SPR sensors are widely used are the detection and identification of biological analytes, and the biophysical characterization of biomolecular interactions. The SPR technique has primarily been used to study interactions between proteins (Besenicar et al., 2006), but advances in preparation and commercialization of sensor chips now also allow studies of protein-membrane, protein-nucleic acid, protein-carbohydrate, and protein-small molecule interactions (Besenicar et al., 2006). This section focuses on presenting the use of SPR sensors in studies of protein-lipid interactions, which is the focus area of the experimental part of the thesis, presented in chapter 5. The quantitative analysis of SPR data is presented in detail later in the thesis.

Many biological processes, as well as technological applications, such as food digestion and detergent activity of proteins take place at a lipid interfaces. Furthermore, important biological interactions often involve receptors embedded in membranes, and numerous important drug targets are in fact membrane proteins (Cooper, 2004). Accordingly, there has been an increasing interest for applying SPR in studies of protein interactions with lipid surfaces. Lipid surfaces on SPR sensor chips are generally made from one of three principles: 1) hybrid bilayer membranes (HBM), which can be made by applying lipid vesicles to a hydrophobic coating of the sensor chip gold surface (Plant, 1993; Plant et al., 1995; Terrettaz et al., 1993; Cooper et al., 1998). 2) Immobilization of lipid bilayers (Lang et al., 1994; Bunjes et al., 1997). 3) Immobilization of liposomes (Cooper et al., 2000; Granéli et al., 2004). The first commercially available sensor chip, designed for studying interactions with lipids, was the HPA chip launched by Biacore. The HPA chip design is based on depositing a monolayer of self-assembled alkanethiols onto the gold surface of a sensor chip. The self-assembled monolayer (SAM) enable HBM formation when the user applies lipid vesicles. The lipid vesicles spontaneously adsorb to the SAM by hydrophobic interactions between the SAM and the hydrophobic acyl chain. The polar head groups of the vesicle lipids thereby comprise the membrane/solution interface. The HBM surface has some desirable qualities, as it is very stable and homogenous with few defects in the lipid monolayer, and resists nonspecific binding of proteins like BSA (Plant et al., 1995; Terrettaz et al., 1993; Cooper et al., 1998). Cooper et al. (1998) thoroughly investigated the formation of lipid monolayers on the HPA chip, using different lipid vesicles preparation methods. They also demonstrated that the correlation between deposited lipid, and the observed response (number of response units, RU), was similar to that of proteins. A monolayer of lipids corresponds to a deposited mass of $2.0\,\mathrm{ngmm}^{-2}$, giving rise to a response of about 2200 RU. The HPA sensor chip constitute a very simple and robust membrane model (Cooper, 2004), but has some limitations in its membrane mimetic properties, as it only consists of a supported monolayer. Membrane mimetic properties are particularly desired in biological research, where understandings of protein interactions with (or in) cellular membranes or micelles are sought. A significant advantage of sensor chips with immobilized membrane bilayer or liposomes is that they allow reconstitution of functional transmembrane proteins within the lipid surface (Heyse et al., 1998; Lang et al., 1994; Stora et al., 1999). This is particularly important for studying interactions with membrane proteins, as they often require the lipid environment to retain their functional and structural integrity Cooper (2004). Various techniques for immobilization of membrane bilayers and liposomes have been developed and are reviewed by Besenicar et al. (2006); Cooper (2002). At present, the most frequently used sensor chip in protein-membrane studies is the

L1 chip from Biacore, which is designed to immobilize liposomes or membrane preparations from cell lysates (Besenicar and Anderluh, 2010). Studies of direct interaction between a protein and a lipid surface often seek information about either lipid specificity or about membrane binding motifs of the protein (Besenicar et al., 2006). Lipid specificity can be addressed by modulation of the lipid composition of the biorecognition element, and has been studied for instance for toxins (Bakrac et al., 2008; Kuziemko et al., 1996) and amyloid protein (Aguilar and Small, 2005). Identification of amino acids involved in the binding process of a protein to lipid surfaces has been identified for a number of proteins, using mutagenesis to generate genetically modified protein variants, which are then characterized using SPR sensors (Bakrac et al., 2008; Jones et al., 2005; Stahelin and Cho, 2001). Thus, Stahelin and Cho (2001) investigated the importance on ionic, aromatic, and aliphatic amino acids for the binding of phospholipase A2 to immobilized liposomes. They proposed a general model for protein attachment to membranes, where electrical interactions between aromatic amino acids and a zwitterionic membrane initially bring the protein to the membrane surface. Subsequent hydrophobic interactions between aromatic and aliphatic residues, and the hydrophobic lipids of the membrane, are responsible for a firm protein attachment. Other applications of SPR sensors within the field of protein-membrane interactions include analysis of initial binding of pore-forming proteins to membranes (Anderluh et al., 2003), binding of coagulation factor VIII to the phospholipid surfaces (Saenko et al., 2001), membrane binding of amyloid protein and amylogenic peptides (Aguilar and Small, 2005; Mozsolits and Aguilar, 2002; Mozsolits et al., 2003). Finally, numerous interactions with reconstituted transmembrane proteins have been studies with SPR sensors (Heyse et al., 1998; Stora et al., 1999; Cooper, 2004; Salamon et al., 1999; Besenicar et al., 2006; Cho et al., 2001).

2.6 SPR in the present thesis

In the experimental part of the present Ph.D. project surface plasmon resonance SPR spectroscopy (Biacore) is applied to study adsorption dynamics of lipase, and competitive adsorption dynamics of lipase and surfactants, on model hydrophobic surfaces established on the Biacore HPA chip (see chapter 5 for a more detailed description). While the Biacore SPR apparatus is capable of capturing qualitative adsorption behavior, quantitative studies of chemical rate constants and equilibrium constants are more challenging. Inconsistencies in derived rate constants have lead to both experimental and theoretical investigations of the effect of convection and diffusion of the binders in the microfluidic flow cell, i.e. mass transport, on the SPR signal (Schuck and Minton, 1996; Myszka et al.,

1998 Aug). Significant progress was made by the application of a theoretical quasi-steady-state approximation. This approximation has been richly adopted for Biacore data analysis due to its simplicity (Schuck, 1996; Schuck and Minton, 1996; Mason et al., 1999; Noinville et al., 2010; Myszka et al., 1998 Aug; Goldstein et al., 1999 Sep-Oct). However, practice in the biochemical society still, to a large degree, consists of empirical and qualitative studies (Rich and Myszka, 2010, 2008, 2007). The next chapter provides an in-depth description of the theoretical modeling used for SPR data analysis.

Chapter 3

Mathematical modeling of transport phenomena in surface-based biosensors

This chapter presents a theoretical and computational investigation of convection, diffusion, and adsorption in surface-based biosensors. We study the transport dynamics in a model geometry designed to mimic the actual geometry used in the Biacore SPR apparatus. As a novel feature the finite distance from the inlet of the microfluidic flow cell to the sensor surface is included. The evolution equations are introduced, and subsequently made nondimensional, leading to a number of nondimensional parameters, which will be subject to an in-depth parameter study during the chapter. An approximate quasi-steady theory, which is widely adopted in the surface-based biosensor community, is reviewed. Additionally, an analytical solution, which to our knowledge has not been published before, is presented. A nondimensional formulation of the quasi-steady theory reveals the important nondimensional parameter, known as the Damköhler number, which is sometimes referred to as the limit coefficient. An expression of the Damköhler number is derived in terms of the Biot number, the Peclet number, and the model geometry. The ability of the quasi-steady theory to capture convective and diffusive mass transport in the surface-based biosensor is thoroughly tested, by comparison with numerical simulations of the transient dynamics. In this way the consequences of using the quasi-steady theory for experimental data fitting in both kinetically limited and convection-diffusion limited regimes are properly quantified. The results clarify the conditions under which the quasi-steady theory lack credibility. In extension to the well known fact that credibility is altered under convection-diffusion limited conditions, we also show how the ratio of the inlet concentration to the maximum surface capacity is critical for reliable use of the quasi-steady theory.

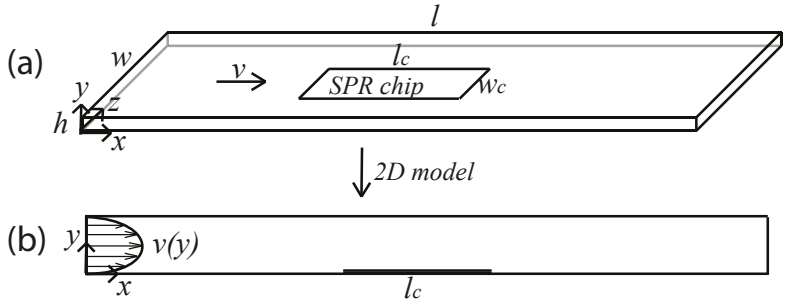

Figure 3.1: Microfluidic flow cell - (a) Rectangular flow cell of length l, height h, and width w. The SPR chip of length l_c, and width w_c, is indicated as the square in the middle of the flow cell. The buffer flow is represented by the velocity vector v. (b) The two-dimensional approximation of the system in the vertical xy-plane. The parabolic velocity profile is indicated at the inlet of the flow cell.

3.1 System geometry and two-dimensional approximation

We investigate the transport dynamics in a geometry designed to replicate the actual geometry used by Biacore (Fig. 3.1). The length scales for this particular geometry are $l = 2.3\,\mathrm{mm}$, $w = 0.5\,\mathrm{mm}$, and $h = 0.05\,\mathrm{mm}$. Adsorption is probed by the SPR chip, located on the surface in the middle of the flow cell. The SPR chip has a length of $l_\mathrm{c} = 0.6\,\mathrm{mm}$, and a width of $w_\mathrm{c} = 0.16\,\mathrm{mm}$. The fluid flows in the lengthwise direction (x), with a parabolic velocity profile along the direction (y) of the height of the flow cell, i.e. $v_x(y) = 4v_m(y/h)(1 - y/h)$, where v_m is the maximum velocity (Batchelor, 1967). Based on the large geometric aspect ratio $w/h = 10$, and the small Reynolds numbers often present in the system, we have assumed total invariance in the direction (z) of the width of the flow cell (Brody et al., 1996), essentially ending up with a two-dimensional consideration of the transport. Hereby we do not take boundary effects from the side walls of the flow cell at $z = \{0, w\}$ into account.

3.2 Evolution equations

The main objective of the mathematical model is to describe the spatio-temporal evolution of some molecular solute components, dissolved in a homogeneous medium, such as water. In this perspective all molecular details of the solvent are ignored altogether. The solvent simply acts as a medium, facilitating convective

and diffusive transport of the solute components. A continuum consideration of some solute component i leads to the definition of two dependent field variables, namely the bulk concentration field $c_i = c_i(x, y, t)$, and the corresponding surface concentration field $\gamma_i = \gamma_i(x, t)$, where t is time. We name the bulk domain Ω, and the surface domains $\{\partial\Omega, \partial\Omega_{\text{ads}}\}$, referring to respectively insulating non-adsorbing surfaces, and surfaces where adsorption takes place. The spatio-temporal evolution of the bulk concentration field $c_i(x, y, t)$ is governed by the convection-diffusion equation

$$\frac{\partial c_i}{\partial t} + v_x(y)\frac{\partial c_i}{\partial x} = D_i \nabla^2 c_i, \qquad \Omega \tag{3.1}$$

where the Laplacian $\nabla^2 = \partial^2/\partial x^2 + \partial^2/\partial y^2$, and D_i is the diffusion coefficient for molecular component i. The boundary conditions for the bulk concentration are given by

$$\frac{\partial c_i}{\partial y} = 0, \qquad \partial\Omega \tag{3.2a}$$

$$-D_i\frac{\partial c_i}{\partial y} = -\mathcal{A}_i(\gamma_i, c_i, \ldots), \qquad \partial\Omega_{\text{ads}} \tag{3.2b}$$

The former is simply a no-flux condition, whereas the latter is a balance between diffusive flux perpendicular to the surface and net adsorption rate, captured in the adsorption term $\mathcal{A}_i(\gamma_i, c_i, \ldots)$ in Eq. (3.5). At the inlet of the flow cell, at $x = 0$, the concentration is equal to the injection concentration, $c_i = c_{i,0}$. At the outlet of the flow cell, $x = l$, we assume free convection, i.e. essentially $\partial c_i/\partial x = 0$. The spatio-temporal evolution of the surface concentration field $\gamma_i = \gamma_i(x, t)$ is governed by the adsorption-diffusion equation

$$\frac{\partial \gamma_i}{\partial t} - \frac{\partial}{\partial x}\left[D_{i,s}\frac{\partial \gamma_i}{\partial x}\right] = \mathcal{A}_i(\gamma_i, c_i, \ldots), \qquad \partial\Omega_{\text{ads}} \tag{3.3}$$

where $D_{i,s}$ is the surface diffusion coefficient of molecular component i, which in general can be a function of both the independent variables, x and t, as well as the dependent variables $\gamma_i, c_i, \ldots$. The adsorption term $\mathcal{A}(\gamma_i, c_i, \ldots)$ represents the net rate of change of surface concentration due to adsorption and desorption. A particular functionality of $\mathcal{A}(\gamma_i, c_i, \ldots)$ is determined by the kinetics of some chosen adsorption-desorption scheme, and can in general include arbitrarily complex surface kinetics. Particular functionalities of $\mathcal{A}(\gamma_i, c_i, \ldots)$ are provided for unimolecular and bimolecular systems respectively in section 3.3.1 and section 3.4.1. Finally, no-flux boundary conditions for γ_i, i.e. $\partial\gamma_i/\partial x = 0$ are imposed at the end of the adsorbing domain, i.e. surface bound molecules only leave the chip by desorption.

Importantly, the total surface concentration Γ, which is the natural measure of a surface-based biosensor, is given by the sum

$$\Gamma = \sum_i \gamma_i. \tag{3.4}$$

3.3 Unimolecular systems

In this section the general evolution equations introduced in chapter 3.2 are analyzed in considerable detail for a single molecular solute component. This case is referred to as a unimolecular system. First, the adsorption kinetics is presented. Then, nondimensional formulations of the unimolecular evolution equations are presented. This is followed by an order of magnitude estimation of the nondimensional parameters. The section ends with a presentation of the weak formulation of the unimolecular evolution equations, which is used for implementation of the finite element method in the ComSol/MatLab computational software.

3.3.1 Surface adsorption kinetics

The adsorption kinetics has to be modeled by a phenomenological model, which ultimately captures experimental data and thereby provides reasonable and consistent phenomenological parameters. The standard adsorption model that contains the feature of a maximum surface capacity γ_m is the Langmuir adsorption model. This model is essentially a first order scheme between bulk molecules at the interface $c|_{y=0}$ and free surface space $(\gamma_\mathrm{m} - \gamma)$, with adsorption rate constant k_a and desorption rate constant k_d. For a single molecular component this first order model may be written in the form

$$\mathcal{A}(\gamma, c) = k_\mathrm{a} c|_{y=0}(\gamma_\mathrm{m} - \gamma) - k_\mathrm{d}\gamma. \tag{3.5}$$

When $c|_{y=0}$ is independent of γ this is a linear relation between $\mathcal{A}(\gamma, c)$ and γ. This particular adsorption model is a *local theory* in both space and time, i.e. the evolution of γ at (x, t) depends only on the present state at (x, t). The ultimate goal is often to obtain consistent values for the triplet $(k_\mathrm{a}, k_\mathrm{d}, \gamma_\mathrm{m})$ of phenomenological parameters from experimental biosensor data. In this linear model the adsorption and desorption rate constants, k_a and k_d respectively, are assumed unaltered by the density on the surface. In reality on might expect interactions between adsorbed particles at high densities. In spite of its simplicity, however, it has been argued that this model is general enough to explain the majority of adsorption/desorption processes in molecular biology (Gervais and Jensen, 2006). Substituting Eq. (3.5) into Eq. (3.3) and Eq. (3.2b), these two equations together with Eq. (3.1), and the remaining boundary conditions, form a nonlinear system

of partial differential equations for the concentration fields $c_i(x, y, t)$ and $\gamma_i(x, t)$. The system is in general of such complexity that a numerical study is necessary for detailed analysis.

3.3.2 Nondimensional parameterization

Nondimensional formulations are developed for a more comprehensible parameterization of the unimolecular evolution equations. Two different nondimensional formulations are introduced and discussed.

Nondimensional parameterization: kinetic scaling

In order to put the evolution equations on nondimensional form, we introduce the following spatial and temporal scales:

$$\overline{x} = \frac{x}{h}, \quad \overline{y} = \frac{y}{h}, \quad \overline{t} = k_{\mathrm{a}} c_0 t. \tag{3.6}$$

Note in particular, that time has been made nondimensional by the adsorption rate. For the dependent concentration variables we introduce the following scaled dependent variables:

$$\overline{c} = \frac{c}{c_0}, \quad \overline{\gamma} = \frac{\gamma}{\gamma_{\mathrm{m}}}. \tag{3.7}$$

In terms of these nondimensional variables, and the definitions $f(\overline{y}) = 4\overline{y}(1-\overline{y})$, $\overline{\nabla}^2 = \partial^2/\partial\overline{x}^2 + \partial^2/\partial\overline{y}^2$ we obtain the nondimensional evolution equation for the bulk concentration field

$$\mathrm{Bi}\overline{c}_0 \frac{\partial \overline{c}}{\partial \overline{t}} + \mathrm{Pe} f(\overline{y}) \left(\frac{\partial \overline{c}}{\partial \overline{x}} \right) = \overline{\nabla}^2 \overline{c}, \qquad \Omega \tag{3.8}$$

with the boundary condition in Eq. (3.2b) given by

$$\left. \frac{\partial \overline{c}}{\partial \overline{y}} \right|_{\overline{y}=0} = \mathrm{Bi}\overline{c}|_{\overline{y}=0}(1-\overline{\gamma}) - K\mathrm{Bi}\gamma, \qquad \partial\Omega_{\mathrm{ads}} \tag{3.9}$$

The nondimensional evolution equation for the surface concentration field is given by

$$\frac{\partial \overline{\gamma}}{\partial \overline{t}} - \frac{\partial}{\partial \overline{x}} \left[\frac{d_s}{\mathrm{Bi}\overline{c}_0} \frac{\partial \overline{\gamma}}{\partial \overline{x}} \right] = \overline{c}|_{\overline{y}=0}(1-\overline{\gamma}) - K\gamma, \qquad \partial\Omega_{\mathrm{ads}} \tag{3.10}$$

The remaining boundary conditions are easily translated into the nondimensional form. These nondimensional evolution equations are parameterized by the fol-

lowing five nondimensional groups.

$$\mathrm{Pe} = v_m h/D, \tag{3.11a}$$
$$\mathrm{Bi} = k_\mathrm{a}\gamma_\mathrm{m} h/D, \tag{3.11b}$$
$$\overline{c}_0 = c_0 h/\gamma_\mathrm{m}, \tag{3.11c}$$
$$K = k_\mathrm{d}/k_\mathrm{a}c_0, \tag{3.11d}$$
$$d_s = D_s/D. \tag{3.11e}$$

The Peclet number Pe measures the ratio of transport by convection to perpendicular diffusion, and is essentially the nondimensional flow rate. The Biot number Bi measures the ratio of adsorption rate to diffusion along the height of the flow cell, and is essentially the nondimensional adsorption rate constant. $\overline{c}_0$ is a nondimensional inlet concentration. In the limit of no flow, $\overline{c}_0$ is the reciprocal of the fraction of the height h needed to fill the surface up to $\gamma = \gamma_\mathrm{m}$. This interpretation explains the close relationship between $\overline{c}_0$ and the so called depletion depth introduced by Alvarez et al. (2010). K is the kinetic equilibrium constant. d_s is the ratio of the surface and bulk diffusion coefficients, and if $D_s < D$, $d_s \in \{0, 1\}$ measures the hindrance of diffusion caused by the presence of the surface. Interestingly, the magnitude of the transient term in Eq. (3.8) is weighed by the product $\overline{c}_0\mathrm{Bi} = k_\mathrm{a}c_0h^2/D$, essentially meaning that adsorption dynamics for large inlet concentrations of molecules with a high affinity to the surface evolves in a transient regime. This result is supported by Squires et al. (2008).

Dimensionless parameterization: diffusion scaling

Following a similar approach as above, but with the difference of scaling time with a diffusion time, i.e. $\overline{t} = Dt/h^2$, the dimensionless evolution equation for the bulk concentration field takes the form

$$\frac{\partial \overline{c}}{\partial \overline{t}} + \mathrm{Pe} f(\overline{y})\left(\frac{\partial \overline{c}}{\partial \overline{x}}\right) = \overline{\nabla}^2 \overline{c}, \qquad \Omega \tag{3.12}$$

while the boundary condition in Eq. (3.2b) is now given by

$$\left.\frac{\partial \overline{c}}{\partial \overline{y}}\right|_{\overline{y}=0} = \mathrm{Bi}\overline{c}|_{\overline{y}=0}(1-\overline{\gamma}) - K\mathrm{Bi}\overline{\gamma}, \qquad \partial\Omega_\mathrm{ads} \tag{3.13}$$

The dimensionless evolution equation for the surface concentration field becomes

$$\frac{\partial \overline{\gamma}}{\partial \overline{t}} - \frac{\partial}{\partial \overline{x}}\left[d_s \frac{\partial \overline{\gamma}}{\partial \overline{x}}\right] = \mathrm{Bi}\overline{c}_0\overline{c}|_{\overline{y}=0}(1-\overline{\gamma}) - K\mathrm{Bi}\overline{c}_0\overline{\gamma}, \qquad \partial\Omega_\mathrm{ads} \tag{3.14}$$

The correspondence between the time scales for kinetic scaling (ks) and diffusion scaling (ds) is

$$\overline{t}^\mathrm{ks} = \overline{t}^\mathrm{ds} k_\mathrm{a}c_0h^2/D = \mathrm{Bi}\overline{c}_0\overline{t}^\mathrm{ds}. \tag{3.15}$$

Kinetic scaling or diffusion scaling?

The kinetic scaling of time leads to a dimensionless formulation which is particularly advantageous in the regime of kinetically limited dynamics. Generally speaking, kinetically limited dynamics is obtained for small Bi numbers ($\mathrm{Bi} \ll 1$) and/or large Peclet numbers ($\mathrm{Pe} \gg 1$). Kinetically limited dynamics is, opposed to convection-diffusion limited dynamics, characterized by an independence of the flow rate, i.e. the Peclet number, and a scaling of the dynamics with the Biot number. This dynamical behavior is referred to as a kinetic scaling, which is therefore also the terminology used for this particular dimensionless formulation. If, on the other hand, the adsorbing molecules have a very high affinity to the surface, such as in the case of hydrophobic proteins in aqueous solution, $\mathrm{Bi} \gg 1$. In this limit the dynamics is convection-diffusion limited, which is characterized by an independence of adsorption rate, i.e. Biot number, and a scaling of the dynamics with the Peclet number. In this limit it is advantageous to use the diffusion scaling of time.

Disregarding the dynamical limit of the system, there are other pros and cons for applying the two different time scales. As seen below, an approximation of quasi-steady-state in the bulk transport dynamics leads to a theory, which adopts a minimal number of dimensionless parameters using kinetic scaling. Hence kinetic scaling is advantageous when working with the quasi-steady theory. This is consistent with the fact that the quasi-steady-state approximation is only theoretically supported for kinetically limited dynamics. This is further elaborated on in section 3.5. However, concerning practical use of the theory for experimental data fitting, we remark that k_a is usually a parameter one wishes to determine from an adsorption experiment, and is thereby unknown *a priori*. Hence, kinetic scaling is not practical for experimental data fitting - an issue avoided by using diffusion scaling. Dependent on the experimental regime it might as well be preferable to present and fit experimental data unscaled.

3.3.3 Estimates of nondimensional parameters

In this section we estimate some reasonable values for the dimensionless numbers. Concerning typical operating conditions, flow rates are in the range $Q = 1 - 100\,\mu\mathrm{L min}^{-1}$, which amounts to maximum velocities of $v_m = 3Q/2hw = 10^{-3} - 10^{-1}\,\mathrm{ms}^{-1}$. Injection concentrations typically range from $c_0 = 10^{-1} - 10^{2}\,\mu\mathrm{M}$. To proceed we need to consider a model binder. We take as an example a globular protein with a diameter of $2R = 5\,\mathrm{nm}$, and molecular weight $M_w = 30\,\mathrm{kDa} = 3 \times 10^4\,\mathrm{gmol}^{-1}$. A simple estimate of the maximum surface capacity γ_m is simply the weight of one molecule divided by its diameter squared.

Viz, $\gamma_{\mathrm{m}} = M_w/4N_{\mathrm{A}}R^2 \approx 2 \times 10^3\,\mu\mathrm{gm}^{-2}$, where N_{A} is the Avogadro number. However, in biochemical studies the surface of the chip, or the dextran layer, is sometimes prepared with a relatively low number of binding sites, with the aim of reducing rebinding probability and neighbor interactions among the adsorbing binders. This implies that the above estimate for γ_{m}, which is based on a packing occurring for e.g. self-assembled monolayers, represents an upper limit. In several applications the maximum surface capacity can be significantly lower. The diffusion coefficient can be estimated from the Stokes-Einstein relation. In aqueous solution at room temperature the dynamic viscosity is $\mu \approx 10^{-3}\,\mathrm{Nsm}^{-2}$, and $T \approx 300\,\mathrm{K}$, hence $D = k_{\mathrm{B}}T/6\pi\mu R \approx 10^{-10}\,\mathrm{m}^2\mathrm{s}^{-1}$.

Based on the above values we can estimate the regime of the dimensionless numbers. By choosing $c_0 \approx 1\,\mu\mathrm{M}$, we obtain $\bar{c}_0 = c_o h/\gamma_{\mathrm{m}} \approx 1$, in the case of close packing on the surface. For surfaces prepared with a lower number of binding sites $\bar{c}_0 > 1$. For the Peclet number we obtain $\mathrm{Pe} = v_m h/D \approx 5 \times 10^2 - 5 \times 10^4$.

3.3.4 The weak formulation

The weak formulation of the unimolecular evolution equations is derived using the diffusion scaling. The kinetic scaling can later be obtained by a straightforward rescaling of time $\bar{t}^{\mathrm{ks}} = \mathrm{Bi}\bar{c}_0\bar{t}^{\mathrm{ds}}$. The overline notation for the dimensionless variables is skipped for clarity. The first step of obtaining the weak form is by multiplication with a test function and integrating over the domain on which the function is defined. For the bulk field we get

$$\int_\Omega \hat{c}\frac{\partial c}{\partial t}\,\mathrm{d}A + \int_\Omega \mathrm{Pe} f(y)\hat{c}\left(\frac{\partial c}{\partial x}\right)\mathrm{d}A = \int_\Omega \hat{c}\nabla \times \nabla c\,\mathrm{d}A$$

The second step is to reduce the order of the differential equation by integration by parts of the highest order derivative and using Gauss' theorem. In this way the second order derivative is removed, such that the function c can be approximated by linear shape functions, whose first order derivatives have jump discontinuities. The partial integration yields

$$\int_\Omega \hat{c}\nabla \times \nabla c\,\mathrm{d}A = \int_{\partial\Omega} \hat{c}\nabla c \times n\,\mathrm{d}s - \int_\Omega \nabla\hat{c} \times \nabla c\,\mathrm{d}A$$

Finally, the terms involving temporal respectively spatial derivatives are collected on the left respectively right hand side of the equation, viz

$$\int_\Omega \hat{c}\frac{\partial c}{\partial t}\,\mathrm{d}A = \int_{\partial\Omega} \hat{c}\nabla c \times n\,\mathrm{d}s - \int_\Omega \left[\nabla\hat{c} \times \nabla c + \mathrm{Pe} f(y)\hat{c}\left(\frac{\partial c}{\partial x}\right)\right]\mathrm{d}A \qquad (3.16)$$

The boundary integral, i.e. the first term on the right hand side, essentially contains the boundary conditions for the bulk field. So far nothing has been said about the test functions $\hat{c}$. The test functions $\hat{c}$ is chosen to vanish at boundaries where the function c satifies *Dirichlet* conditions, but not elsewhere. Hence

$$\hat{c} = 0, \quad \text{at} \quad x = 0.$$

Also, for the insulating surfaces, as well as for the outlet with convective flux, the homogeneous Neumann boundary conditions $\nabla c \times n = 0$ translate into a vanishing contribution to the boundary integral. Clearly, the integrand in the boundary integral is non-zero only at adsorbing surfaces where

$$\left.\frac{\partial c}{\partial y}\right|_{y=0} = \mathrm{Bi}c|_{y=0}(1-\gamma) - K\mathrm{Bi}\gamma \qquad \partial\Omega_{\mathrm{ads}} \tag{3.17}$$

For the sake of completeness the weak formulation of the bulk field is summarized in

$$\int_\Omega \hat{c}\frac{\partial c}{\partial t}\,\mathrm{d}A = \int_{\partial\Omega_{\mathrm{ads}}} \Big[\mathrm{Bi}c|_{y=0}(1-\gamma) - K\mathrm{Bi}\gamma\Big]\,\mathrm{d}x - \int_\Omega \left[\nabla\hat{c}\times\nabla c + \mathrm{Pe}f(y)\hat{c}\left(\frac{\partial c}{\partial x}\right)\right]\mathrm{d}A \tag{3.18}$$

The weak formulation for the surface field is obtained in a similar way, however since the equation is naturally first order, it is simply

$$\int_{\partial\Omega_{ads}} \hat{\gamma}\frac{\partial \gamma}{\partial t}\,\mathrm{d}x = \int_{\partial\Omega_{ads}} \hat{\gamma}\left[\frac{\partial}{\partial x}d_s\frac{\partial\gamma}{\partial x} + \mathrm{Bi}c_0 c|_{y=0}(1-\gamma) - K\mathrm{Bi}c_0\gamma\right]\mathrm{d}x \tag{3.19}$$

Eqs. (3.18) and (3.19) constitute the weak formulation of the unimolecular evolution equations. The mathematical goal is to find a set of functions (c, γ) that satisfies Eqs. (3.18) and (3.19), as well as $c = 1$ at $x = 0$, for all sufficiently smooth functions $(\hat{c}, \hat{\gamma})$, where $\hat{c}$ has the property that it vanishes at $x = 0$. This task is performed by an implementation of the weak formulation of the evolution equations in the ComSol/MatLab computational software. More details on the finite element method is outside the scope of the present thesis. Numerical analysis based on an implementation of the weak form is presented in chapter 4.

3.4 Bimolecular systems

In this section the general evolution equations, introduced in chapter 3.2, are developed for a bimolecular system, i.e. two molecular solute components. The solute components in the bulk phase are assumed to be dissolved to a dilute state, such that intermolecular interactions of the solutes can be ignored. On the

surface the solute particles are close together, i.e. molecular length scales, for an extended period of time, hence interactions on the surface have to be taken into account. In this way, the introduction of an additional component only alters the adsorption kinetics. Following a presentation and discussion of the adsorption kinetics, nondimensional formulations of the bimolecular evolution equations are presented along with an order of magnitude estimation of the nondimensional parameters.

3.4.1 Surface adsorption kinetics

The main scope of the bimolecular system is to model competitive adsorption of two species. The model is motivated by experiments on the competitive adsorption of lipase enzymes and surfactants, which is explained in detail in chapter 5, and in particular section 5.4. Like for the unimolecular system the adsorption kinetics is modeled by a phenomenological model, designed as an attempt to consistently capture experimental data and provide reasonable and consistent phenomenological parameters. For the sake of clarity the kinetic rate equations for the two-component competitive adsorption/desorption dynamics are developed, with no convective-diffusive transport in mind, and then subsequently integrated into the full theoretical spatio-temporal framework.

When two different species are present on the surface together, it has to be taken into account that they will give different response in the SPR measurement per unit area. This is actually the only way to distinguish between different adsorbed species on the surface, as SPR spectroscopy is a label-free method as described in chapter 2. A simple approach to cope with this challenge is simply to develop the kinetic rate equations in terms of the relative surface areas exerted by the different species. Defining the surface area fractions for enzyme and surfactant as respectively θ_e and θ_s, the kinetic rate equations can be written generally as

$$\frac{d\theta_e}{dt} = f_e(\theta_e, \theta_s, c_e, c_s; k_{e,i}) \tag{3.20a}$$

$$\frac{d\theta_s}{dt} = f_s(\theta_e, \theta_s, c_e, c_s; k_{s,i}) \tag{3.20b}$$

where the functions f_e and f_s are the rate of change of the area-based surface concentrations due to adsorption and desorption kinetics. These terms, in general, depend on the concentration field variables and are constrained by some parameters $k_{e,i}$, $k_{s,i}$ that include adsorption and desorption rate constants, maximum surface capacities, and other possible constraints.

Integrating the kinetics with bulk transport

The source term $\mathcal{A}_i$ in Eq. (3.3) is simply the rate of change of mass-based surface concentration due to adsorption and desorption kinetics, hence in order to integrate the two-component kinetic rate equations into the full spatio-temporal framework we simply put

$$\mathcal{A}_i = \gamma_{\mathrm{m},i} d\theta_i/dt, \tag{3.21}$$

where $\gamma_{\mathrm{m},i}$ is maximum surface capacity of the particular specie i. Under purely kinetically limited conditions, with no account of convective-diffusive transport, the surface concentrations are only functions of time, and Eqs. (3.20) are simply two coupled ordinary differential equations (ODE's) for the temporal evolution of the surface concentrations. The general framework is written as

$$\mathcal{A}_e = \gamma_{\mathrm{m},e} f_e(\theta_e, \theta_s, c_e, c_s; k_{e,i}) \tag{3.22a}$$
$$\mathcal{A}_s = \gamma_{\mathrm{m},s} f_s(\theta_e, \theta_s, c_e, c_s; k_{s,i}) \tag{3.22b}$$

Kernel of the two-component model

Motivated by experimental results the surfactant system is modeled by the simple Langmuir adsorption/desorption model presented in section 3.3.1. Also, the lipase enzymes are known to adsorb irreversibly in the absence of surfactants. Taking into account that free surface space is given by $(1 - \theta_s - \theta_e)$ the dynamics is modeled by the following system of adsorption rate equations

$$\frac{d\theta_e}{dt} = k_{\mathrm{a},e} c_e (1 - \theta_s - \theta_e) \tag{3.23a}$$
$$\frac{d\theta_s}{dt} = k_{\mathrm{a},s} c_s (1 - \theta_s - \theta_e) - k_{\mathrm{d},s} \theta_s \tag{3.23b}$$

In terms of the mass-based concentration fields we obtain

$$\mathcal{A}_e = k_{\mathrm{a},e} c_e (\gamma_{\mathrm{m},e} - \gamma_e - \frac{\gamma_{\mathrm{m},e}}{\gamma_{\mathrm{m},s}} \gamma_s) \tag{3.24a}$$
$$\mathcal{A}_s = k_{\mathrm{a},s} c_s (\gamma_{\mathrm{m},s} - \gamma_s - \frac{\gamma_{\mathrm{m},s}}{\gamma_{\mathrm{m},e}} \gamma_e) - k_{\mathrm{d},s} \gamma_s \tag{3.24b}$$

An important aspect, which however deserves attention at this point, is that the surfactant forms micelles in solution above the critical micelle concentration (cmc). The micelles, being multimolecular aggregates, diffuse slower, and can be expected to exhibit a different intrinsic adsorption behavior than that of the single surfactant molecules. From this perspective the definition of the bulk surfactant concentration, and a corresponding adsorption rate constant $k_{\mathrm{a},s}$, seems dubious. A more thorough theoretical model would take into account the dynamics of

micelle formation, and the adsorption/desorption dynamics of single surfactant molecules and micelles, separately. To keep the complexity level reasonable this approach is however avoided in the present work. This decision is actually data-driven. For the experiments done in the present work the pure surfactant system is reasonably well captured by the Langmuir model as shown in section 5.4. A two-component model like Eqs. (3.24), without any displacement of one specie by the other, has been analyzed by Fu and Santore (1998).

First order displacement model

In the presence of surfactants, enzyme desorption is observed. Different mechanisms, some of which are discussed in chapter 5, have been proposed in order to explain how surfactants displace enzyme on the surface in a competitive process. In regards to modeling surface kinetics a mathematical term is needed to capture this competitive displacement process. The most plain way of modeling the competitive displacement process is by a first order reaction between surface bound surfactant and enzyme, in which case a negative term $-k_c\theta_s\theta_e$ is added to Eq. (3.26a), such that

$$\frac{d\theta_e}{dt} = k_{a,e}c_e(1-\theta_s-\theta_e) - k_c\theta_s\theta_e \tag{3.25a}$$

$$\frac{d\theta_e}{dt} = k_{a,s}c_s(1-\theta_s-\theta_e) - k_{d,s}\theta_s \tag{3.25b}$$

In terms of the mass-based concentration fields we obtain

$$\mathcal{A}_e = k_{a,e}c_e(\gamma_{m,e}-\gamma_e-\frac{\gamma_{m,e}}{\gamma_{m,s}}\gamma_s) - k_c\frac{\gamma_s}{\gamma_{m,s}}\gamma_e \tag{3.26a}$$

$$\mathcal{A}_s = k_{a,s}c_s(\gamma_{m,s}-\gamma_s-\frac{\gamma_{m,s}}{\gamma_{m,e}}\gamma_e) - k_{d,s}\gamma_s \tag{3.26b}$$

This model, albeit simple, captures the essence of the competitive adsorption of two species, including displacement of one specie by the other.

Coorporative displacement model

The above form of the displacement term, being of first order in both surfactant and enzyme, takes no coorporative behavior of the surfactant into account. In reality it is well known (see section 5.4) that the surfactant has properties of self-assembly and enhanced surface activity above a certain concentration threshold. It is therefore probable that the displacement is better captured by some higher order model. One displacement model that has many of the wanted properties

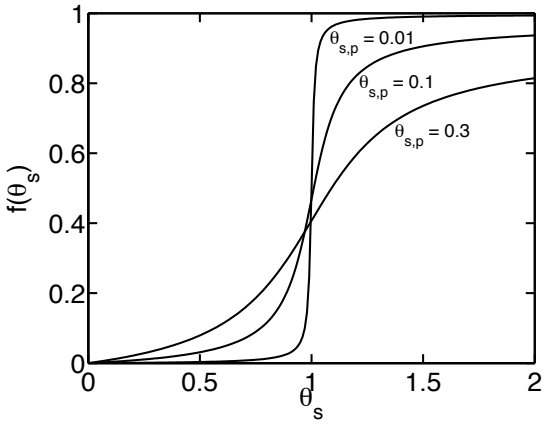

Figure 3.2: Coorporative displacement model - Parameters: $\theta_{s,c} = 1$, $\theta_{s,p} = \{0.01, 0.1, 0.3\}$

is build from the inverse tangent function. Choosing again a first order form for the enzyme leads to a competitive term $-k_c f(\theta_s)\theta_e$, where

$$f(\theta_s) = \frac{1}{\pi}\left[\arctan\left(\frac{\theta_s - \theta_{s,c}}{\theta_{s,p}}\right) + \arctan\left(\frac{\theta_{s,c}}{\theta_{s,p}}\right)\right] \tag{3.27}$$

This form, in principle, introduces two additional parameters: $\theta_{s,c}$, measuring the surface concentration of surfactant at which the coorporativity enhances its competitive properties, as well as $\theta_{s,p}$ that measures how dramatic the change in competitive properties is. Increasing the value of $\theta_{s,p}$ leads to a less dramatic change and vice versa. The functionality of the model is presented in Fig. 3.2. The model is chosen such that it goes to zero for vanishing surfactant concentrations, and to unity for large surfactant concentrations. The latter property implies that k_c is a normalized measure of the strength of the displacement.

3.4.2 Nondimensional parameterization

The nondimensional parameterization is done for the first order competitive adsorption model, and to keep the number of free parameters to a reasonable minimum surface diffusion is neglected. The mathematical formulation of the spatiotemporal problem for the bimolecular system consists of two independent versions of Eq. (3.1) for the two molecular components, respectively. The coupling of the two fields arises from the two versions of the surface evolution equations (Eq. (3.3)), and the boundary flux balance conditions (Eq. (3.2b)). The following

spatial and temporal scales are applied:

$$\overline{x} = \frac{x}{h}, \quad \overline{y} = \frac{y}{h}, \quad \overline{t} = \frac{D_s t}{h^2} \tag{3.28}$$

Time has been made nondimensional by the surfactant diffusion time across the height of the flow cell. For the dependent concentration variables we introduce the following scaled variables:

$$\overline{c}_e = \frac{c_e}{c_{e,0}}, \quad \overline{c}_s = \frac{c_s}{c_{s,0}}, \quad \overline{\gamma}_e = \frac{\gamma_e}{\gamma_{\mathrm{m},e}}, \quad \overline{\gamma}_s = \frac{\gamma_s}{\gamma_{\mathrm{m},s}} \tag{3.29}$$

where $c_{e,0}$ and $c_{s,0}$ are the bulk concentrations injected at the inlet of the flow cell ($x = 0$). The following dimensionless parameters are defined:

$$\mathrm{Pe}_s = \frac{v_m h}{D_s}: \quad \text{Peclet number based on surfactant diffusion} \tag{3.30a}$$

$$\mathrm{Bi}_e = \frac{k_{\mathrm{a},e}\gamma_{\mathrm{m},e} h}{D_e}: \quad \text{enzyme Biot number} \tag{3.30b}$$

$$\mathrm{Bi}_s = \frac{k_{\mathrm{a},s}\gamma_{\mathrm{m},s} h}{D_s}: \quad \text{surfactant Biot number} \tag{3.30c}$$

$$d = \frac{D_e}{D_s}: \quad \text{ratio of enzyme and surfactant diffusion coefficients} \tag{3.30d}$$

$$\overline{k}_{\mathrm{c}} = \frac{k_{\mathrm{c}}\gamma_{\mathrm{m},e} h}{D_e c_{e,0}}: \quad \text{Nondimensional competition constant} \tag{3.30e}$$

$$K_s = \frac{k_{\mathrm{d},s}}{k_{\mathrm{a},s} c_{s,0}}: \quad \text{surfactant kinetic equilibrium constant} \tag{3.30f}$$

$$\overline{c}_{e,0} = \frac{c_{e,0} h}{\gamma_{\mathrm{m},e}}: \quad \text{Nondimensional inlet enzyme concentration} \tag{3.30g}$$

$$\overline{c}_{s,0} = \frac{c_{s,0} h}{\gamma_{\mathrm{m},s}}: \quad \text{Nondimensional inlet surfactant concentration} \tag{3.30h}$$

In terms of these nondimensional variables and parameters, and the definitions $f(\overline{y}) = 4\overline{y}(1-\overline{y})$, $\overline{\nabla}^2 = \partial^2/\partial\overline{x}^2 + \partial^2/\partial\overline{y}^2$ we obtain the nondimensional evolution equations. For the bulk concentration fields (Eq. (3.1)):

$$\frac{\partial \overline{c}_e}{\partial \overline{t}} + \mathrm{Pe}_s f(\overline{y}) \frac{\partial \overline{c}_e}{\partial \overline{x}} = d\overline{\nabla}^2 \overline{c}_e, \qquad \Omega \tag{3.31a}$$

$$\frac{\partial \overline{c}_s}{\partial \overline{t}} + \mathrm{Pe}_s f(\overline{y}) \frac{\partial \overline{c}_s}{\partial \overline{x}} = \overline{\nabla}^2 \overline{c}_s, \qquad \Omega \tag{3.31b}$$

The boundary conditions (Eq. (3.2b)) become

$$\left.\frac{\partial \overline{c}_e}{\partial \overline{y}}\right|_{\overline{y}=0} = \mathrm{Bi}_e \overline{c}_e|_{\overline{y}=0}(1-\overline{\gamma}_s-\overline{\gamma}_e) - \overline{k}_\mathrm{c}\overline{\gamma}_s\overline{\gamma}_e, \qquad \partial\Omega_\mathrm{ads} \tag{3.32a}$$

$$\left.\frac{\partial \overline{c}_s}{\partial \overline{y}}\right|_{\overline{y}=0} = \mathrm{Bi}_s \overline{c}_s|_{\overline{y}=0}(1-\overline{\gamma}_s-\overline{\gamma}_e) - K_s\mathrm{Bi}_s\overline{\gamma}_s, \qquad \partial\Omega_\mathrm{ads} \tag{3.32b}$$

The nondimensional evolution equations for the surface concentration fields are finally given by

$$\frac{\partial \overline{\gamma}_e}{\partial \overline{t}} = \mathrm{Bi}_e d\overline{c}_{e,0}\overline{c}_e|_{\overline{y}=0}(1-\overline{\gamma}_s-\overline{\gamma}_e) - \overline{k}_\mathrm{c} d\overline{c}_{e,0}\overline{\gamma}_s\overline{\gamma}_e, \qquad \partial\Omega_\mathrm{ads} \tag{3.33a}$$

$$\frac{\partial \overline{\gamma}_s}{\partial \overline{t}} = \mathrm{Bi}_s \overline{c}_{s,0}\overline{c}_s|_{\overline{y}=0}(1-\overline{\gamma}_s-\overline{\gamma}_e) - K_s\mathrm{Bi}_s\overline{c}_{s,0}\overline{\gamma}_s, \qquad \partial\Omega_\mathrm{ads} \tag{3.33b}$$

Again, the remaining no-flux boundary conditions are trivially translated into the nondimensional form for both molecular components.

3.4.3 Estimates of nondimensional parameters

In this section we estimate some reasonable values for the nondimensional parameters for the bimolecular system. As for the unimolecular system, flow rates are in the range $Q = 1 - 100\,\mu\mathrm{Lmin}^{-1}$, amounting to maximum velocities of $v_m = 3Q/2hw = 10^{-3} - 10^{-1}\,\mathrm{ms}^{-1}$. A diffusion coefficient for the enzyme was estimated in section 3.3.3, using the Stokes-Einstein relation $D = k_\mathrm{B}T/6\pi\mu R \approx 10^{-10}\,\mathrm{m}^2\mathrm{s}^{-1}$. The smaller surfactant molecules diffuse faster. Considering for example surfactant molecules of linear size $5\times10^{-10}\,\mathrm{m}$, which is one order of magnitude smaller than the enzyme, leads to a diffusion coefficient of approximately $10^{-9}\,\mathrm{m}^2\mathrm{s}^{-1}$. This leads to Peclet numbers, based on the surfactant diffusion coefficient, of order $\mathrm{Pe}_s \approx 5\times10^2 - 5\times10^4$, and $d = D_e/D_s \approx 10^{-1}$. Also, from section 3.3.3, $c_{e,0} \approx 1\,\mu\mathrm{M}$, and hence $\overline{c}_{e,0} = c_{e,0}h/\gamma_{\mathrm{m},e} \approx 1$. The injection concentration of surfactant is typically two orders of magnitude higher, dependent on the cmc for the particular surfactant. In addition, the maximum surface capacity $\gamma_{\mathrm{m},s}$ is typically a few times smaller. A rough estimate may be that $\overline{c}_{s,0} = c_{s,0}h/\gamma_{\mathrm{m},s} \approx 100$.

The set of parameters $(\mathrm{Bi}_e, \mathrm{Bi}_s, \overline{k}_\mathrm{c}, K_s)$ characterizes adsorption, desorption and competition, and would typically be the quantitative objective of adsorption experiments.

3.5 The quasi-steady theory

The theoretical models developed in the earlier sections 3.2, 3.3, and 3.4 all entail numerical simulations. The models have the mathematical structure of nonlin-

ear systems of partial differential equations, which require somewhat demanding numerical techniques. Analytical studies of these models are few, hence they are unfit for use in experimental data analysis, and this kind of modeling have therefore not been widely embraced by the SPR community. This section is concerned with a widely adopted approximate theory, which we refer to as the quasi-steady theory.

Ideally one would like to interpret SPR data by assuming simply that the concentration near the sensor $c_{y=0}$ is identical to the injection concentration c_0. That is, by assuming that there is no resistance to mass transfer. To account for the corrections due to some mass transfer resistance, it has been suggested to interpret data by means of a mass transport model, saying that the overall flux of solute J to the surface is proportional to the difference between the far field concentration c_0, usually taken as the injection concentration, and the concentration close to the surface of the sensor $c|_{y=0}$, i.e. $J = k_{\mathrm{L}}(c_0 - c|_{y=0})$. In fact, this suggestion is based on a solution to the stationary diffusion-convection equation for the concentration field $c = c(x, y)$ on a semi-infinite domain $x, y \geq 0$

$$v_x \frac{\partial c}{\partial x} = D \frac{\partial^2 c}{\partial y^2}, \quad y > 0. \tag{3.34}$$

The velocity $v_x = v_x(y)$ is linearized close to the surface, i.e. $v_x(y) = \dot{\gamma}_{\mathrm{w}} y$, $\dot{\gamma}_{\mathrm{w}}$ being the shear rate at the surface, and the boundary conditions for the concentration field are $c(x, y)|_{y=0} = const$, $c(x, y)|_{x,y\to\infty} = 0$, and $c(x, y)|_{x=0} = c_0$. The solution consists of a concentration boundary layer close to the surface $y = 0$, and a flux of solute to the surface $J = k_{\mathrm{L}}(c_0 - c|_{y=0})$, where the mass transport parameter k_{L} is given by

$$k_{\mathrm{L}} = \frac{2D}{\Gamma(\frac{7}{3})} \left(\frac{\dot{\gamma}_{\mathrm{w}}}{9Dl} \right)^{1/3}. \tag{3.35}$$

This mass transport parameter is often chosen as a free fitting parameter in the SPR community, although it may in fact be predicted from the operating conditions. Given a flow rate Q, the shear rate at the wall is

$$\dot{\gamma}_{\mathrm{w}} = \frac{6Q}{h^2 w} \tag{3.36}$$

The coupling of this stationary convection-diffusion solution with the adsorption kinetics on the surface is performed by loosening up the Dirichlet boundary condition $c(x, y)|_{y=0} = const$. Letting these bulk particles $c|_{y=0}$ adsorb, they are converted into surface particles γ, and a simple mass balance on the surface dictates $J = d\gamma/dt = \mathcal{A}(\gamma, c)$. The critical assumption here is that the adsorption is

so slow, that the bulk concentration on the surface $c|_{y=0}$ is practically constant, and use of the steady-state flux $J = k_{\mathrm{L}}(c_0 - c|_{y=0})$, with k_{L} given by Eq. (3.35), is still reasonable.

Inserting the steady-state flux into the mass balance on the surface yields $k_{\mathrm{L}}(c_0 - c|_{y=0}) = \mathcal{A}(\gamma, c)$. In the case of linear kinetics (Eq. (3.5)) this becomes an algebraic equation for $c|_{y=0}$, with the solution

$$c|_{y=0} = \frac{k_{\mathrm{L}} c_0 + k_{\mathrm{d}}\gamma}{k_{\mathrm{a}}(\gamma_{\mathrm{m}} - \gamma) + k_{\mathrm{L}}} \tag{3.37}$$

Substituting this into Eq. (3.5) gives the following nonlinear ordinary differential equation for the evolution of the surface concentration $\gamma(t)$

$$\frac{d\gamma}{dt} = \frac{k_{\mathrm{a}} k_{\mathrm{L}} c_0(\gamma_{\mathrm{m}} - \gamma) - k_{\mathrm{d}} k_{\mathrm{L}}\gamma}{k_{\mathrm{a}}(\gamma_{\mathrm{m}} - \gamma) + k_{\mathrm{L}}} \tag{3.38}$$

Using the kinetic scaling from section 3.3, we can write Eq. (3.38) as

$$\frac{d\overline{\gamma}}{d\overline{t}}^{\mathrm{ks}} = \frac{1 - (1+K)\overline{\gamma}}{1 + \mathrm{Da}(1 - \overline{\gamma})} \tag{3.39}$$

with the additional introduction of the important dimensionless Damköhler number

$$\mathrm{Da} = k_{\mathrm{a}}\gamma_{\mathrm{m}}/k_{\mathrm{L}}, \tag{3.40}$$

which is the ratio of the adsorption rate and the rate of mass transport to the surface, i.e. it measures the limiting effect of convection-diffusion on the adsorption process. If $\mathrm{Da} \ll 1$ the system is kinetically limited, and if $\mathrm{Da} \gg 1$ the system is convection-diffusion limited. Note in particular when $\mathrm{Da} \ll 1$ Eq. (3.39) becomes

$$\frac{d\overline{\gamma}}{d\overline{t}}^{\mathrm{ks}} = 1 - (1+K)\overline{\gamma}, \qquad \mathrm{Da} \ll 1 \tag{3.41}$$

which is simply the dimensionless form of Eq. (3.5), i.e. a purely adsorption-limited, linear, first order kinetic process. Also, the initial rate of adsorption, starting from the initial condition of zero surface concentration, $\overline{\gamma} = 0$, is predicted to be

$$\frac{d\overline{\gamma}}{d\overline{t}}(0)^{\mathrm{ks}} = \frac{1}{1+\mathrm{Da}} \quad \text{or} \quad \frac{d\gamma}{dt}(0)^{\mathrm{ks}} = c_0 k_{\mathrm{L}} \frac{\mathrm{Da}}{1+\mathrm{Da}} \tag{3.42}$$

Using diffusion scaling the formulation of the quasi-steady theory involves the two additional parameters, Bi and $\overline{c}_0$, viz

$$\frac{d\overline{\gamma}}{d\overline{t}}^{\mathrm{ds}} = \frac{\mathrm{Bi}\overline{c}_0(1 - \overline{\gamma}) - K\overline{\gamma}}{\mathrm{Da}(1 - \overline{\gamma}) - 1} \tag{3.43}$$

By combining Eq. (3.39) with Eq. (3.35) we obtain the scaling of the maximum rate of adsorption with Peclet number in the convection-diffusion-limited regime ($\mathrm{Da} \gg 1$),

$$\max\left(\frac{d\bar{\gamma}}{d\bar{t}}\right) \sim \mathrm{Pe}^{1/3}. \tag{3.44}$$

3.5.1 Correspondence between the Damköhler, Biot, and Peclet number

The kinetic scaling of the evolution equations (Eqs. (3.8),(3.9),(3.10)) clarifies the assumptions in the quasi-steady theory. By setting $\mathrm{Bi} = 0$ we essentially obtain the conditions for the solution in Eq. (3.35), i.e. time dependency drops out of the bulk convection-diffusion equation, which is consistent with an instantaneous build-up of the concentration boundary layer above the adsorbing surface in the *quasi-steady* theory. In addition, the quasi-steady theory approximates reality by a semi-infinite bulk domain, a linear velocity profile, and equally important, by no inlet distance to the sensor surface. With the exception of the last difference, we expect that the quasi-steady theory can be obtained from a boundary layer perturbation theory. This work has however not been further pursued.

The kinetically scaled quasi-steady theory in Eq. (3.39) is parameterized only by the Damköhler number Da, and the equilibrium constant K. As the quasi-steady theory combines steady-state convection-diffusion with adsorption in the Damköhler number, through the mass transport coefficient k_L, it is naturally possible to express the Damköhler number in terms of the Peclet number and the Biot number. First, from Eq. (3.36), $\dot{\gamma}_\mathrm{w} = 4v_m/h$. By defining the number $\alpha = 2(4/9)^{1/3}/\Gamma(7/3) \approx 1.2819$, the mass transport coefficient k_L can be expressed as

$$k_\mathrm{L} = \alpha\left(\frac{v_m h}{D}\right)^{1/3}\frac{D}{l^{1/3}h^{2/3}}$$

Hence the Damköhler number is given by

$$\mathrm{Da} = \frac{k_\mathrm{a}\gamma_\mathrm{m}}{k_\mathrm{L}} = \alpha^{-1}(l/h)^{1/3}\,\mathrm{Bi}\,\mathrm{Pe}^{-1/3} \tag{3.45}$$

Note that the quasi-steady theory is parameterized by the Damköhler number, and at the same time is based on the assumption $\mathrm{Da} = 0$. It is clear from Eq. (3.45) that the Damköhler number increases linearly with the Biot number, and decreases with the cubic root of the Peclet number. Practically speaking, if the binders are strongly attracted to the surface (large Biot number), it may be impossible to reduce the Damköhler number significantly by simply increasing the flow rate, i.e. Peclet number.

3.5.2 Analytical solution of the quasi-steady theory

Eq. (3.39) can be solved analytically in *implicit* form, i.e. $\bar{t} = \bar{t}(\overline{\gamma})$ instead of the *explicit* form $\overline{\gamma} = \overline{\gamma}(\bar{t})$. It is determined simply by separation of variables and integration, with initially $\overline{\gamma}(\bar{t} = 0) = 0$:

$$\bar{t} = \frac{\mathrm{Da}\kappa\overline{\gamma} - \big(\kappa + \mathrm{Da}(\kappa - 1)\big)\ln(1 - \kappa\overline{\gamma})}{\kappa^2} \tag{3.46}$$

where $\kappa \equiv 1+K$. For irreversible adsorption $K = 0$, $\kappa = 1$, the solution condenses into

$$\bar{t} = \mathrm{Da}\overline{\gamma} - \ln(1 - \overline{\gamma}) \tag{3.47}$$

This solution may not be so useful for physical insight, but has its practical advantage when performing nonlinear least squares data fitting in the time domain. Data fitting in the time domain involves a numerical solution of the ordinary differential equation (Eq. (3.39)) at every parameter space iteration, which can be avoided with the *implicit* solution above. Another option is simply fitting data in the phase plane (Goren et al., 2006 Jan 31). This method does not involve the solution of Eq. (3.39), is *explicit*, but as a trade off involves differentiation of data.

3.5.3 Note on two-compartment model

The quasi-steady theory captures the qualitative essence of the mass transport problem in the microfluidic system of surface-based biosensors. In this respect the theory includes the coupling of convective and diffusive bulk mass transport with adsorption/desorption surface kinetics. To increase the quantitative accuracy of the model in the context of fitting data from surface-based biosensor experiments, a two-compartment model has been suggested (Schuck and Minton, 1996; Myszka et al., 1997 Feb 28, 1998 Aug). In this model the flow cell is divided into two compartments, an inner compartment directly adjacent to the sensor surface, and an outer compartment spanning the rest of the flow cell. The outer compartment is modeled with a uniform concentration equal to the injection concentration. Mass transport from the outer to the inner compartment is then modeled by a flux, linear in the concentration difference between the two compartments, like the quasi-steady flux, with the mass transport coefficient k_{L}. This mass transport coefficient is usually chosen as a free fitting parameter. The mass transport between the inner compartment and the surface is finally modeled by a first order kinetic adsorption/desorption scheme like in Eq. (3.5).

The two compartment model shows increased capabilities of fitting experimental data (Myszka et al., 1998 Aug). What happens is that the introduc-

tion of the two compartments renders the adsorption process second order, i.e. $d\gamma/dt(t = 0) = 0$. The inner compartment needs to receive solute binders from the outer compartment before being able to support adsorption onto the surface. This second order behavior is consistent with real adsorption experiments, where the concentration boundary adjacent to the SPR surface initially needs to build up by a time-dependent transient transport process. The drawback of the two-compartment model is the somewhat arbitrary specification of the inner compartment height, and thereby the definition of the compartments, altogether. Choosing the inner compartment height to zero leads back to the quasi-steady theory. The shortcomings of the quasi-steady theory, especially in the initial process of an adsorption experiment, is analyzed in detail in chapter 4.

Chapter 4

Numerical Analysis

This chapter presents some of the main results from numerical analysis of the mathematical models, introduced in chapter 3. From a theoretical point of view, much knowledge has been build up in this field (Bird et al., 2002). The aim of this first section is by no means to review this knowledge, but simply to build up some intuition about the transport physics in the surface-based biosensor, by visualization of the spatio-temporal evolution of the concentration fields. This part also serves to introduce the most important terminology used in this and related transport problems. The following section quantifies and compares transient convection, diffusion, and adsorption, obtained by numerical solutions of the evolution equations from chapter 3, with the quasi-steady theory. A major part of the results in this section is included in the paper, submitted for publication in the appendix [P1]. This is followed by a brief investigation of the case where the solute adsorbs equally well to all the surfaces in the flow cell. This could hypothetically occur for non-specific binding of highly surface active solutes, e.g. the experiments described in the following chapter.

4.1 Numerical method

All numerical simulations are performed with the ComSol/MatLab finite element method software. The method is implemented in MatLab 7, which calls a set of functions running in ComSol 3 that perform the numerical simulations of the given problem. The implementation is based on the weak formulation derived in section 3.3.4. The time stepping procedure is an implicit backward Euler method, which uses a variable order differentiation formula. The level of meshing is increased until the solver converges, and the concentrationen fields, as well as derived functions such as the mean value of surface concentration, appear smooth. A convergence test is performed automatically by the program. An additional

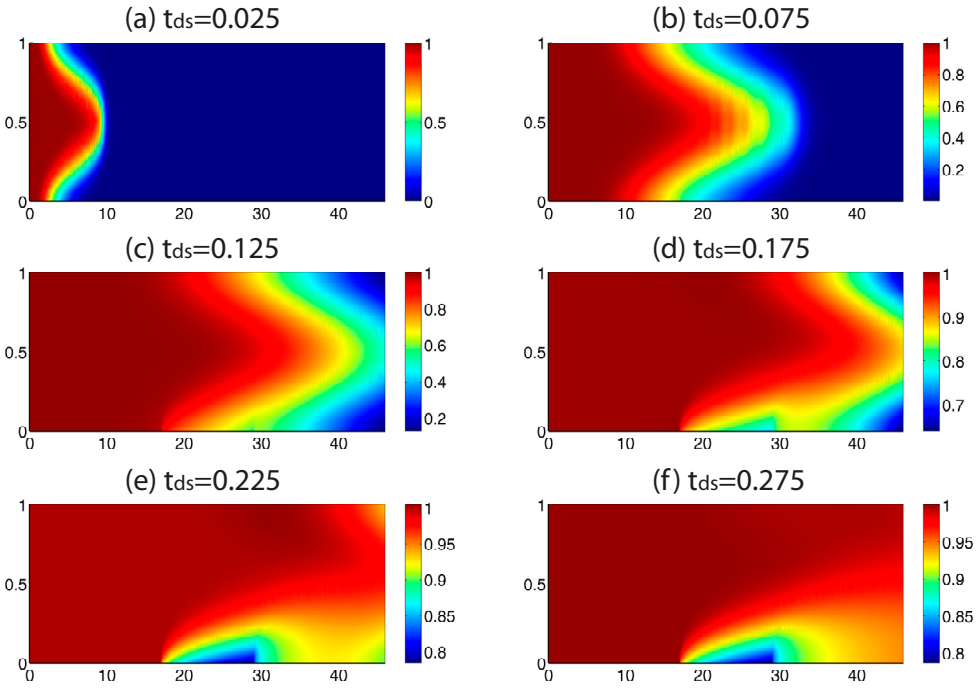

Figure 4.1: Evolution of the bulk concentration field in the flow cell - The plots (a)-(f) correspond to equidistant times. Time is made nondimensional by diffusion scaling: $t_{\mathrm{ds}} = tD/h^2$. Parameters: $\overline{c}_0 = 1$, Pe $= 500$, Bi $= 1$

test for convergence is done by comparing the solutions with the quasi-steady theory in the limit where this is known to be a good approximation. Aditional details on the numerical technique are not within the scope of the present thesis.

4.2 Evolution of the concentration fields

We take offset in the estimated regime for the nondimensional parameters in section 3.3.3, and, to simplify matters, choose to consider the case of irreversible adsorption of binders, which are immobile on the surface, hence $K = d_s = 0$. In nondimensional variables the height of the flow cell is 1, while the length is 46, and the chip length is 12. Fig. 4.1 presents the bulk concentration field in the flow cell for six equidistant times, made nondimensional by diffusion scaling: $t_{\mathrm{ds}} = tD/h^2$. The parameters are $\overline{c}_0 = 1$, Pe $= 500$, Bi $= 1$. In Fig. 4.1 (a)-(b)

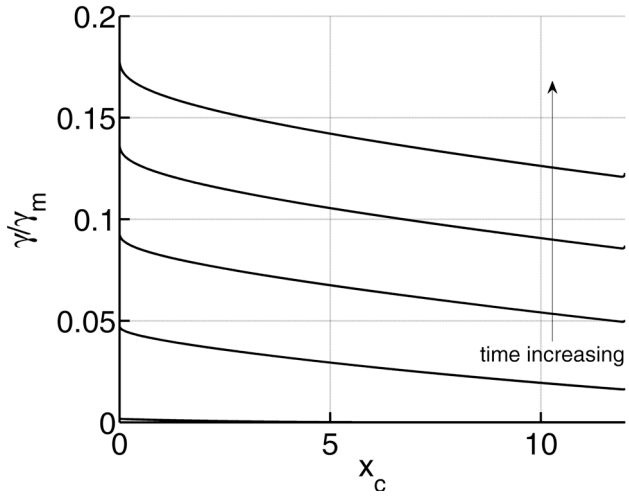

Figure 4.2: Evolution of the surface concentration field at the SPR chip - The curves correspond to the equidistant times from Fig. 4.1 (a)-(f). The abscissa x_c is the measure along the x-axis starting at the chip. Parameters: $\overline{c}_0 = 1$, Pe = 500, Bi = 1

we clearly see how the solute is convected by the parabolic velocity flow profile, while diffusion evens out the concentration field at the border to the buffer initially present in the flow cell. As time progresses further, going from Fig. 4.1 (b) to (f), we observe a transient formation of a concentration boundary layer above the surface of the adsorbing SPR chip. The adsorption causes a depletion locally above the chip. The system approaches a steady-state, where this depletion of the solute above the chip is balanced by the convection of fresh solute from the inlet of the flow cell. The physics of this steady-state boundary layer is theoretically well understood (Bird et al., 2002), and forms the basis for the quasi-steady theory of adsorption, as described in the preceding chapter in section 3.5. The steady-state is reached after the surface concentration has saturated, such that $\overline{\gamma} = \gamma/\gamma_{\mathrm{m}} = 1$. Fig. 4.2 shows the evolution of the surface concentration field $\overline{\gamma}$, corresponding to the equidistant times from Fig. 4.1 (a)-(f). For (a) and (b) only a minor amount of solute has adsorbed. From (c) to (f) the surface concentration increases almost linearly with time, while the surface is still far from saturation. The concentration decreases with downstream distance due to the earlier encounter with bulk solute in the beginning of the chip, and the thinner boundary layer in this region.

Fig. 4.3 compares the bulk concentration field for different parameters at the

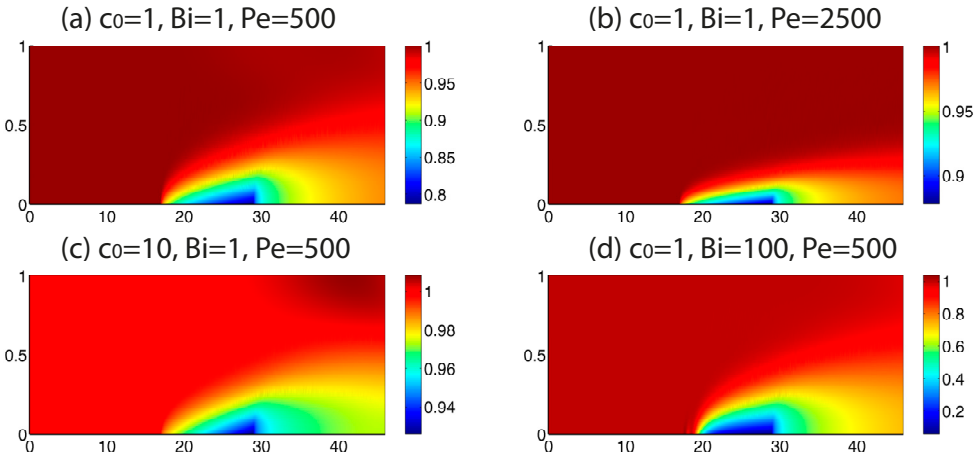

Figure 4.3: Bulk concentration field in the flow cell at the time $t_{\mathrm{ds}} = 0.275$ - Parameters are indicated above each plot.

fixed time $t_{\mathrm{ds}} = 0.275$.

Effect of Peclet number

The effect of increasing the Peclet number from 500 to 2500, with fixed parameters $\overline{c}_0 = 1$ and $\mathrm{Bi} = 1$, is seen by comparing Fig. 4.3 (a) and (b). The process of developing the boundary layer is speeded up by the increase in Peclet number, which is followed by a faster adsorption process, as long as the system is convection-diffusion-limited. The boundary layer is qualitatively preserved, but undergoes a quantitative change, under the increase in Peclet number. In accordance with theory, the height of the boundary layer decreases with Peclet number. Steady-state theory for large Peclet numbers ($\mathrm{Pe} \gg 1$) predicts that the height of the boundary layer scales with $\mathrm{Pe}^{-1/3}$ (Bird et al., 2002). Additionally, the nondimensional concentration $\overline{c}$ within the boundary layer has increased with Peclet number. In this way, increasing the Peclet number leads to conditions, which are closer to those assumed in a rapid mixing model, where the bulk concentration field just above the chip is put equal to the injection concentration. Also, the conditions get closer to those assumed assumed in the quasi-steady theory. However, the relative increase in the boundary layer concentration is only in the order of 10^{-1}, or 10 percent, which should be seen in the light of the 5-fold increase in Peclet number.

Effect of inlet concentration

The effect of increasing the nondimensional inlet concentration $\overline{c}_0$ from 1 to 10, with fixed parameters Bi = 1 and Pe = 500, is seen by comparing Fig. 4.3 (a) and (c). The most notable effect is a decrease in the nondimensional concentration gradients across the boundary layer.

Effect of Biot number

The effect of increasing the Biot number from 1 to 100, with fixed parameters $\overline{c}_0 = 1$ and Pe = 500, is seen by comparing Fig. 4.3 (a) and (d). In this case the most notable effect is a more pronounced depletion of the bulk concentration field above the adsorbing chip. This leads to increased nondimensional concentration gradients across the boundary layer.

4.3 Transient transport in surface-based biosensors

This section is concerned with a numerical investigation of the nonlinear system of partial differential equations, governing the evolution of the concentration fields. The intention is to simulate the dynamics of real adsorption experiments in surface-based biosensors, whereby we use the mean surface concentration $\Gamma \equiv (1/l_c) \int_{sensor} \overline{\gamma}\, dx$ as the central quantifier. Numerical solutions to Eqs. (3.8), (3.9), and (3.10), or similarly Eqs. (3.12), (3.13), and (3.14), are collectively referred to as the *simulations*. We take offset in the estimated regime for the nondimensional parameters, and to simplify matters choose to consider the case of irreversible adsorption of binders, which are immobile on the surface, hence $K = d_s = 0$. A particular aim of the investigation is to evaluate the quality of the quasi-steady theory by comparison with the simulations. Deviations between the simulations and the quasi-steady theory reveal the effects of the transient dynamics in the simulations, which of course are also present in real adsorption experiments. To mimic the case of real adsorption experiments, being fitted by the quasi-steady theory to reveal an adsorption rate constant k_a, we fit the quasi-steady theory to the simulation with Bi as the free fitting parameter, using a least squares method. The quasi-steady theory has no chance of fitting initial data, hence the simulation time from the origin of the phase plane to the extremum (highest adsorption rate) is cut off in the fitting procedure, corresponding to typical practice of representing SPR data in the phase plane (Goren et al., 2006 Jan 31). The error of the quasi-steady theory is then quantified by the relative difference between the fitted Bi number and the real Bi number used for the simu-

lation. Strictly speaking, we define the error as $(\mathrm{Bi}^{\mathrm{fit}} - \mathrm{Bi})/\mathrm{Bi}$. Being interested in the kinetics of adsorption the results are most naturally presented and analyzed in the phase plane, spanned by the mean surface concentration Γ, and its time derivative $\dot{\Gamma} \equiv (1/l_{\mathrm{c}}) \int_{sensor} \partial\overline{\gamma}/\partial\overline{t}\, dx$. This representation clearly illustrates the transient regime, and is the most straightforward approach to analyze deviations from linear adsorption kinetics due to mass transport. The choice of parameters span both kinetically limited and convection-diffusion limited dynamics. Results are presented using both kinetic and diffusion scaling of time, the former leading to universality for kinetically limited dynamics, and the latter leading to universality for convection-diffusion limited dynamics. Note in particular that purely kinetically limited dynamics, i.e. the linear kinetics in 3.5, is represented by a linear curve in the phase plane. For kinetic scaling this linear curve is the diagonal from the point $(0, 1)$ on the ordinate to the point $(1, 0)$ on the abscissa. The universality characteristic obtained with kinetic scaling is that this curve represents the dynamics independent of $\overline{c}_0$ and Pe for large enough Bi.

4.3.1 Kinetic scaling

Fig. 4.4 contains a representative collection of phase plane curves using kinetic scaling, i.e. $\overline{t}^{\mathrm{ks}} = k_{\mathrm{a}} c_0 t$. Four different simulations for the combinations of concentrations $\overline{c}_0 \in \{1, 20\}$, $\mathrm{Bi} \in \{1, 10\}$, and $\mathrm{Pe} = 500$ are presented (full black line), each in a separate plot, along with the prediction of the quasi-steady theory for identical parameters (dashed black line), as well as a fit of the quasi-steady theory to the simulations (dashed gray line). Importantly, the quasi-steady theory scales linearly with $\overline{c}_0$, taken into account in the kinetic scaling of time in 3.39. Hence the quasi-steady theory does not explicitly include the $\overline{c}_0$ - degree of freedom, whereby essentially only two distinctive predictions occur in Fig. 4.4. In other words, the dashed curves denoted (QST) are identical in Fig. 4.4 (a) and (b), respectively, Fig. 4.4 (c) and (d). Several points are immediately apparent from the simulations. The simulation curves start at the origin of the phase plane, whereas the quasi-steady theory has the finite initial adsorption rate given in 3.42. It is important to note that the kinetic scaling of time implicitly includes a linear scaling of the adsorption rate with both Bi and $\overline{c}_0$. The decrease in adsorption rate for both increasing Bi and increasing $\overline{c}_0$ in Fig. 4.4, amounts to a sublinear increase with both Bi and $\overline{c}_0$ in dimensional variables. The sublinear scaling naturally arises from convection-diffusion limitation in the nonlinear dynamics of the system. Apart from in the initial phase, predictions of the quasi-steady theory practically coincides with the simulations, and thereby also the fits, for $\overline{c}_0 = 1$. Increasing the concentration to $\overline{c}_0 = 20$ leads to significant alteration of the simulation curves. Since there are no knobs to turn for the kinetically scaled quasi-steady theory, regarding changes in concentration $\overline{c}_0$, this leads to equally

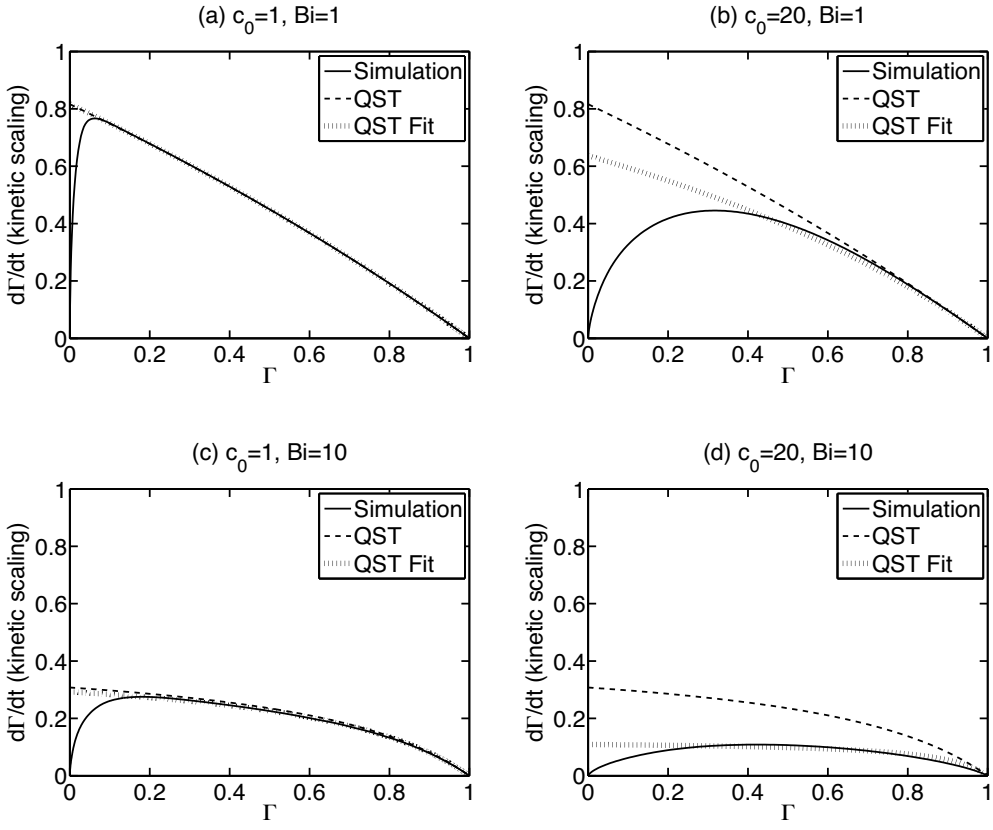

Figure 4.4: Phase plane dynamics using kinetic scaling - Simulation: Numerical solution of Eqs. (3.8), (3.9), and (3.10) for $\bar{c}_0 \in \{1, 20\}$, $\mathrm{Bi} \in \{1, 10\}$, and $\mathrm{Pe} = 500$. QST: Quasi-steady theory (3.39) for corresponding values of Da through Eq. (3.45). QST Fit: Fits of the quasi-steady theory to simulations.

significant deviations between the simulations and predictions of the quasi-steady theory. The observed dependency of $\bar{c}_0$ is expected since $\bar{c}_0$ parameterizes time dependency in 3.8, and hence transient behavior in the system dynamics, which is not taken into account in the quasi-steady theory. Physically speaking, the surface simply saturates faster than a steady-state can be achieved in the bulk.

4.3.2 Diffusion scaling

Fig. 4.5 contains a representative collection of phase plane curves using diffusion scaling, i.e. $\bar{t}^{\mathrm{ds}} = Dt/h^2$. Four different simulations for the combination of parameters $\bar{c}_0 \in \{20\}$, $\mathrm{Bi} = \{1, 10, 50, 100\}$, and $\mathrm{Pe} = 2500$ are presented, each in a separate plot, along with the prediction of the quasi-steady theory for identical parameters, as well as a fit of the quasi-steady theory to the simulations. The universality characteristic obtained with diffusion scaling of time is that the simulations approach a limiting curve, representing predominantly convection-diffusion limited dynamics, for large Biot numbers. This curve is observed to

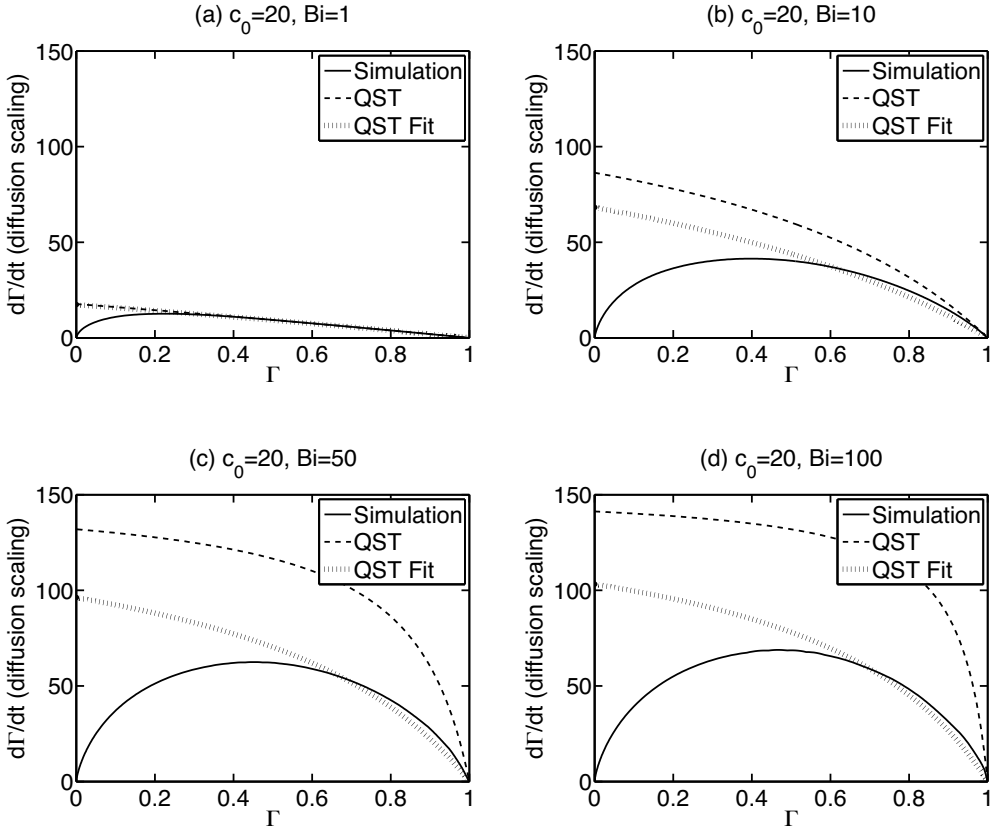

Figure 4.5: Phase plane dynamics using diffusion scaling - Simulation: Numerical solution of Eqs. (3.12), (3.13), and (3.14) for $\bar{c}_0 \in \{1, 20\}$, $\mathrm{Bi} = \{1, 10\}$, and $\mathrm{Pe} = 500$. QST: Quasi-steady theory (3.43) for corresponding values of Da through Eq. (3.45). QST Fit: Fits of the quasi-steady theory to simulations.

have a very symmetric, parabolic-like, characteristic form. Inconsistent with the simulations, quasi-steady theory predicts a linear scaling of adsorption rate with concentration, which is explicit when using diffusion scaling as in Fig. 4.5. This naturally leads to an increasing deviation between quasi-steady theory and simulations for increasing Bi.

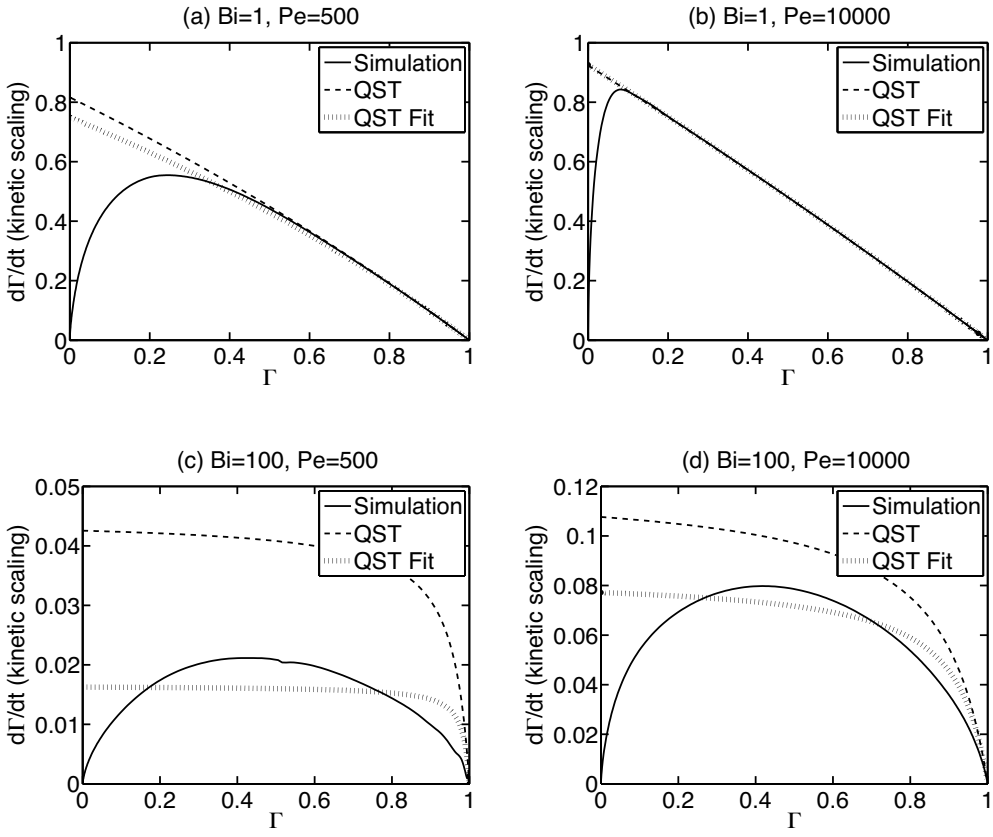

Figure 4.6: Phase plane dynamics showing effect of the flow rate (Pe number) - Simulation: Numerical solution of Eqs. (3.8), (3.9), and (3.10) for $\bar{c}_0 = 10$, Bi $= \{1, 100\}$, and Pe $= \{500, 10000\}$. QST: Quasi-steady theory (Eq. (3.43)) for corresponding values of Da though Eq. (3.45). QST Fit: Fits of the quasi-steady theory to simulations.

4.3.3 Flow rate dependency

The nature of the Peclet number dependency is presented in Fig. 4.6, containing four different simulations for the combination of parameters $\bar{c}_0 = 10$, $\mathrm{Bi} = \{1, 100\}$, and $\mathrm{Pe} = \{500, 10000\}$. Again, the simulations are presented, each in a separate plot, along with the prediction of the quasi-steady theory for identical parameters, as well as a fit of the quasi-steady theory to the simulations. Kinetic scaling, i.e. $\bar{t}^{\mathrm{ks}} = k_{\mathrm{a}} c_0 t$ is applied. Clearly the increase of the Peclet number leads to less convection-diffusion limitation. Thereby the simulations approach the diagonal in Fig. 4.6, representing purely adsorption limited linear kinetics, for increasing Pe. This behavior is very clear for $\mathrm{Bi} = 1$, where the dynamics is predominantly kinetically limited. For $\mathrm{Bi} = 100$, where the dynamics is much more convection-diffusion limited, we again observe increased agreement between quasi-steady theory and simulations as the Peclet number is increased. The agreement is, however, not as good as for $\mathrm{Bi} = 1$. Note that the ordinate axis are different in the two lower plots for $\mathrm{Bi} = 100$. The specific case in the lower left plot ($\bar{c}_0 = 10$, $\mathrm{Bi} = 100$, $\mathrm{Pe} = 500$) is clearly in a regime where the quasi-steady theory has little value, and little ability to fit data as well. The approach to adsorption limited dynamics in Fig. 4.6 is consistent with a decrease in the Damköhler number as $\mathrm{Da} \sim \mathrm{Pe}^{-1/3}$. Fig. 4.6 also serves to show that, due to this slow cubic root dependency, experimental practicalities often preclude to cope with convection-diffusion limitation, by simply increasing the flow rate for systems with a high Biot number.

In summary, Figs 4.4, 4.5, and 4.6 stress some nonlinearities present in the real system dynamics, which are not well captured in the approximate quasi-steady theory.

4.3.4 Error of the quasi-steady theory

The numerical investigation concludes with a quantification of the error of the quasi-steady theory, measured as the relative difference between the Biot number used to fit the quasi-steady theory to simulations, and the Biot number used for the simulation itself. The nondimensional parameter space is spanned by $\mathrm{Bi} \in \{1, \ldots, 100\}$, $\mathrm{Pe} \in \{500, \ldots, 10000\}$, for $\bar{c}_0 = \{1, 10, 20\}$. Fig. 4.7 presents the relative errors $(\mathrm{Bi}^{\mathrm{fit}} - \mathrm{Bi})/\mathrm{Bi}$ by contour lines in the nondimensional parameter space $(\mathrm{Pe}, \mathrm{Bi})$. Every contour is labelled with the matching error. Equal for all values of $\bar{c}_0$ is that the error is largest for slow flows of strong binders, i.e. small Pe and large Bi numbers. For $\bar{c}_0 = 1$ only relatively minor errors, up to around 0.2 (20%), are observed in the spanned parameter space. However, the quantitative increase of the error with $\bar{c}_0$ is significant. For $\bar{c}_0 = 20$ the errors increase to above

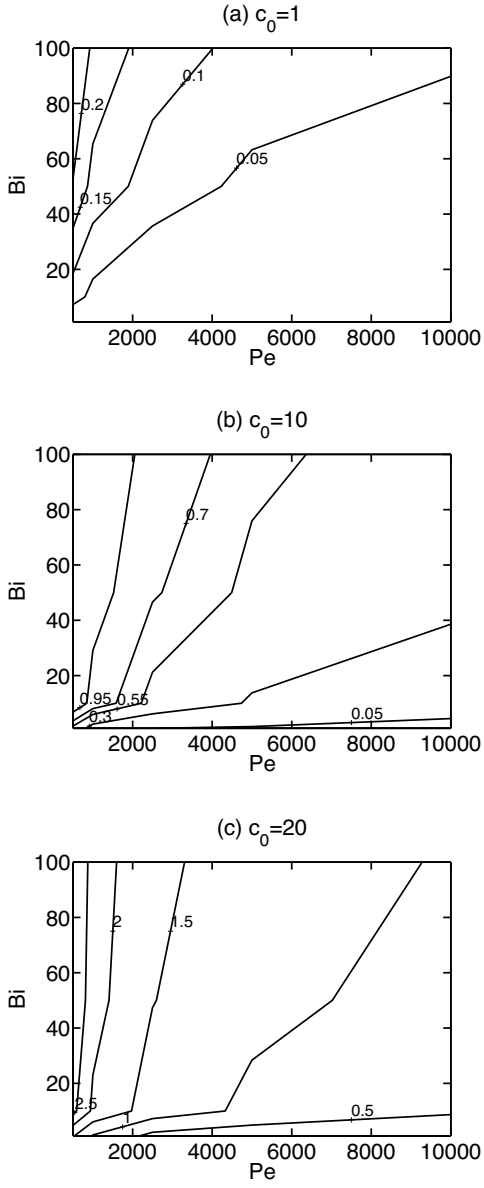

Figure 4.7: Error of quasi-steady theory - Contour lines of the relative error $(\mathrm{Bi}^{\mathrm{fit}} - \mathrm{Bi})/\mathrm{Bi}$ for $\bar{c}_0 \in \{1, 10, 20\}$ in the parameter space $(\mathrm{Pe}, \mathrm{Bi})$. The errors increase with increasing Bi, increasing $\bar{c}_0$, and decreasing Pe.

2.5 (250%), which amounts to a factor of 3-4, in the spanned parameter space.

4.3.5 Effect of preadsorption

For highly surface active molecules undergoing nonspecific adsorption one could expect that solute adsorbs equally well to all surfaces in the microfluidic flow cell. This final investigation for the unimolecular system concerns the characteristic effects of such dynamics on the SPR signal. We refer to this as *preadsorption*, even though adsorption is modeled both upstream, downstream, and on the surface opposite the sensor. Fig. 4.8 compares the phase plane dynamics, with and without preadsorption, for the parameters; $\overline{c}_0 = 1$, Bi $= \{1, 100\}$, and Pe $=$

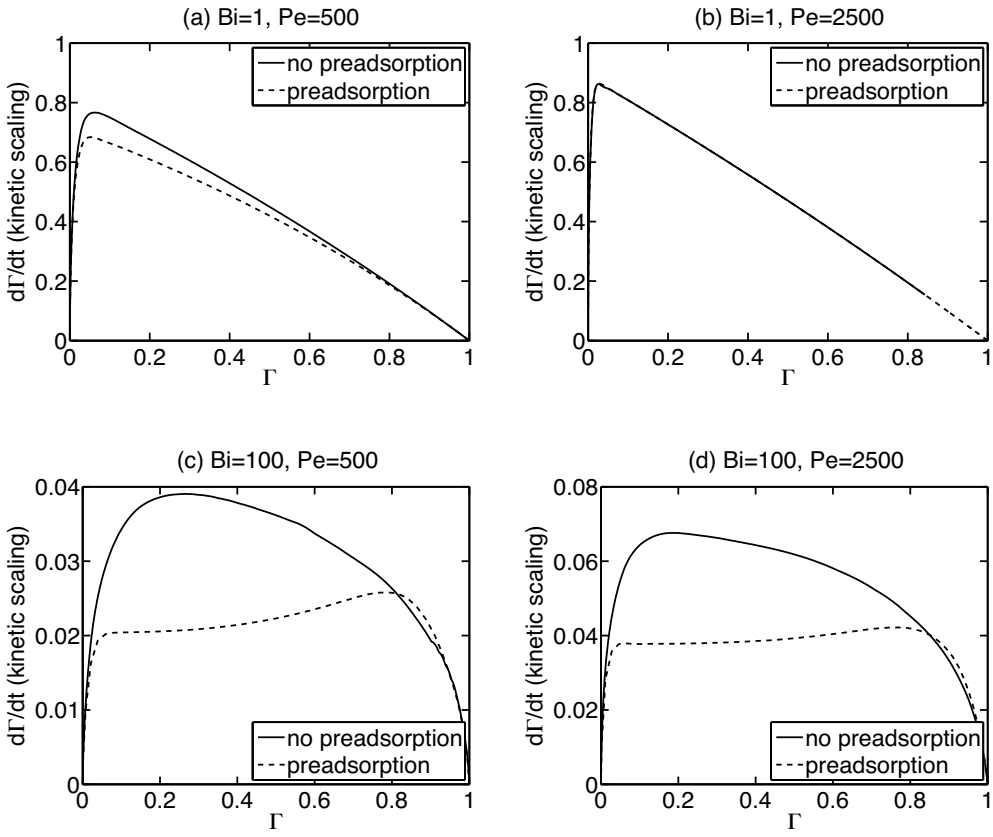

Figure 4.8: Effect of preadsorption on phase plane dynamics. - Parameters are indicated above each plot. $\overline{c}_0 = 1$ for all plots.

$\{500, 2500\}$. In the regime of low Bi and high Pe (Bi = 1, Pe = 2500) the effect of preadsorption is vanishing. For high Bi (Bi = 100) the effect is much more pronounced, even under a increase in the flow rate from Pe = 500 to Pe = 2500. Also, for high Bi and low Pe, the phase plane curve has a characteristic shape with a convex region for intermediate values of Γ. This essentially means that the adsorption rate initially increases, and then starts decreasing, as usual, but then starts increasing again as the surfaces surrounding the sensor surface get saturated.

4.3.6 Summary of results

The nondimensional Damköhler number Da = $k_{\mathrm{a}}\gamma_{\mathrm{m}}/k_{\mathrm{L}}$, inherent in the quasi-steady theory, was expressed in terms of the Biot number Bi = $k_{\mathrm{a}}\gamma_{\mathrm{m}}h/D$, the Péclet number Pe = $v_m h/D$, and the model geometry. In addition, an analytical solution to the quasi-steady theory was derived. The results provided the regimes of both reliable and unreliable use of the quasi-steady theory for experimental data analysis, by quantifying the error of the quasi-steady theory in the space of parameters. This can be used as a tool to correct adsorption rate constants, obtained by fitting the quasi-steady theory to experimental data. We deduced a critical importance of the inlet concentration, and the maximum surface capacity, combined in the nondimensional inlet concentration. Finally, inclusion of adsorption on all the surfaces lead to a pronounced effect on the dynamics of adsorption for large Biot numbers.

Chapter 5

SPR experiments of lipase adsorption

This chapter presents some of the main experimental results obtained during the thesis. After a short review of lipase, the experimental method and protocol is introduced. This is followed by a presentation and discussion of data obtained for lipase adsorption in the absence, as well as presence, of surfactant.

5.1 Introduction

Enzymes are true workhorses as chemical catalysts in living matter. Most enzymes are very specific in the sense of catalyzing chemical reactions of particular reactant molecules called substrates. Using genetic engineering the chemical composition of an enzyme can be altered by mutations, creating different *mutant* variants. This has been widely adopted by the chemical and biotechnological industry to achieve high performance mutant variants of naturally occurring wild type enzymes.

Lipases are enzymes that facilitate degradation of lipids and fats, a process referred to as lipolysis. They are ubiquitous in nature, playing many essential roles in e.g. the digestive system, remodeling of membranes, and in forming the permeability barrier of the skin (Mouritsen, 2005). More technically, the degradation of lipids and fats by lipases is executed by catalysis of hydrolysis of ester bonds in triglycerides. This important property is naturally utilized in industrial detergent formulations, where lipases play a key role in removing fatty soils. As lipases are water soluble, whereas their lipid substrate is water insoluble, the catalytic reaction occurs on a water-oil interface. Upon adsorption to the lipid substrate the majority of known lipases undergoes an interfacial activation, composed of

conformational rearrangements on the lipid substrate (Cygler and Schrag, 1997; Reis et al., 2009). As a part of this interfacial activation a hydrophobic active site of the lipase gets exposed to the substrate (Brzozowski et al., 2000). In comparison with enzymatic catalysis in homogenous solutions, the complicated interfacial environment, in which lipolysis occurs, introduces challenges for understanding the regulation of lipolysis. One complicating factor is lipase adsorption and substrate availability (Reis et al., 2009). Another important aspect that complicates the physical system is the frequent presence of surfactants, which influences the lipase activity. For example, bile acids function as unconventional surfactants in the digestive system, where they are critical for reducing lipase product inhibition by promoting the solubilization of lipolytic products. In addition, they prepare the interface for lipase adsorption (Wilde and Chu, 2011; Maldonado-Valderrama et al., 2011). Surfactants are also an important ingredient in detergent formulations for solubilizing lipolytic products (Gennes et al., 2004).

Surfactants interact with both proteins and the lipid interface. Concordantly, the presence of surfactants has been demonstrated to influence the adsorption of lipase molecules to solid lipid interfaces (Sonesson et al., 2006, 2008), and the conformational stability of the enzyme (Mogensen et al., 2005). The effect of surfactant, however, is highly dependent on its concentration. At high concentrations surfactants tend to displace lipase molecules, either by replacement, or by binding to and solubilizing the lipase (Wahlgren and Arnebrant, 1991). Hence, the interactions between surfactants and lipase at the interface is important for regulation of lipid catalysis. The step of adsorption of lipase to the lipid substrate constitutes a potential target for modification to regulate lipolysis, and thereby take full advantage of these enzymes.

Thermomyces lanuginusos lipases (TLL, see Fig. 5.1) is a well-studied lipase, which has found technological application in detergent formulations (Schmid and Verger, 1998). Adsorption and mobility of TLL at interfaces has been investigated in a number of previous studies, addressing the influence of ionic strength and pH (Duinhoven et al., 1995), glycosylation (Pinholt et al., 2010; Schmid and Verger, 1998), and surface hydrophobicity (Wannerberger and Arnebrant, 1996; Wannerberger et al., 1996). Studies on how surfactants affect TLL adsorption dynamics revealed that surfactants can displace TLL from the interface, and that the mobility of TLL on a hydrophobic interface increase substantially in the presence of surfactants at concentrations above the cmc Sonesson et al. (2006, 2008).

To achieve more high performance enzymes, several TLL mutant variants have been designed using molecular genetics (communication with Novozymes). The present study compares the adsorbing properties of a high performance TLL

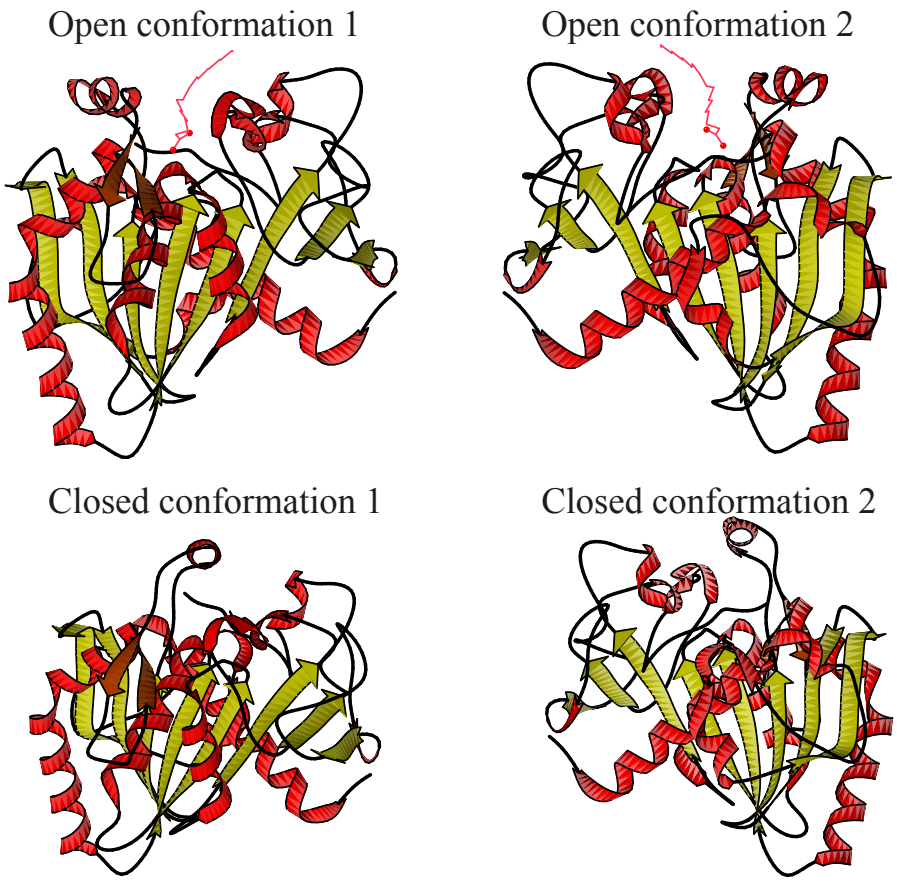

Figure 5.1: Thermomyces lanuginosus lipase (TLL) - Pictures are taken from the Protein Data Base. The crystal structure is obtained by x-ray diffraction. The lipase is shown in both its open (interfacial activated) and closed (bulk state) conformation at two different angles. In the open conformation a lipid molecule is indicated at the location of the catalytic active site of the lipase.

variant (MUT) with the wild type (WT) protein. We apply surface plasmon resonance (SPR) spectroscopy to investigate the adsorption dynamics onto a model hydrophobic surface both in the absence, and in the presence, of surfactant. The hydrophobic surface is established on the Biacore HPA chip and is designed to mimic the surface properties of naturally occurring lipid assemblies. In particular, we study the influence of the concentrations of lipase and surfactants, and the relative rates of arrival to the surface, by changing the injection flow rate.

5.2 Materials and methods

5.2.1 Lipases and solvent

Novozymes A/S (Bagsværd, Denmark) provided the wild type (WT) Thermomyces lanuginosus lipase (TLL), and a high performance mutant variant (MUT) of this wild type. Both variants have a molecular weight of about $M_{\mathrm{w}}^{\mathrm{l}} = 30 \times 10^3\,\mathrm{gmol}^{-1}$. The buffer used throughout all experiments was Hepes pH 7.0 (50 mM Hepes, 10 mM NaCl, 1 mM NaN_3). All water used was of Milli-Q grade.

5.2.2 Surfactant

In the competitive study presented in section 5.4, we apply a Polyoxyethylene (20) sorbitan monolaurate ($C_{58}H_{114}O_{26}$), also known as Tween 20, surfactant. It has a molecular weight of $M_{\mathrm{w}}^{\mathrm{s}} = 1227.54\,\mathrm{gmol}^{-1}$, and a cmc of approximately $80\,\mu$M at 21°C. It is a highly water soluble surfactants, with a HLB value of 16.7. The lipase variants were thawed at room temperature, and diluted in buffer, together with the surfactant, to appropriate concentrations immediately prior to the experiments.

5.2.3 Experimental protocol

The adsorption dynamics is measured using the SPR apparatus Biacore 3000 (Biacore, Uppsala, Sweden), on the surface of a C18-modified gold sensor SPR chip (HPA, purchased from Biacore). All experiments were done at room temperature. The Biacore 3000 has four SPR flow cells in series, with the possibility of directing the flow through only a subgroup of the flow cells. This is utilized immediately before an actual experiment to precondition the Biacore flow system. We inject the actual solution used for the experiment through a single flow cell, before the flow is redirected into two other flow cells, from where we then collect the experimental data. This protocol was introduced in response to some inconsistent results, which were hypothesized to be unwanted effects from adsorption upstream of the SPR flow cell.

5.3 Adsorption of lipase on hydrophobic surfaces

The first set of results presented are for the adsorption of lipase in the absence of surfactant.

5.3.1 Presentation and discussion of data

The first set of experiments presented is an investigation of the adsorption dynamics of the two lipase variants introduced in section 5.2, in the absence of surfactants. The main purposes of these experiments were to get data on adsorption dynamics, upon which theoretical analysis could be based, and to qualitatively compare the two lipase variants under different conditions. The experiments were done under variation of injection flow rate and lipase concentration. The total volume of the injected solution was conserved at $150\,\mu$L across all the experiments. Data is presented for two different flow rates, namely $5\,\mu\text{Lmin}^{-1}$ and $10\,\mu\text{Lmin}^{-1}$, amounting to a total *contact time* of respectively $30\,\text{min} = 1800\,\text{s}$ and $15\,\text{min} = 900\,\text{s}$. The two flow rates correspond to Peclet numbers (see section 3.3.2) of respectively $\text{Pe} = 2500$ and $\text{Pe} = 5000$. The six different injection concentrations were chosen as $c_0 \in \{100, 150, 200, 300, 400, 500\}\,\text{nM}$. Two repetitions were done for a particular combination of parameters, and the mean value is presented along with error bars based on the standard deviation of the two repetitions. Error bars are only showed at a subset of the times of recorded data to achieve a more clear presentation. Fig. 5.2 presents timeseries of the adsorption process, i.e. the adsorbed amount Γ in $[\mu\text{gm}^{-2}]$ as a function of time. Fig. 5.3 presents the data in the phase plane spanned by the adsorbed amount Γ and its temporal rate of change $d\Gamma/dt$.

A universal behavior for all the data is that the adsorption rate, as well as the saturation level, increases with injection concentration c_0. The data is smooth and generally shows a monotone dependence of concentration and flow rate. In addition, the error bars are relatively small, indicating robust results at least within the experimental run of all the parameter combinations. The phase plane provides the clearest picture of the qualitative nature of the adsorption dynamics. The adsorption dynamics of the wild type lipase, at the low Peclet number $\text{Pe} = 2500$ (Fig. 5.3 (a)), is close to linear for all concentrations. As the flow rate is increased (Fig. 5.3 (b)) the adsorption rates are increased much more drastically than expected from both quasi-steady theory and simulations as presented in the preceding chapters. Quasi-steady theory predicts that the maximum adsorption rate scales with $\text{Pe}^{1/3}$ (see Eq. (3.44)), in the convection-diffusion-limited regime, which is where the largest effect of flow rate occurs. The much more pronounced effect of flow rate in the experimental data asks for other explanations than those provided in the theoretical and numerical section of this thesis. The wild type data at the high flow rate in Fig. 5.3 (b) also shows a more convex form, especially at high concentrations. This amounts to a prolonged adsorption to higher saturation levels than expected from a linear extrapolation of data at intermediate times. The phase plane dynamics of the mutant lipase in

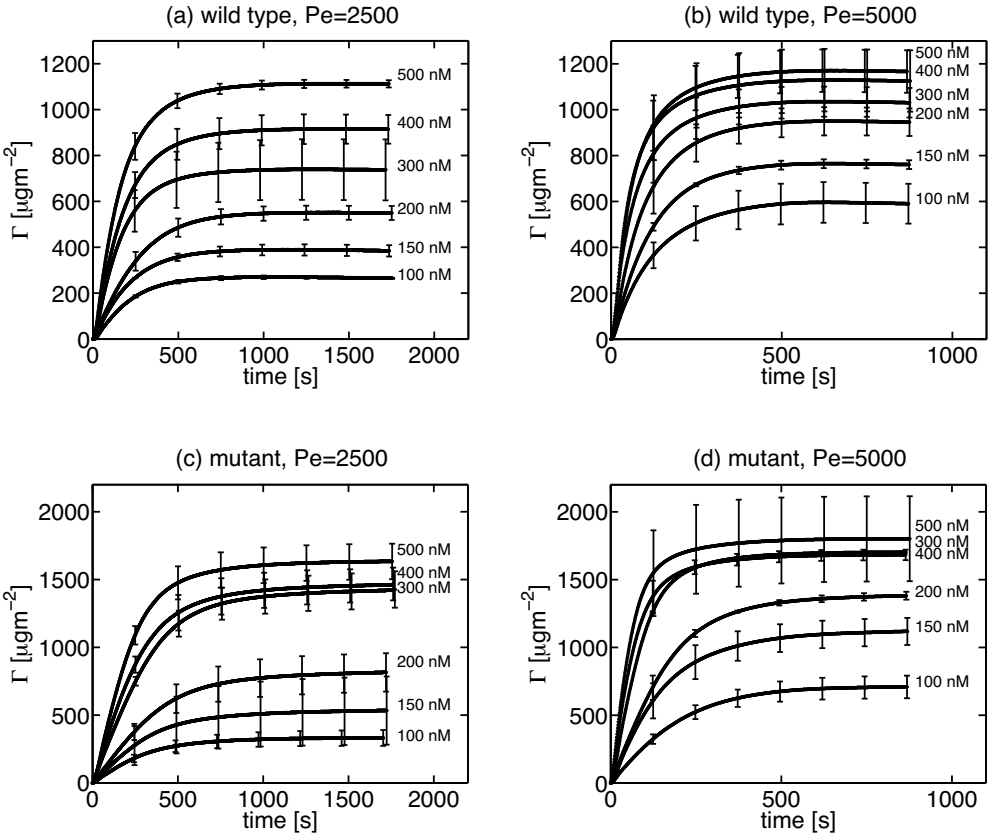

Figure 5.2: Timeseries obtained from SPR spectroscopy - wild type (a,b) and mutant (c,d) lipase for the flow rates $5\,\mu\mathrm{Lmin}^{-1}$ and $10\,\mu\mathrm{Lmin}^{-1}$.

Fig. 5.3 (c) and (d) has a more concave form for both flow rates. However, close to saturation a small convex tail is also observed for the mutant. The increase in adsorption rate going from low to high flow rate is equally pronounced for the mutant.

5.3.2 Inconsistency with expected behavior

Prior investigation of the lipase adsorption shows that the binding is irreversible, such that $k_\mathrm{d} = 0$. Therefore it is unexpected that the saturation levels depend on injection concentration. In other words, for irreversible adsorption the expectation is an adsorption process up to some saturation level, which is ideally independent of bulk concentration, as long as there are enough bulk particles

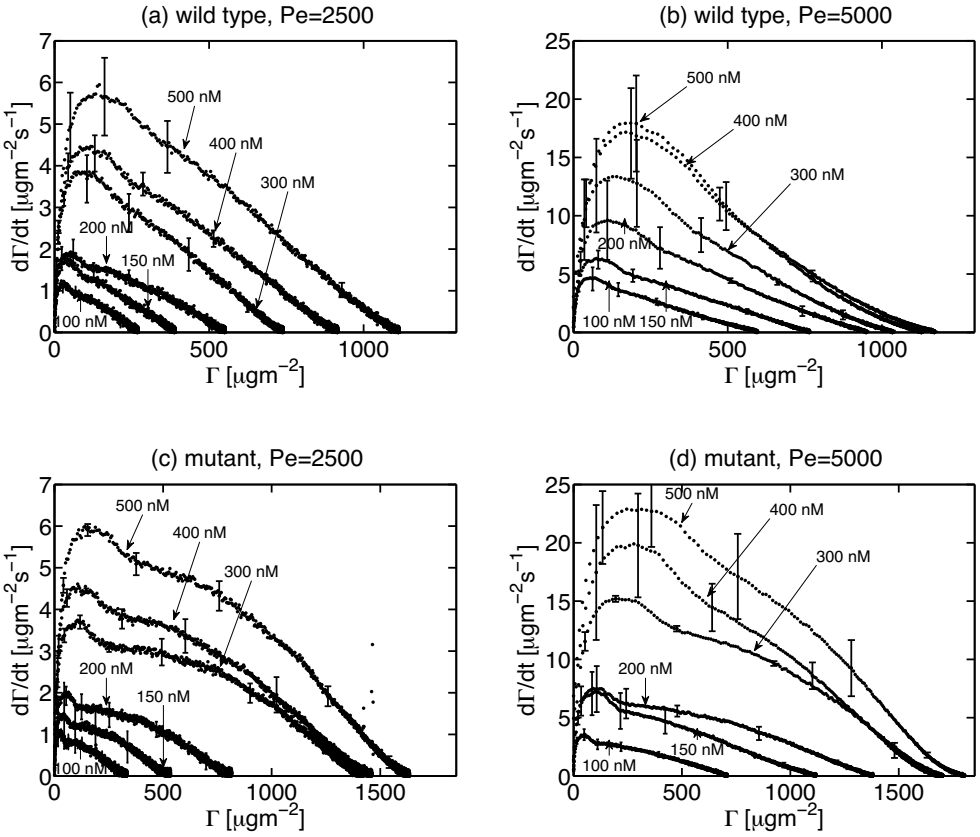

Figure 5.3: Phase plane representation of data from Fig. 5.2 - wild type (a,b) and mutant (c,d) lipase for the flow rates $5\,\mu$Lmin^{-1} and $10\,\mu$Lmin^{-1}.

available for adsorption. This suggests that the injection plug, in some way, runs out of lipase as time progresses in the adsorption experiment. This inconsistency was investigated further by running experiments with two consecutive injections of the mutant lipase. The concentration for the two consecutive injections was fixed at values $c_0 \in \{100, 200, 400\}$ nM, and the flow rate was varied between $25\,\mu$Lmin^{-1} and $100\,\mu$Lmin^{-1}. The results of these experiments are presented in Fig. 5.4. An increased adsorption is observed as the second injection is provided, which is more pronounced the lower the concentration gets. This suggests that the spatio-temporal profile of the injected concentration in the inlet of the flow cell, usually referred to as the injection plug, has a different nature than expected from the interface with the Biacore SPR apparatus.

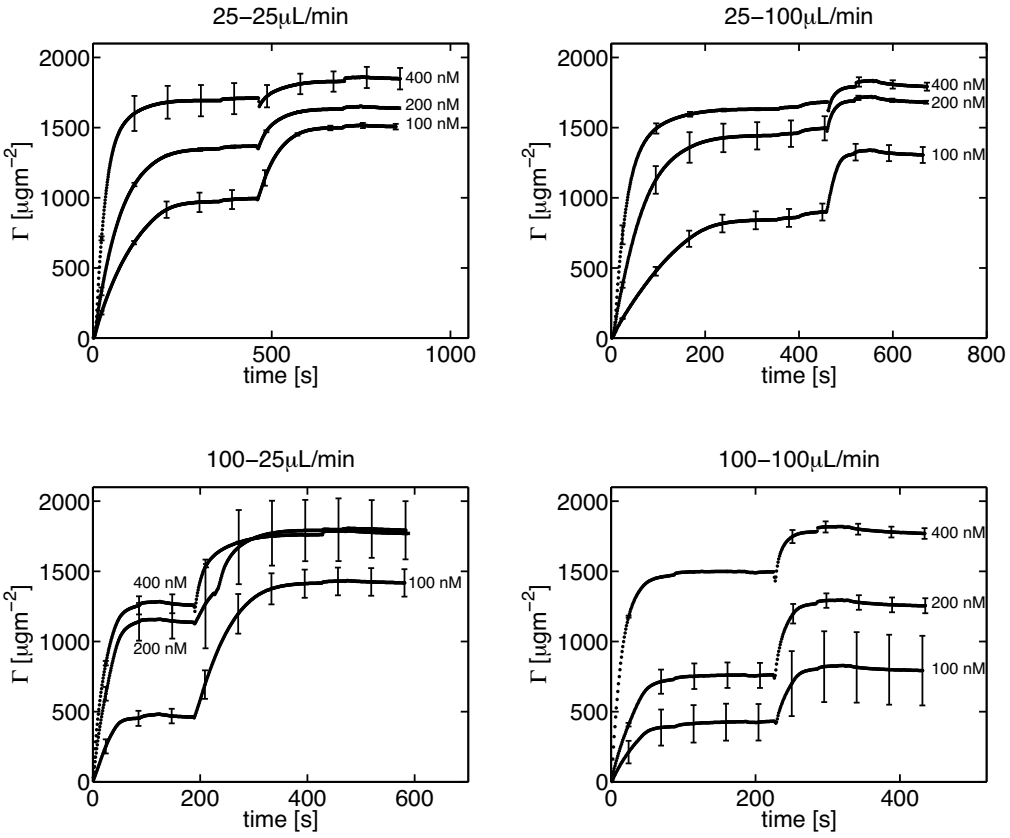

Figure 5.4: Two consecutive injections of lipase into the flow cell - The two flow rates used for the injections are indicated above each plot. The experiments were done for mutant lipase at fixed concentrations $c_0 \in \{100, 200, 400\}$ nM.

5.3.3 Head to head comparison of wild type and mutant lipase

In spite of the unexpected behavior described above, a qualitative comparison between the two lipase variants shows marked differences. Fig. 5.5 presents the data from Fig. 5.3, plotted together for the same flow rate. The wild type lipase shows very linear adsorption processes, especially for the slow flow rate (Pe = 2500). The mutant lipase has more nonlinear characteristics, overlapping the wild type data initially, but then turn into more concave curves, with both a higher adsorption rate and saturation level. From this behavior the mutant lipase is regarded as, loosely speaking, a stronger binder than the wild type lipase.

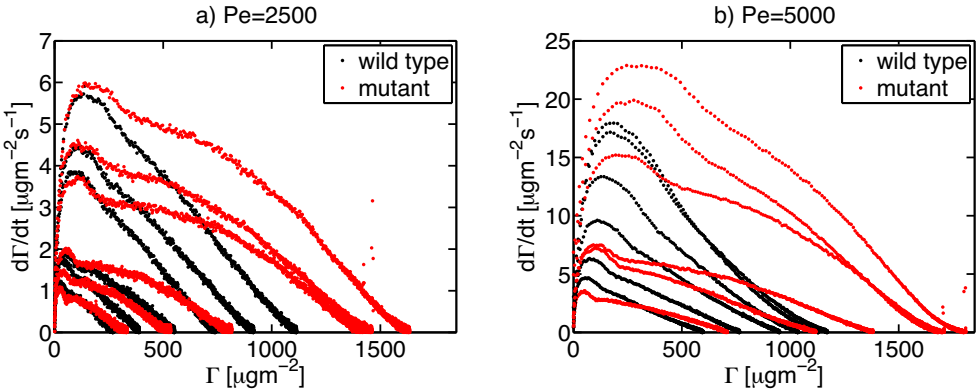

Figure 5.5: Head to head comparison of wild type and mutant lipase - Same data as in Fig. 5.2 and Fig. 5.3. (a) Flow rate: $5\,\mu$Lmin^{-1}. (b) Flow rate: $10\,\mu$Lmin^{-1}. The concentrations are $c_0 \in \{100, 150, 200, 300, 400, 500\}$ nM.

5.3.4 Lipase adsorption rate constants

A crude estimation of the adsorption rate constants for the lipase data are obtained from the initial data. The convection-diffusion limitation is initially neglected such that, according to Eq. (3.5), the initial SPR response is given by

$$\dot{\Gamma}(t=0)_{\text{model}} = k_{\text{a}} c_0 \gamma_{\text{m}} \tag{5.1}$$

This model predicts a finite initial adsorption rate, in contrast with the experiments. However, in the limit of kinetically limited dynamics, we know from the results in chapter 4, that the finite initial adsorption rate is close to the maximum adsorption rate in the experiment. Hence, setting $\dot{\Gamma}(t=0)_{\text{model}} = \max(\dot{\Gamma})_{\text{data}}$, and using the maximum SPR response for the surface capacity for lipase γ_{m}, we obtain

$$k_{\text{a}} = \frac{\max(\dot{\Gamma})_{\text{data}}}{c_0 \max(\Gamma)} \tag{5.2}$$

The adsorption rate constants for the wild type and mutant lipase, based on Eq. (5.2), are presented in Fig. 5.6 and table 5.1. Interestingly, the estimated adsorption rate constant are quite independent of the injection concentration. The estimated adsorption rate constants for the wild type are larger than for the mutant for both Peclet numbers. Also, the estimated adsorption rate constants increase substantially with Peclet number, which is of course undesirable. This behavior is consistent with the dramatic increase in adsorption rate under increase in flow rate mentioned above. Further theoretical analysis of the data, including

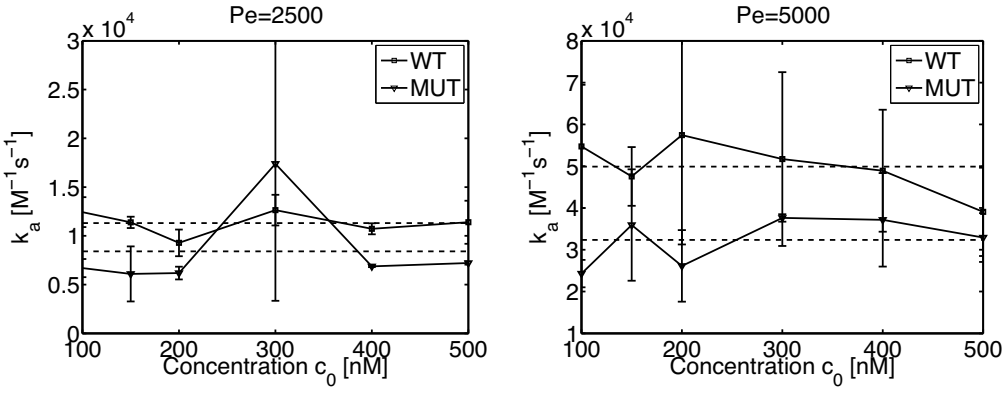

Figure 5.6: Lipase adsorption rate constants for the six concentrations - obtained from the initial data in Fig. 5.6 using Eq. (5.2)

Table 5.1: Lipase adsorption rate constants obtained from the initial data in Fig. 5.6 using Eq. (5.2), given as mean values and standard deviation across the six concentrations.

	Pe = 2500	Pe = 5000
$k_{\mathrm{a}}^{\mathrm{wt}} \times 10^{-4}\,[\mathrm{M}^{-1}s^{-1}]$	1.1 ± 0.1	4.9 ± 0.6
$k_{\mathrm{a}}^{\mathrm{mut}} \times 10^{-4}\,[\mathrm{M}^{-1}s^{-1}]$	0.7 ± 0.2	3.2 ± 0.6

mass transport modeling, is not pursued, due to the apparent shortcoming of information about the injection and operating conditions.

5.4 Competitive adsorption of lipase and surfactant

This section is concerned with competitive adsorption of lipase and surfactant. The study is in an early stage, and the scope of this section is merely to outline our approach to the subject.

5.4.1 Identification of competitive regime

The outcome of the competitive process of lipase and surfactant adsorption depends on the relative concentrations of the two interacting species. Loosely speaking, if one of the species is overly outnumbered by the other, it gets no foothold on the surface. The primary scope of the study is the competitive adsorption

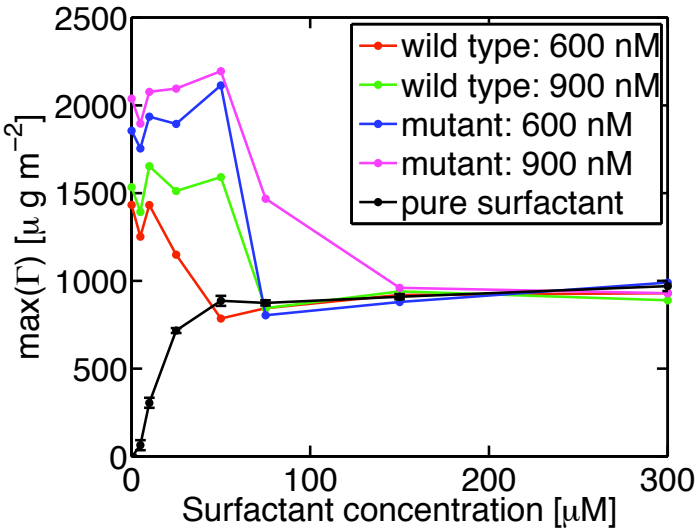

Figure 5.7: Maximum SPR response levels as a function of surfactant concentration - Consecutive values of the surfactant concentration $c_s = \{0, 5, 10, 25, 50, 75, 150, 300\}\,\mu$M. Lipase concentrations $c_l = \{600, 900\}$ nM. Flow rate set to $5\,\mu$Lmin^{-1} amounting to Pe = 2500.

dynamics in a relative concentration regime of equal competitiveness. In other words, the number of lipase and surfactant molecules is chosen such that a fair competition is observed. In order to identify a regime, where such dynamics is obtained, a sweep of surfactant concentration for a fixed lipase concentration is performed. From such experiments the maximum SPR response is deduced as a function of surfactant concentration. Fig. 5.7 presents such data for two concentrations of both the wild type and mutant lipase variant. First note for the pure surfactant system, that the maximum SPR response level initially increases as a function of concentration, whereafter it saturates at roughly $1000\,\mu$gm^{-2}. The qualitative form of the curve looks like a classical Langmuir isotherm. (The first order Langmuir adsorption model in Eq. (3.5) is later successfully applied for the pure surfactant system). At zero surfactant concentration we observe the maximum response levels for the pure lipase systems. The levels, which are roughly $1500\,\mu$gm^{-2} respectively $2000\,\mu$gm^{-2} for the wild type respectively mutant variant, are not strongly dependent on the lipase concentration, essentially meaning that the surface is nearly saturated. The larger SPR response for pure lipase saturation in comparison with pure surfactant saturation is the only way to distinguish between lipase and surfactant on the surface, since we have no way to label the two species. For increasing surfactant concentrations small fluctua-

tions in the maximum response are observed first. There is, however, a trend of a minor increase in the SPR response as a function of surfactant concentration, which suggests that surfactant and lipase are present on the surface together in some kind of optimal mixed state. This regime is followed by a steep decrease in the response towards the pure surfactant response. Importantly, this steep decrease is displaced towards higher surfactant concentrations for increasing lipase concentration, supporting that the desired competitive regime is determined. At high surfactant concentration, i.e. above $150\,\mu$M the surfactant system is totally dominant in the competitive process. The regime where the surfactant begins to dominate is closely related to the cmc of the surfactant, which for aqueous solution at ambient temperature is around $80\,\mu$M. This value, however, naturally depends on the solvent medium and the presence of other solutes. The data shows a rather smooth concentration dependency, i.e. no abrupt or singular behavior is observed. One could therefore conclude from the regime at around surfactant concentrations of $0-100\,\mu$M, that increasing the surfactant concentration simply leads to larger fraction of the surface it occupies in equilibrium. One must, however, keep in mind that the data in Fig. 5.7 are maximum response levels, and not equilibrium levels. As seen below the dynamical adsorption process shows first a quick increase, and then a slow decrease, in the SPR signal as a function of time, supporting that maximum response levels in Fig. 5.7 are not isotherms, and not a measure of equilibrium. As seen below the process is also greatly influenced by the flow rate, which was set to $5\,\mu\text{Lmin}^{-1}$ amounting to $\text{Pe} = 2500$ for the experiments in Fig. 5.7. This experiment primarily serves to identify some lipase and surfactant concentrations, at which we then put focus on the underlying dynamical adsorption process.

5.4.2 The competitive adsorption dynamics of lipase and surfactant

Based on the preliminary experimental results, presented above in Fig. 5.7, we move on to study the competitive adsorption dynamics of lipase and surfactant for both wild type and mutant lipase. The lipase concentration was chosen as $c_l = 800\,\text{nM}$, and the surfactant concentration was chosen as $c_s = 50\mu\text{M}$. The dynamical adsorption process was then obtained, using both wild type and mutant lipase. The adsorption experiments were run at two different flow rates, $5\,\mu\text{Lmin}^{-1}$ and $20\,\mu\text{Lmin}^{-1}$. The two flow rates amounts to $\text{Pe} = \{2500, 10000\}$. The total volume of solution injected in the association phase was $150\,\mu$L for both flow rates, which implies that the duration of the association phase was 30 min and 7.5 min, respectively. An association phase was directly followed by a dissociation phase of pure buffer injection to obtain ideal conditions for probing desorption

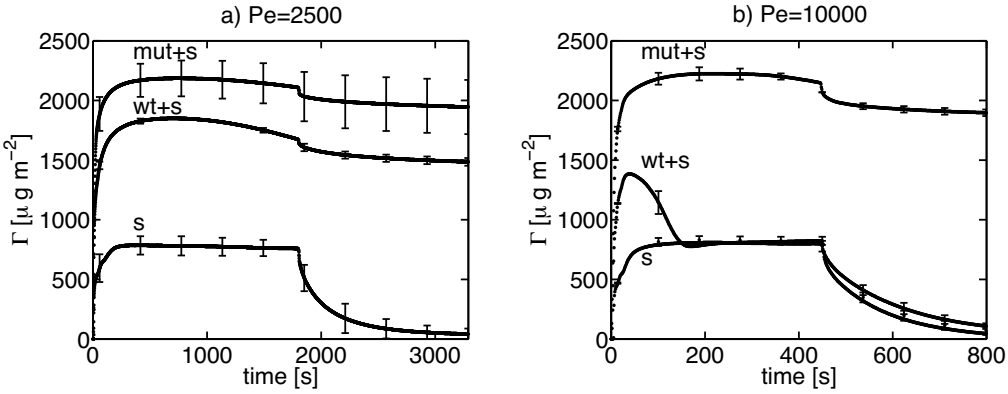

Figure 5.8: The competitive adsorption dynamics of lipase and surfactant - 150 μL of solution is injected at two different flow rates $\{5, 20\}\,\mu\text{Lmin}^{-1}$ (Pe = $\{2500, 10000\}$), followed by a dissociation phase of pure buffer injection. Meaning of labels: (mut+s) mutant lipase and surfactant mixture. (wt+s) wild type lipase and surfactant mixture. (s) pure surfactant, no lipase. Lipase concentration $c_l = 800\,\text{nM}$. Surfactant concentration $c_s = 50\mu\text{M}$.

from the surface. For use as reference the experiment was also done for the pure surfactant system, with no lipase in the solution. All experiments were repeated twice. The results are shown in Fig. 5.8 as mean values, with superimposed error bars, obtained from the standard deviation, of the two repetitions. Several points are immediately apparent from the data. The pure surfactant solution rapidly reaches equilibrium in the association phase and desorbs almost entirely within the experimental time in the dissociation phase. In this way the pure surfactant system qualitatively shows straightforward reversible adsorption/desorption behavior for both flow rates. For the mixed lipase/surfactant systems we generally observe a rapid initial increase in the SPR response up to a maximum value above the saturation value of the pure surfactant. Consistent with the data in Fig. 5.7 these maximum response levels are also higher than than those for the pure lipase solution. We therefore expect that the state of the surface at the maximum response is a mixture of the two species. This phase is followed by another phase where the SPR response decreases with time. Immediately after the transition to the dissociation phase we observed a rapid decrease in the SPR response. For $5\,\mu\text{Lmin}^{-1}$ the binding curves for the two lipases are qualitatively similar, with a higher SPR response for the mutant than for the wildtype lipase. Increasing the flow rate to $20\,\mu\text{Lmin}^{-1}$ causes no significant changes for the mutant lipase, but leads to a remarkably different binding process for the wildtype. Following the initial adsorption the response falls off rapidly to coincide with

the response for the pure surfactant solution. For all lipase/surfactant data, but the wild type at Pe = 10000, the decrease following the maximum response is relatively slow, and the following desorption in the dissociation phase is limited (partly irreversible). For the wild type lipase/surfactant system at Pe = 10000 the decrease in the signal, after the maximum response, is so rapid that the data essentially follows those for the pure surfactant system from an early time before the dissociation phase. In the dissociation phase we observe reversible desorption.

We do not know if a longer association phase would lead to data for the mixed systems, which would eventually coincide with the data for the pure surfactant system, for all the experiments. From the data shown in Fig. 5.8, we can only hypothesize about the potential progress of the dynamics if the dissociation phase was shifted to a later start. A head to head comparison of the two lipase variants shows that the mutant adsorbs to higher response levels. This is expected to be caused by a closer packing on the surface, stemming from a lesser degree of intermolecular repulsion between the lipases. Also, the mutant seems stronger in relation to the competition with surfactant, especially at the higher flow rate (Pe = 10000), where the wild type lipase gets almost no foothold in the competition whatsoever.

With the goal of getting a better comparison between the two different flow rates in Fig. 5.8, we plot the SPR response as a function of injected amount, instead of as a function of time. In this way, all the data can be combined into a single plot. The error bars are omitted, and the mean values are presented in Fig. 5.9. The general shape of the pure surfactant data, as well as the mutant/surfactant data, is conserved across change in flow rate. The wild type/surfactant data, however, clearly shows that the increase in flow rate drastically favors the surfactant above the lipase competitiveness. This suggests that the rate of arrival, which is increased by an increased flow rate, is critical in the competitive process. A direct hydrodynamic effect is not expected to be important, due to the very low flow rates close to the surface, and around particles with sizes in the order of nanometers. Fig. 5.9 also shows a small decrease in the initial SPR response, as a function of injected amount, when the flow rate is increased. This is a characteristic of a kinetically limited process, where a faster injection implies that more solution flows past the sensor surface, without getting adsorbed.

5.4.3 Surfactant dynamics from Langmuir adsorption model

As a first quantitative approach to the data, we fit the first order Langmuir model in Eq. 3.5 to the pure surfactant dynamics. In this way we initially neglect

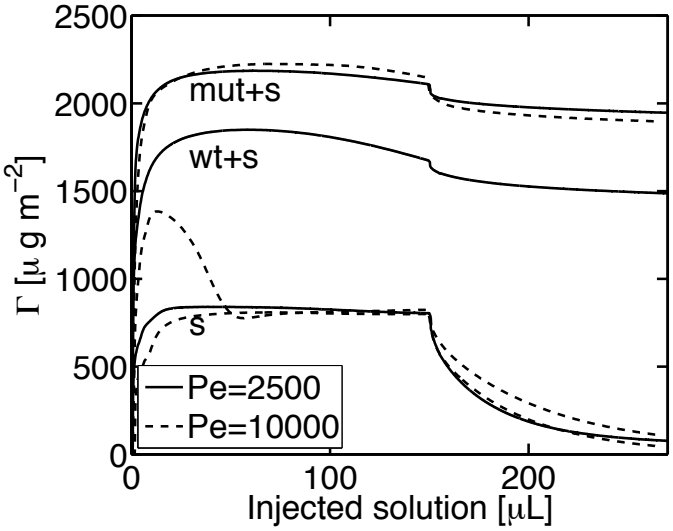

Figure 5.9: The data from Fig 5.8 combined into a single plot as a function of injected amount. - Association phase consisting of a 150 μL injection, followed by dissociation phase of pure buffer injection. Meaning of labels: (mut+s) mutant lipase and surfactant mixture. (wt+s) wild type lipase and surfactant mixture. (s) pure surfactant, no lipase. Lipase concentration $c_l = 800\,\text{nM}$. Surfactant concentration $c_s = 50\mu\text{M}$.

convection-diffusion limitation. The bulk concentration is set to $c_s = 50\mu\text{M}$. The results of nonlinear least squares fitting, for both $5\,\mu\text{Lmin}^{-1}$ and $20\,\mu\text{Lmin}^{-1}$, are presented in Fig. 5.10, and the obtained fitting parameters are presented in Table 5.2. The overall quality of both fits looks reasonably good. The obtained adsorption rate constant $k_{\text{a},s}$ slightly increases with Peclet number, but with a minor difference of about 6 percent. The desorption rate constant $k_{\text{d},s}$ increases more substantially with Peclet number, and since the saturation value is almost the same for the two Peclet numbers, the larger desorption rate constant is compensated for by a larger value of the maximum surface capacity $\gamma_{\text{m},s}$. Corresponding Damköhler and Biot numbers are also given in Table 5.2. The numerically low values support that the dynamics is in the regime of kinetic limitation, such that convection-diffusion limitation can be neglected, without imposing significant errors on the result.

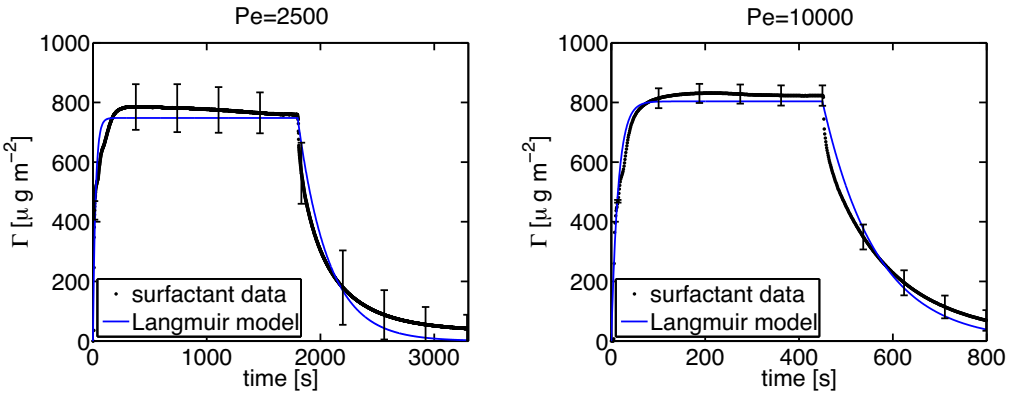

Figure 5.10: Fit of the Langmuir model (Eq. 3.5) to surfactant data - The obtained parameters are presented in table 5.2.

Table 5.2: Surfactant parameters obtained from the fit shown in Fig. 5.10.

	Pe = 2500	Pe = 10000
$k_{\mathrm{a},s}\,[\mathrm{M}^{-1}s^{-1}]$	772	823
$k_{\mathrm{d},s}\,[\mathrm{s}^{-1}]$	0.00386	0.00867
$\gamma_{\mathrm{m},s}\,[\mu g m^{-2}]$	821	980
Da	3.00×10^{-4}	2.40×10^{-4}
Bi	0.0023	0.0029

5.4.4 Lipase adsorption rate constants

A crude estimation of the adsorption rate constants for the lipase data can be done from the initial data. Again, the convection-diffusion limitation is initially neglected. According to Eqs. (3.24) and Eq. (3.4) this assumption implies an initial SPR response given by

$$\dot{\Gamma}(t=0)_{\mathrm{model}} = k_{\mathrm{a},e} c_e \gamma_{\mathrm{m},e} + k_{\mathrm{a},s} c_s \gamma_{\mathrm{m},s} \tag{5.3}$$

This model predicts a finite initial adsorption rate, in contrast with the experiments. However, in the limit of kinetically limited dynamics, we know from the results in chapter 4, that the finite initial adsorption rate is close to the maximum adsorption rate in the experiment. Hence, setting $\dot{\Gamma}(t=0)_{\mathrm{model}} = \max(\dot{\Gamma})_{\mathrm{data}}$, using the surfactant parameters from table 5.2, and estimating the maximum surface capacity for lipase $\gamma_{\mathrm{m},e}$ from the maximum SPR response, we put

$$k_{\mathrm{a},e} = \frac{\max(\dot{\Gamma})_{\mathrm{data}} - k_{\mathrm{a},s} c_s \gamma_{\mathrm{m},s}}{c_e \max(\Gamma)} \tag{5.4}$$

Table 5.3: Lipase adsorption rate constants obtained from the initial data in Fig. 5.8 using Eq. (5.4).

	Pe = 2500	Pe = 10000
$k_{\mathrm{a},l}^{\mathrm{wt}} \times 10^{-4}\,[\mathrm{M}^{-1}s^{-1}]$	10.2	9.3
$k_{\mathrm{a},l}^{\mathrm{mut}} \times 10^{-4}\,[\mathrm{M}^{-1}s^{-1}]$	8.2	13.2

Estimates for the adsorption rate constants for the wild type and mutant lipase, based on the competitive data in Fig. 5.8 and Eq. (5.4), are presented in table 5.3. The lipase adsorption rate constants in the presence of surfactants are about one order of magnitude larger than those obtained in the absence of surfactants in table 5.1. One hypothesis to explain this increase is that surfactant molecules screen lipase adsorption downstream of the SPR chip, which could lead to a higher actual lipase concentration available at the location of the SPR measurement.

5.4.5 Problems with reproducibility

The presented data on competitive adsorption of lipase and surfactants hints at some rich dynamics, as well as intriguing flow rate dependencies. However, following the measurements presented above, we encountered problems with reproducibility of the data. New data showed different, and less dramatic, behavior. The observations included a lesser degree of apparent displacement of lipase by surfactant, as well as a much less dramatic flow rate dependency. However, the response obtained for the pure surfactant system was substantially lower than for the data presented above, questioning the quality of the data. The collection of disconcerting results was continued until the Biacore SPR apparatus developed a failure so severe that the system shut down, and subsequent assistance from GE Healthcare (producers of Biacore) was required. This is the current status of the work, and further experimental investigations are therefore beyond the scope of the present dissertation. By the same token, further theoretical investigations, including an attempt of applying the bimolecular theory from section 3.4 to the data, needs stronger experimental support. Possible future work is discussed in chapter 6.

Chapter 6

Concluding remarks

6.1 Conclusions

The thesis brought different aspects of surface-based biosensors, and in particular SPR spectroscopy, into focus. Following a somewhat general review of SPR spectroscopy, including relevant applications, the theoretical framework for mass transport dynamics was developed in detail. Kinetic and diffusion scalings of time lead to nondimensional formulations that provide users of the surface-based biosensor technologies with a correct set of parameters to characterize the operating regime for their experiments. The widely adopted quasi-steady theory, which users of the technologies often employ in order to avoid cumbersome numerical solutions of the entire transport problem, was analyzed in detail. In this respect, the parameterization of the quasi-steady theory was related to the more comprehensive parameterization of the entire transport problem. The numerical results in the thesis yielded a way to correct experimentally obtained adsorption rate constants, based on fitting data with the quasi-steady theory. The problem of solute adsorption to all surfaces in the biosensor flow cell, besides the sensor surface, was briefly investigated numerically. Adsorption of a wild type and mutant lipase to a model hydrophobic surface, as well as competitive adsorption of lipase and surfactant, was investigated by a Biacore SPR reader. Qualitative comparison of the wild type and the mutant lipase showed higher saturation levels, and stronger competitiveness against surfactant, for the mutant. Adsorption and desorption rate constants for the studied species were estimated from the data. We emphasized some experimental conditions, which should be met in order for the experiments to form basis for rigorous theoretical modeling.

6.2 Future perspective

In this section some of the most natural future work is discussed. Surely, there are other possibilities, since the suggestions are naturally biased towards some of the issues which have had primary focus during the project. The section is divided into suggestions of a purely theoretical nature, then suggestions of a purely experimental nature, and finally, possible future work in the interface between theory and experiments.

6.2.1 Future theoretical work

- From a theoretical viewpoint a boundary layer theory, for which the quasi-steady theory is a first order approximation, is an interesting goal. Such a theoretical development could deepen the fundamental understanding of the quasi-steady theory, and furthermore suggest corrections to the model to better capture the convection-diffusion-limited regime. Such work could perhaps even be developed for other geometries encountered in other kinds of surface-based biosensors, as well as technological and natural systems more generally.

- Another issue, which could be analyzed in more detail than done in this thesis, is the effect of adsorption to surfaces besides the sensor surface. This work asks for a more thorough parameter study. A similar study for the bimolecular system, which encompass an even larger undiscovered parameter space, could be done. This study forms an interesting theoretical model basis for investigations of the possibility of screening unwanted adsorption of one specie by adsorption of another specie in the same solution.

- The theoretical framework developed for the bimolecular system can be used to determine parameter regimes where a two-component quasi-steady theory, and even just pure kinetic models, have sufficient accuracy for data fitting. This work could follow the progress of the manuscript [P1], but naturally involves a more extensive parameter investigation.

6.2.2 Future experimental work

- The previous suggestion of a model system for studying the possibility of screening unwanted adsorption is connected to a hypothesis on the experimental system. Namely, that the larger lipase adsorption rate constants, obtained for the experimental system including surfactant, can be explained by a larger bulk concentration of lipase due to screening of unwanted upstream adsorption of lipase by the surfactant. Support for this interpre-

tation could be searched for by experimental investigations using different relative concentrations of lipase and surfactants, and also different molecular species.

- More importantly, a major milestone is to obtain adsorption profiles for pure lipase solutions with concentration independent saturation. This goal should be theoretically possible for the concentrations used in this thesis, yet we observe steady-state at surface coverage levels below saturation. The experimental study with two consecutive injections of lipase suggest that the injection conditions are practically unknown. An experimental resolution of this issue should have top priority.

6.2.3 Future work in the interface between theory and experiments

- A more thorough link between theoretical models and experiments is a natural goal for the future. The simple first order model, as well as the suggested competitive model in section 3.4 can be applied to a more comprehensive set of data, and the competition parameters could be estimated. The competition parameters would then characterize a given system, and they could be used as quantifiers across different flow rates and relative concentrations. Concerning the competitive adsorption study outlined in the thesis, a theoretical model that takes into account the dynamics of micelle formation, and the adsorption/desorption dynamics of single surfactant molecules and micelles separately, could be a future goal. This would be an interesting model system for theoretical investigations, and brought to a higher impact level by combining it with supporting experiments.

References

Aguilar, M.I. and Small, D.H. (2005). Surface plasmon resonance for the analysis of beta-amyloid interactions and fibril formation in alzheimer's disease research. *Neurotox Res*, 7(1-2):17–27. 11

Alvarez, N.J., Walker, L.M. and Anna, S.L. (2010). Diffusion-limited adsorption to a spherical geometry: The impact of curvature and competitive time scales. *Phys. Rev. E*, 82:011604. 18

Anderluh, G., Macek, P. and Lakey, J.H. (2003). Peeking into a secret world of pore-forming toxins: membrane binding processes studied by surface plasmon resonance. *Toxicon*, 42(3):225–8. 11

Bakrac, B., Gutiérrez-Aguirre, I., Podlesek, Z., Sonnen, A.F.P., Gilbert, R.J.C., Macek, P., Lakey, J.H. and Anderluh, G. (2008). Molecular determinants of sphingomyelin specificity of a eukaryotic pore-forming toxin. *J Biol Chem*, 283(27):18665–77. 11

Batchelor, G.K. (1967). *An introduction to fluid dynamics*. U.P., Cambridge. 14

Besenicar, M., Macek, P., Lakey, J.H. and Anderluh, G. (2006). Surface plasmon resonance in protein-membrane interactions. *Chem Phys Lipids*, 141(1-2):169–78. 5, 9, 10, 11

Besenicar, M.P. and Anderluh, G. (2010). Preparation of lipid membrane surfaces for molecular interaction studies by surface plasmon resonance biosensors. *Methods Mol Biol*, 627:191–200. 11

Bird, R.B., Stewart, W.E. and Lightfoot, E.N. (2002). *Transport phenomena*. J. Wiley, New York, 2nd, wiley international ed edition. 33, 35, 36

Brody, J.P., Yager, P., Goldstein, R.E. and Austin, R.H. (1996). Biotechnology at low reynolds numbers. *Biophys J*, 71(6):3430–41. 14

Brzozowski, A.M., Savage, H., Verma, C.S., Turkenburg, J.P., Lawson, D.M., Svendsen, A. and Patkar, S. (2000). Structural origins of the interfacial activation in thermomyces (humicola) lanuginosa lipase. *Biochemistry*, 39(49):15071–82. 48

Bunjes, N., Schmidt, E., Jonczyk, A., Rippmann, F., Beyer, D., Ringsdorf, H., Gräber, P., Knoll, W. and Naumann, R. (1997). Thiopeptide-supported lipid layers on solid substrates. *Langmuir*, 13(23):6188–6194. 10

Cho, W., Bittova, L. and Stahelin, R.V. (2001). Membrane binding assays for peripheral proteins. *Anal Biochem*, 296(2):153–61. 11

Cooper, M.A., Hansson, A., Löfås, S. and Williams, D.H. (2000). A vesicle capture sensor chip for kinetic analysis of interactions with membrane-bound receptors. *Analytical Biochemistry*, 277(2):196–205. 10

Cooper, M.A., Try, A.C., Carroll, J., Ellar, D.J. and Williams, D.H. (1998). Surface plasmon resonance analysis at a supported lipid monolayer. *Biochim Biophys Acta*, 1373(1):101–11. 10

Cooper, M. (2004). Advances in membrane receptor screening and analysis. *J. Mol. Recognit.*, 17(4):286–315. 10, 11

Cooper, M.A. (2002). Optical biosensors in drug discovery. *Nat. Rev. Drug Disc.*, 1(7):515–28. 10

Cygler, M. and Schrag, J.D. (1997). Structure as basis for understanding interfacial properties of lipases. *Methods Enzymol*, 284:3–27. 48

Duinhoven, S., Poort, R., der Voet, G.V., Agterof, W., Norde, W. and Lyklema, J. (1995). Driving forces for enzyme adsorption at solid-liquid interfaces: 1. the serine protease savinase. *Journal of Colloid and Interface Science*, 170(2):340 – 350. 48

Fu, Z. and Santore, M.M. (1998). Kinetics of competitive adsorption of peo chains with different molecular weights. *Macromolecules*, 31(20):7014–7022. 24

Gennes, P.G.d., Brochard-Wyart, F. and Quéré, D. (2004). *Capillarity and wetting phenomena: drops, bubbles, pearls, waves*. Springer, New York. 48

Gervais, T. and Jensen, K.F. (2006). Mass transport and surface reactions in microfluidic systems. *Chemical Engineering Science*, 61(4):1102 – 1121. 16

Goldstein, B., Coombs, D., He, X., Pineda, A.R. and Wofsy, C. (1999 Sep-Oct). The influence of transport on the kinetics of binding to surface receptors: application to cells and biacore. *J Mol Recognit*, 12(5):293–299. 12

Goren, M., Galley, N. and Lennox, R.B. (2006 Jan 31). Adsorption of alkylthiol-capped gold nanoparticles onto alkylthiol self-assembled monolayers: an spr study. *Langmuir*, 22(3):1048–1054. 31, 37

Granéli, A., Edvardsson, M. and Höök, F. (2004). Dna-based formation of a supported, three-dimensional lipid vesicle matrix probed by qcm-d and spr. *ChemPhysChem*, 5(5):729–33. 10

Heyse, S., Ernst, O.P., Dienes, Z., Hofmann, K.P. and Vogel, H. (1998). Incorporation of rhodopsin in laterally structured supported membranes: observation of transducin activation with spatially and time-resolved surface plasmon resonance. *Biochemistry*, 37(2):507–22. 10, 11

Homola, J. (2008). Surface plasmon resonance sensors for detection of chemical and biological species. *Chem Rev*, 108(2):462–93. 5, 6

Jones, J.A., Rawles, R. and Hannun, Y.A. (2005). Identification of a novel phosphatidic acid binding domain in protein phosphatase-1. *Biochemistry*, 44(40):13235–45. 11

Kodoyianni, V. (2011). Label-free analysis of biomolecular interactions using spr imaging. *Biotech.*, 50(1):32–40. 9

Kuziemko, G.M., Stroh, M. and Stevens, R.C. (1996). Cholera toxin binding affinity and specificity for gangliosides determined by surface plasmon resonance. *Biochemistry*, 35(20):6375–84. 11

Lang, H., Duschl, C. and Vogel, H. (1994). A new class of thiolipids for the attachment of lipid bilayers on gold surfaces. *Langmuir*, 10(1):197–210. 10

Maldonado-Valderrama, J., Wilde, P., Macierzanka, A. and Mackie, A. (2011). The role of bile salts in digestion. *Adv Colloid Interface Sci*, 165(1):36–46. 48

Mason, T., Pineda, A.R., Wofsy, C. and Goldstein, B. (1999). Effective rate models for the analysis of transport-dependent biosensor data. *Math Biosci*, 159(2):123–44. 12

Mogensen, J.E., Sehgal, P. and Otzen, D.E. (2005). Activation, inhibition, and destabilization of thermomyces lanuginosus lipase by detergents. *Biochemistry*, 44(5):1719–30. 48

Mouritsen, O.G. (2005). *Life - as a matter of fat: the emerging science of lipidomics*. Springer, Berlin. 47

Mozsolits, H., Thomas, W. and Aguilar, M. (2003). Surface plasmon resonance spectroscopy in the study of membranemediated cell signalling. *J. Peptide Sci.*, 9(2):77–89. 11

Mozsolits, H. and Aguilar, M.I. (2002). Surface plasmon resonance spectroscopy: an emerging tool for the study of peptide-membrane interactions. *Biopolymers*, 66(1):3–18. 11

Myszka, D.G., He, X., Dembo, M., Morton, T.A. and Goldstein, B. (1998 Aug). Extending the range of rate constants available from biacore: interpreting mass transport-influenced binding data. *Biophys J*, 75(2):583–594. 11, 12, 31

Myszka, D.G., Morton, T.A., Doyle, M.L. and Chaiken, I.M. (1997 Feb 28). Kinetic analysis of a protein antigen-antibody interaction limited by mass transport on an optical biosensor. *Biophys Chem*, 64(1-3):127–137. 31

Noinville, S., Vidic, J. and Déjardin, P. (2010). Adsorption rate dependence on convection over a large length of a sensor to get adsorption constant and solute diffusion coefficient. *Colloids Surf B Biointerfaces*, 76(1):112–6. 12

Piliarik, M., Vaisocherová, H. and Homola, J. (2009). Surface plasmon resonance biosensing. *Methods Mol Biol*, 503:65–88. 6, 7, 8, 9

Pinholt, C., Fanø, M., Wiberg, C., Hostrup, S., Bukrinsky, J.T., Frokjaer, S., Norde, W. and Jorgensen, L. (2010). Influence of glycosylation on the adsorption of thermomyces lanuginosus lipase to hydrophobic and hydrophilic surfaces. *Eur J Pharm Sci*, 40(4):273–81. 48

Plant, A. (1993). Self-assembled phospholipid/alkanethiol biomimetic bilayers on gold. *Langmuir*, 9(11):2764–2767. 10

Plant, A., Brighamburke, M., Petrella, E. and Oshannessy, D. (1995). Phospholipid/alkanethiol bilayers for cell-surface receptor studies by surface plasmon resonance. *Analytical Biochemistry*, 226(2):342–348. 10

Raether, H. (1997). Surface plasmons on smooth and rough surfaces and on gratings. *Springer Tracts in Modern Physics (Springer, Berlin, 1988)*. 7

Reis, P., Holmberg, K., Watzke, H., Leser, M.E. and Miller, R. (2009). Lipases at interfaces: a review. *Adv Colloid Interface Sci*, 147-148:237–50. 48

Rich, R.L. and Myszka, D.G. (2007). Survey of the year 2006 commercial optical biosensor literature. *J Mol Recognit*, 20(5):300–66. 12

Rich, R.L. and Myszka, D.G. (2008). Survey of the year 2007 commercial optical biosensor literature. *J Mol Recognit*, 21(6):355–400. 12

Rich, R.L. and Myszka, D.G. (2010). Grading the commercial optical biosensor literature-class of 2008: 'the mighty binders'. *J Mol Recognit*, 23(1):1–64. 12

Robelek, R. (2009). Surface plasmon resonance sensors in cell biology: basics and application. *Bioanal Rev*, 1(1):57–72. 9

Saenko, E., Sarafanov, A., Ananyeva, N., Behre, E., Shima, M., Schwinn, H. and Josić, D. (2001). Comparison of the properties of phospholipid surfaces formed on hpa and l1 biosensor chips for the binding of the coagulation factor viii. *J Chromatogr A*, 921(1):49–56. 11

Salamon, Z., Brown, M. and Tollin, G. (1999). Plasmon resonance spectroscopy: probing molecular interactions within membranes. *Trends Biochem Sci*, 24:213–219. 11

Schmid, R.D. and Verger, R. (1998). Lipases: Interfacial enzymes with attractive applications. *Angewandte Chemie International Edition*, 37(12):1608–1633. 48

Schuck, P. (1996). Kinetics of ligand binding to receptor immobilized in a polymer matrix, as detected with an evanescent wave biosensor. i. a computer simulation of the influence of mass transport. *Biophys J*, 70(3):1230–49. 12

Schuck, P. and Minton, A.P. (1996). Analysis of mass transport-limited binding kinetics in evanescent wave biosensors. *Anal Biochem*, 240(2):262–72. 11, 12, 31

Sonesson, A.W., Blom, H., Hassler, K., Elofsson, U.M., Callisen, T.H., Widengren, J. and Brismar, H. (2008). Protein-surfactant interactions at hydrophobic interfaces studied with total internal reflection fluorescence correlation spectroscopy (tir-fcs). *J Colloid Interface Sci*, 317(2):449–57. 48

Sonesson, A.W., Elofsson, U.M., Brismar, H. and Callisen, T.H. (2006). Adsorption and mobility of a lipase at a hydrophobic surface in the presence of surfactants. *Langmuir*, 22(13):5810–7. 48

Squires, T.M., Messinger, R.J. and Manalis, S.R. (2008). Making it stick: convection, reaction and diffusion in surface-based biosensors. *Nat Biotechnol*, 26(4):417–26. 18

Stahelin, R.V. and Cho, W. (2001). Differential roles of ionic, aliphatic, and aromatic residues in membrane-protein interactions: a surface plasmon resonance study on phospholipases a2. *Biochemistry*, 40(15):4672–8. 11

Stenberg, E., Persson, B., Roos, H. and Urbaniczky, C. (1991). Quantitative determination of surface concentration of protein with surface plasmon resonance using radiolabeled proteins. *Journal of Colloid and Interface Science*, 143(2):513 – 526. 8

Stora, T., Lakey, J. and Vogel, H. (1999). Ion-channel gating in transmembrane receptor proteins: functional activity in tethered lipid membranes. *Angewandte Chemie-International Edition*, 38(3):389–391. 10, 11

Terrettaz, S., Stora, T., Duschl, C. and Vogel, H. (1993). Protein binding to supported lipid membranes: investigation of the cholera toxin-ganglioside interaction by simultaneous impedance spectroscopy and surface plasmon resonance. *Langmuir*, 9(5):1361–1369. 10

Wahlgren, M. and Arnebrant, T. (1991). Protein adsorption to solid surfaces. *Trends Biotechnol*, 9(6):201–8. 48

Wannerberger, K. and Arnebrant, T. (1996). Lipases from humicola lanuginosa adsorbed to hydrophobic surfaces–desorption and activity after addition of surfactants. *Colloids and Surfaces B: Biointerfaces*. 48

Wannerberger, K., Wahlgren, M. and Arnebrant, T. (1996). Adsorption from lipase-surfactant solutions onto methylated silica surfaces. *Colloids and Surfaces B: ...*. 48

Ward, L.D. and Winzor, D.J. (2000). Relative merits of optical biosensors based on flow-cell and cuvette designs. *Analytical Biochemistry*, 285(2):179–93. 8

Wilde, P.J. and Chu, B.S. (2011). Interfacial & colloidal aspects of lipid digestion. *Adv Colloid Interface Sci*, 165(1):14–22. 48

[P1]

Transient Convection, Diffusion, and Adsorption in Surface-based Biosensors

Rasmus Hansen,[*,†] Henrik Bruus,[‡] Thomas H. Callisen,[¶] and Ole Hassager[*,†]

Department of Chemical and Biochemical Engineering, Technical University of Denmark, Department of Micro- and Nanotechnology, Technical University of Denmark, and Novozymes A/S

E-mail: rasmush08@gmail.com; oh@kt.dtu.dk

Abstract

This paper presents a theoretical and computational investigation of convection, diffusion, and adsorption in surface-based biosensors. In particular, we study the transport dynamics in a model geometry of a Biacore surface plasmon resonance (SPR) sensor. The work, however, is equally relevant for other microfluidic surface-based biosensors, operating under flow conditions. A widely adopted approximate quasi-steady theory to capture convective and diffusive mass transport is reviewed, and an analytical solution is presented. An expression of the Damköhler number is derived in terms of the nondimensional adsorption coefficient (Biot number), the nondimensional flow rate (Péclet number), and the model geometry. Transient dynamics is investigated and we quantify the error of using the quasi-steady-state assumption for experimental data fitting in both kinetically limited and convection-diffusion-limited

[*]To whom correspondence should be addressed

[†]Department of Chemical and Biochemical Engineering, Technical University of Denmark, DTU Chemical Engineering Building 227, DK-2800 Kongens Lyngby, Denmark

[‡]Department of Micro- and Nanotechnology, Technical University of Denmark, DTU Nanotech Building 345 B, DK-2800 Kongens Lyngby, Denmark

[¶]Novozymes A/S, Novo Allé, 2880 - Bagsværd, Denmark

regimes. The results clarify the conditions under which the quasi-steady theory is reliable or not. In extension to the well known fact that the range of validity is altered under convection-diffusion-limited conditions, we show how also the ratio of the inlet concentration to the maximum surface capacity is critical for reliable use of the quasi-steady theory. Finally, our results provide users of surface-based biosensors with a tool of correcting experimentally obtained adsorption rate constants.

Introduction

Surface-based biosensors are increasingly used to investigate adsorption dynamics of molecular systems. Surface plasmon resonance (SPR) spectroscopy is a particular technique that is well established as a surface-based biosensor, allowing label-free, real time monitoring of adsorption of biological macromolecules, such as proteins. For a detailed description of the principles behind SPR spectroscopy see Stenberg et al.,[1] and for more recent reviews of SPR sensors see Homola et al.[2] and Homola.[3]

While the SPR technique, developed and commercialized by e.g. Biacore, is well capable of capturing qualitative behavior, quantitative studies of chemical rate constants and equilibrium constants are more challenging. Inconsistencies in derived rate constants has lead to both experimental and theoretical investigations of the effect of convection and diffusion on the SPR signal.[4,5] Significant progress was made by the application of a quasi-steady-state approximation, i.e. a steady-state bulk mass transport coupled to a dynamic adsorption scheme (explained in details below). This approximation has been widely adopted for Biacore data analysis.[5–10] However, practice in the biochemical society still, to a large degree, consists of empirical and qualitative studies.[11–14]

The quasi-steady-state approximation leads to a nondimensional number called the Damköhler number, which is sometimes referred to as the limit coefficient. An expression of the Damköhler number is derived in terms of the nondimensional adsorption coefficient (Biot number), the nondi-

mensional flow rate (Péclet number), and the model geometry. The ability of the quasi-steady theory to capture mass transport is thoroughly tested, by comparison with numerical simulations of the transient dynamics. In this way the consequences of using the quasi-steady theory for experimental data fitting in both kinetically limited and convection-diffusion limited regimes are properly quantified.

Theory

This section provides a theoretical treatment of mass transport, i.e. convection, diffusion, and adsorption, in a microfluidic device with a surface-based biosensor. We consider only unimolecular systems, i.e. a single solute in solution. First, the system geometry is presented, along with the evolution equations governing the system dynamics. We present results of using two different time scales, namely a kinetic time and a diffusion time, the former proving useful if adsorption kinetics is slow compared to bulk mass transport to the surface, and the latter proving useful in the opposite case. The nondimensional parameters are discussed, and estimates of numerical values are provided. The section ends with a thorough description and analysis of the quasi-steady theory, including a discussion of its inherent parameter - the Damköhler number. The analysis contains an analytical solution of the quasi-steady theory.

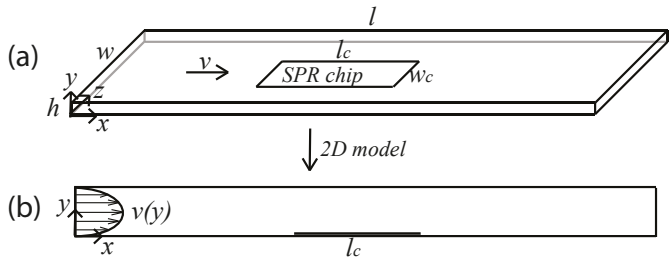

Figure 1: (a) Rectangular flow cell of length l, height h, and width w. The SPR chip of length l_c, and width w_c, is indicated as the square in the middle of the flow cell. The buffer flow is represented by the velocity vector v. (b) The two-dimensional approximation of the system in the vertical xy-plane. The parabolic velocity profile is indicated at the inlet of the flow cell.

System geometry & 2D Approximation

We investigate transport dynamics in a model geometry of a Biacore surface plasmon resonance (SPR) sensor, which by far is the most common SPR platform used.[15] The finite distance from the inlet of the microfluidic flow cell to the sensor surface is included, as shown in Figure 1. The length scales are $l = 2.3\,\mathrm{mm}$, $w = 0.5\,\mathrm{mm}$, and $h = 0.05\,\mathrm{mm}$. Adsorption is probed by the SPR chip located on the surface in the middle of the flow cell. The SPR chip has a length of $l_\mathrm{c} = 0.6\,\mathrm{mm}$, and a width of $w_\mathrm{c} = 0.16\,\mathrm{mm}$. The fluid flows in the lengthwise direction (x), with a parabolic velocity profile along the direction (y) of the height of the flow cell, i.e. $v_x(y) = 4v_m(y/h)(1-y/h)$, where v_m is the maximum velocity. Based on the large geometric aspect ratio $w/h = 10$, and the small Reynolds numbers often present in the system, we have assumed total invariance in the direction (z) of the width of the flow cell,[16] essentially ending up with a two-dimensional consideration of the transport. Hereby we do not take boundary effects from the side walls of the flow cell at $z = \{0, w\}$ into account.

Evolution equations

We define two dependent variables, namely the bulk concentration field $c = c(x,y,t)$, and the surface concentration field $\gamma = \gamma(x,t)$, where t is time. We name the bulk domain Ω, and the surface domains $\{\partial\Omega, \partial\Omega_\mathrm{ads}\}$, referring to insulating, non-adsorbing surfaces, respectively surfaces where adsorption takes place. The spatio-temporal evolution of the bulk concentration field $c = c(x,y,t)$ is governed by the convection-diffusion equation

$$\frac{\partial c}{\partial t} + v_x(y)\frac{\partial c}{\partial x} = D\nabla^2 c, \qquad (x,y) \in \Omega, \tag{1}$$

where the Laplacian $\nabla^2 = \partial^2/\partial x^2 + \partial^2/\partial y^2$, and D is the diffusion coefficient. The boundary conditions for the bulk concentration are given by

$$\frac{\partial c}{\partial y} = 0, \qquad y \in \partial\Omega, \tag{2}$$

$$-D\frac{\partial c}{\partial y} = -\mathscr{A}(\gamma, c), \qquad y \in \partial\Omega_{\text{ads}}. \tag{3}$$

The former is simply a no-flux condition, whereas the latter is a balance between diffusive flux perpendicular to the surface and net adsorption rate, captured in the adsorption term $\mathscr{A}(\gamma, c)$ in Eq. (5). At the inlet of the flow cell, at $x = 0$, the concentration is equal to the injection concentration, $c = c_0$. At the outlet of the flow cell, $x = l$, we assume free convection, i.e. essentially $\partial c/\partial x = 0$. The spatio-temporal evolution of the surface concentration field $\gamma = \gamma(x,t)$ is governed by the adsorption-diffusion equation

$$\frac{\partial \gamma}{\partial t} - \frac{\partial}{\partial x}\left[D_s \frac{\partial \gamma}{\partial x}\right] = \mathscr{A}(\gamma, c), \qquad \partial\Omega_{\text{ads}}, \tag{4}$$

where D_s is the surface diffusion coefficient, which in general can be a function of both the independent variables, x and t, as well as the dependent variables γ and c. The adsorption term $\mathscr{A}(\gamma, c)$ represents the net rate of change of surface concentration due to adsorption and desorption. A particular functionality of $\mathscr{A}(\gamma, c)$ is determined by the kinetics of some chosen adsorption-desorption scheme, and can in general include arbitrarily complex surface kinetics. No-flux boundary conditions for γ, i.e. $\partial\gamma/\partial x = 0$, are imposed at the end of the adsorbing domain, i.e. surface bound molecules only leave the chip by desorption.

Adsorption kinetics

The adsorption kinetics is modeled by a phenomenological model, which ultimately captures experimental data and thereby provide reasonable and consistent phenomenological parameters. The standard adsorption model that still contains the feature of a maximum surface capacity γ_{m} is the Langmuir adsorption model. This model is essentially a first order scheme between bulk molecules at the interface $c|_{y=0}$ and free surface sites $(\gamma_{\text{m}} - \gamma)$, with adsorption rate constant k_{a} and desorption rate constant k_{d}. This first order model may be written in the form

$$\mathscr{A}(\gamma, c) = k_{\text{a}} c|_{y=0}(\gamma_{\text{m}} - \gamma) - k_{\text{d}}\gamma. \tag{5}$$

When $c|_{y=0}$ is independent of γ this is a linear relation between $\mathscr{A}(\gamma,c)$ and γ. This particular adsorption model is a *local theory* in both space and time, i.e. the evolution of γ at (x,t) depends only on the present state at (x,t). The ultimate goal is often to obtain consistent values for the triplet $(k_\mathrm{a}, k_\mathrm{d}, \gamma_\mathrm{m})$ of phenomenological parameters from experimental biosensor data. In this linear model the adsorption and desorption rate constants, k_a and k_d respectively, are assumed unaltered by the density on the surface. In reality, one might expect interactions between adsorbed particles at high densities. However, in spite of its simplicity, it has been argued that this model is general enough to explain the majority of adsorption/desorption processes in molecular biology.[17] Substituting Eq. (5) into Eq. (4) and Eq. (3), these two equations together with Eq. (1), and the remaining boundary conditions, form a nonlinear system of partial differential equations for the two concentration fields $c = c(x,y,t)$ and $\gamma = \gamma(x,t)$. The system is of such complexity that a numerical study is necessary for detailed analysis.

Nondimensional parameterization

Nondimensional formulations are developed for a more comprehensible parameterization of the evolution equations. Two different nondimensional formulations are introduced and discussed.

Nondimensional parameterization: kinetic scaling

In order to put the evolution equations on nondimensional form, we introduce the following spatial and temporal scales:

$$\bar{x} = \frac{x}{h}, \quad \bar{y} = \frac{y}{h}, \quad \bar{t} = k_\mathrm{a} c_0 t. \tag{6}$$

Note in particular that time has been made nondimensional by the adsorption rate. For the dependent concentration variables we introduce the following scaled dependent variables:

$$\bar{c} = \frac{c}{c_0}, \quad \bar{\gamma} = \frac{\gamma}{\gamma_\mathrm{m}}. \tag{7}$$

In terms of these nondimensional variables, and the definitions $f(\bar{y}) = 4\bar{y}(1-\bar{y})$, $\overline{\nabla}^2 = \partial^2/\partial\bar{x}^2 + \partial^2/\partial\bar{y}^2$ we obtain the nondimensional evolution equation for the bulk concentration field

$$\mathrm{Bi}\bar{c}_0\frac{\partial\bar{c}}{\partial\bar{t}} + \mathrm{Pe}f(\bar{y})\left(\frac{\partial\bar{c}}{\partial\bar{x}}\right) = \overline{\nabla}^2\bar{c}, \qquad \Omega, \tag{8}$$

with the boundary condition (Eq. (3)) given by

$$\left.\frac{\partial\bar{c}}{\partial\bar{y}}\right|_{\bar{y}=0} = \mathrm{Bi}\bar{c}|_{\bar{y}=0}(1-\bar{\gamma}) - K\mathrm{Bi}\gamma, \qquad \partial\Omega_{\mathrm{ads}}. \tag{9}$$

The nondimensional evolution equation for the surface concentration field is given by

$$\frac{\partial\bar{\gamma}}{\partial\bar{t}} - \frac{\partial}{\partial\bar{x}}\frac{d_s}{\mathrm{Bi}\bar{c}_0}\frac{\partial\bar{\gamma}}{\partial\bar{x}} = \bar{c}|_{\bar{y}=0}(1-\bar{\gamma}) - K\gamma, \qquad \partial\Omega_{\mathrm{ads}}. \tag{10}$$

The remaining boundary conditions are trivially translated into the nondimensional form. These nondimensional evolution equations are parameterized by the following five nondimensional groups.

$$\mathrm{Pe} = v_m h/D, \tag{11}$$

$$\mathrm{Bi} = k_{\mathrm{a}}\gamma_{\mathrm{m}}h/D, \tag{12}$$

$$\bar{c}_0 = c_0 h/\gamma_{\mathrm{m}}, \tag{13}$$

$$K = k_{\mathrm{d}}/k_{\mathrm{a}}c_0, \tag{14}$$

$$d_s = D_s/D. \tag{15}$$

The Péclet number Pe measures the ratio of transport by convection to perpendicular diffusion, and is essentially the nondimensional flow rate. The Biot number Bi measures the ratio of adsorption rate to diffusion along the height of the flow cell, and is essentially the nondimensional adsorption rate constant. $\bar{c}_0$ is a nondimensional inlet concentration. In the limit of no flow, $\bar{c}_0$ is the reciprocal of the fraction of the height h needed to fill the surface up to $\gamma = \gamma_{\mathrm{m}}$. This interpretation explains the close relationship between $\bar{c}_0$ and the so called depletion depth introduced by.[18] K is the kinetic

equilibrium constant. d_s is the ratio of the surface and bulk diffusion coefficients, and if $D_s < D$, $d_s \in \{0,1\}$ measures the hindrance of diffusion caused by the presence of the surface. Interestingly, the magnitude of the transient term in Eq. (8) is weighed by the product $\overline{c}_0 \mathrm{Bi} = k_\mathrm{a} c_0 h^2/D$, meaning essentially that adsorption dynamics for large inlet concentrations of molecules with a high affinity to the surface evolves in a transient regime. This result is supported by Squires et al.[19] in their Eq. (21).

Nondimensional parameterization: diffusion scaling

Following a similar approach as above, but with the difference of scaling time with a diffusion time, i.e. $\bar{t} = Dt/h^2$, the nondimensional evolution equation for the bulk concentration field takes the form

$$\frac{\partial \overline{c}}{\partial \overline{t}} + \mathrm{Pe} f(\overline{y}) \left(\frac{\partial \overline{c}}{\partial \overline{x}} \right) = \overline{\nabla}^2 \overline{c}, \qquad \Omega \tag{16}$$

while the boundary condition (Eq. (3)) is now given by

$$\left. \frac{\partial \overline{c}}{\partial \overline{y}} \right|_{\overline{y}=0} = \mathrm{Bi} \overline{c}|_{\overline{y}=0} (1-\overline{\gamma}) - K \mathrm{Bi} \overline{\gamma}, \qquad \partial\Omega_\mathrm{ads} \tag{17}$$

The nondimensional evolution equation for the surface concentration field becomes

$$\frac{\partial \overline{\gamma}}{\partial \overline{t}} - \frac{\partial}{\partial \overline{x}} d_s \frac{\partial \overline{\gamma}}{\partial \overline{x}} = \mathrm{Bi} \overline{c}_0 \overline{c}|_{\overline{y}=0} (1-\overline{\gamma}) - K \mathrm{Bi} \overline{c}_0 \overline{\gamma}, \qquad \partial\Omega_\mathrm{ads} \tag{18}$$

The correspondence between the time scales for kinetic scaling (ks) and diffusion scaling (ds) are

$$\bar{t}^\mathrm{ks} = \bar{t}^\mathrm{ds} k_\mathrm{a} c_0 h^2/D = \mathrm{Bi} \overline{c}_0 \bar{t}^\mathrm{ds}. \tag{19}$$

Kinetic scaling or diffusion scaling?

The kinetic scaling of time leads to a nondimensional formulation which is particularly advantageous in the regime of kinetically limited dynamics. Generally speaking, kinetically limited

dynamics is obtained for small Bi numbers (Bi $\ll 1$) and/or large Péclet numbers (Pe $\gg 1$). Kinetically limited dynamics is, opposed to convection-diffusion limited dynamics, characterized by an independence of the flow rate, i.e. Péclet number, and a scaling of the dynamics with the Biot number. This dynamical behavior is referred to as a kinetic scaling, which is therefore also the terminology used for this particular nondimensional formulation. If, on the other hand, the adsorbing molecules have a very high affinity to the surface, Bi $\gg 1$. In this limit the dynamics is convection-diffusion limited, which is characterized by an independence of adsorption rate, i.e. Biot number, and a scaling of the dynamics with the Péclet number. In this limit it is advantageous to use the diffusion scaling of time.

Disregarding the dynamical limit of the system, there are other pros and cons for applying the two different time scales. As seen below, the quasi-steady theory adopts a minimal number of nondimensional parameters by using kinetic scaling. Hence kinetic scaling is advantageous when working with the quasi-steady theory. This is consistent with the fact that the quasi-steady-state approximation is only theoretically supported for kinetically limited dynamics. This is further elaborated on in the latter section on the quasi-steady theory. However, concerning practical use of the theory for experimental data fitting, we remark that k_a is usually a parameter one wish to determine from an adsorption experiment, and thereby unknown *a priori*. Hence, kinetic scaling is not practical for experimental data fitting - an issue avoided by using diffusion scaling. Dependent on the experimental regime it might as well be preferable to present and fit experimental data unscaled.

Estimates of nondimensional numbers

In this section we estimate some reasonable values for the nondimensional numbers. Concerning typical operating conditions, flow rates are in the range $Q = 1 - 100\,\mu\mathrm{Lmin}^{-1}$, which amounts to maximum velocities of $v_m = 3Q/2hw = 10^{-3} - 10^{-1}\,\mathrm{ms}^{-1}$. Injection concentrations typically range from $c_0 = 10^{-1} - 10^{2}\,\mu\mathrm{M}$. To proceed we need to consider a model binder. We take as an

example a globular protein with a diameter of $2R = 5\,\mathrm{nm}$, and molecular weight $M_w = 30\,\mathrm{kDa} = 3 \times 10^4\,\mathrm{gmol}^{-1}$. A simple estimate of the maximum surface capacity γ_m is simply the weight of one molecule divided by its diameter squared. Viz, $\gamma_\mathrm{m} = M_w/4N_\mathrm{A}R^2 \approx 2 \times 10^3\,\mu\mathrm{gm}^{-2}$, where N_A is the Avogadro number. However, in biochemical studies the surface of the chip, or the dextran layer, is sometimes prepared with a relatively low number of binding sites, with the aim of reducing rebinding probability and neighbor interactions among the adsorbing binders. This implies that the above estimate for γ_m, which is based on a packing occurring for e.g. self-assembled monolayers, represents an upper limit. In several applications the maximum surface capacity can be significantly lower. The diffusion coefficient can be estimated from the Stokes-Einstein relation. In aqueous solution at room temperature, the dynamic viscosity is $\mu \approx 10^{-3}\,\mathrm{Nsm}^{-2}$, and $T \approx 300\,\mathrm{K}$, hence $D = k_\mathrm{B}T/6\pi\mu R \approx 10^{-10}\,\mathrm{m}^2\mathrm{s}^{-1}$.

Based on the above values we can estimate the regime of the nondimensional numbers. By choosing $c_0 \approx 1\,\mu\mathrm{M}$, we obtain $\bar{c}_0 = c_o h/\gamma_\mathrm{m} \approx 1$, in the case of close packing on the surface. For surfaces prepared with a lower number of binding sites $\bar{c}_0 > 1$. For the Péclet number we obtain $\mathrm{Pe} = v_m h/D \approx 5 \times 10^2 - 5 \times 10^4$.

The quasi-steady theory

Ideally one would like to interpret SPR data by assuming simply that the concentration near the sensor $c_{y=0}$ is identical to the injection concentration c_0, that is by assuming that there is no resistance to mass transfer. To account for the corrections due to some mass transfer resistance, it has been suggested to interpret data by means of a mass transport model, saying that the overall flux of solute J to the surface is proportional to the difference between the far field concentration c_0, usually taken as the injection concentration, and the concentration close to the surface of the sensor $c|_{y=0}$, i.e. $J = k_\mathrm{L}(c_0 - c|_{y=0})$. In fact, this is based on a solution to the stationary diffusion-

convection equation for the concentration field $c = c(x,y)$ on a semi-infinite domain $x, y \geq 0$.

$$v_x \frac{\partial c}{\partial x} = D \frac{\partial^2 c}{\partial y^2}, \quad y > 0. \tag{20}$$

The velocity $v_x = v_x(y)$ is linearized close to the surface, i.e. $v_x(y) = \dot{\gamma}_w y$, $\dot{\gamma}_w$ being the shear rate at the surface, and the boundary conditions for the concentration field are $c(x,y)|_{y=0} = const$, $c(x,y)|_{x,y\to\infty} = 0$, and $c(x,y)|_{x=0} = c_0$. The solution consists of a concentration boundary layer close to the surface $y = 0$, and a flux of solute to the surface $J = k_L(c_0 - c|_{y=0})$, where the mass transport parameter k_L is given by

$$k_L = \frac{2D}{\Gamma(\frac{7}{3})} \left(\frac{\dot{\gamma}_w}{9Dl} \right)^{1/3} \tag{21}$$

This mass transport parameter is often chosen as a free fitting parameter, although it may in fact be predicted from the operating conditions. Given a flow rate Q the shear rate at the wall is

$$\dot{\gamma}_w = \frac{6Q}{h^2 w} \tag{22}$$

The coupling of this stationary convection-diffusion solution with the adsorption kinetics on the surface is performed by loosening up the Dirichlet boundary condition $c(x,y)|_{y=0} = const$. Letting these bulk particles $c|_{y=0}$ adsorb, they are converted into surface particles γ, and a simple mass balance on the surface dictates $J = d\gamma/dt = \mathscr{A}(\gamma, c)$. The critical assumption here is that the adsorption is so slow, that the bulk concentration on the surface $c|_{y=0}$ is practically constant, and use of the steady-state flux $J = k_L(c_0 - c|_{y=0})$, with k_L given by Eq. (21), is still reasonable.
Inserting the steady-state flux into the mass balance on the surface we obtain $k_L(c_0 - c|_{y=0}) = \mathscr{A}(\gamma, c)$. In the case of linear kinetics (Eq. (5)) this becomes an algebraic equation for $c|_{y=0}$, with the solution

$$c|_{y=0} = \frac{k_L c_0 + k_d \gamma}{k_a(\gamma_m - \gamma) + k_L}. \tag{23}$$

Substituting this into Eq. (5) gives the following nonlinear ordinary differential equation for the evolution of the surface concentration $\gamma = \gamma(t)$

$$\frac{d\gamma}{dt} = \frac{k_a k_L c_0(\gamma_m - \gamma) - k_d k_L \gamma}{k_a(\gamma_m - \gamma) + k_L}. \tag{24}$$

Using kinetic scaling, we can write Eq. (24) as

$$\frac{d\overline{\gamma}^{ks}}{d\overline{t}} = \frac{1-(1+K)\overline{\gamma}}{1+\mathrm{Da}(1-\overline{\gamma})}, \tag{25}$$

with the additional introduction of the important nondimensional Damköhler number

$$\mathrm{Da} = k_a \gamma_m / k_L, \tag{26}$$

which is the ratio of the adsorption rate and the rate of mass transport to the surface. The Damköhler number measures the limiting effect of convection-diffusion on the adsorption process. If $\mathrm{Da} \ll 1$ the system is kinetically limited, and if $\mathrm{Da} \gg 1$ the system is diffusion limited. Note in particular when $\mathrm{Da} \ll 1$ Eq. (25) becomes

$$\frac{d\overline{\gamma}^{ks}}{d\overline{t}} = 1-(1+K)\overline{\gamma}, \qquad \mathrm{Da} \ll 1, \tag{27}$$

which is simply the nondimensional form of Eq. (5), i.e. a purely adsorption-limited, linear, kinetic process. Also, the initial rate of adsorption, starting from the initial condition of zero surface concentration, $\overline{\gamma} = 0$, is predicted to be

$$\frac{d\overline{\gamma}}{d\overline{t}}(0)^{ks} = \frac{1}{1+\mathrm{Da}} \quad \text{or} \quad \frac{d\gamma}{dt}(0)^{ks} = c_0 k_L \frac{\mathrm{Da}}{1+\mathrm{Da}}. \tag{28}$$

Using diffusion scaling the formulation of the quasi-steady theory involves the two additional parameters, Bi and $\overline{c}_0$, viz

$$\frac{d\overline{\gamma}^{ds}}{d\overline{t}} = \frac{\mathrm{Bi}\overline{c}_0(1-\overline{\gamma}) - K\overline{\gamma}}{\mathrm{Da}(1-\overline{\gamma})-1}. \tag{29}$$

Correspondence between the Damköhler, Biot and Péclet Number

The kinetic scaling of the evolution equations (Eqs. (8) to (10)) clarifies the assumptions in the quasi-steady theory. By setting $\mathrm{Bi} = 0$ we essentially obtain the conditions for the solution in Eq. (21), i.e. time dependency drops out of the bulk convection-diffusion equation, consistent with an instantaneous build-up of the concentration boundary layer above the adsorbing surface in the *quasi-steady* theory. In addition, the quasi-steady theory approximates reality by a semi-infinite bulk domain, a linear velocity profile, and equally important, by no inlet distance to the sensor surface.

The kinetically scaled quasi-steady theory in Eq. (25) is parameterized only by the Damköhler number Da, and the equilibrium constant K. As the quasi-steady theory combines steady-state convection-diffusion with adsorption in the Damköhler number, through the mass transport coefficient k_L, it is naturally possible to express the Damköhler number in terms of the Péclet number and the Biot number. First, from Eq. (22), $\dot{\gamma}_\mathrm{w} = 4v_m/h$. By defining the number $\alpha = 2(4/9)^{1/3}/\Gamma(7/3) \approx 1.2819$, the mass transport coefficient k_L can be expressed as

$$k_\mathrm{L} = \alpha \left(\frac{v_m h}{D} \right)^{1/3} \frac{D}{l^{1/3} h^{2/3}}$$

Hence the Damköhler number is given by

$$\mathrm{Da} = \frac{k_\mathrm{a} \gamma_\mathrm{m}}{k_\mathrm{L}} = \alpha^{-1} (l/h)^{1/3} \, \mathrm{Bi} \, \mathrm{Pe}^{-1/3} \tag{30}$$

Note that the quasi-steady theory is parameterized by the Damköhler number, and at the same time is based on the assumption $\mathrm{Da} = 0$. It is clear from Eq. (30) that the Damköhler number increases linearly with the Biot number, and decreases with the cubic root of the Péclet number. Practically speaking, if the binders are strongly attracted to the surface (large Biot number), it may be impossible to reduce the Damköhler number significantly by simply increasing the flow rate, i.e. Péclet number.

Analytical solution of the quasi-steady theory

Eq. (25) can be solved analytically in *implicit* form, i.e. $\bar{t} = \bar{t}(\overline{\gamma})$ instead of the *explicit* form $\overline{\gamma} = \overline{\gamma}(\bar{t})$. It is determined simply by separation of variables and integration, with initially $\overline{\gamma}(\bar{t} = 0) = 0$:

$$\bar{t} = \frac{\mathrm{Da}\kappa\overline{\gamma} - \big(\kappa + \mathrm{Da}(\kappa - 1)\big)\ln(1 - \kappa\overline{\gamma})}{\kappa^2} \tag{31}$$

where $\kappa \equiv 1 + K$. For irreversible adsorption $K = 0$, $\kappa = 1$, the solution condenses into

$$\bar{t} = \mathrm{Da}\overline{\gamma} - \ln(1 - \overline{\gamma}) \tag{32}$$

This solution may not be so useful for physical insight, but has its practical advantage when performing nonlinear least squares data fitting in the time domain. Data fitting in the time domain involves a numerical solution of the ordinary differential equation (Eq. (25)) at every parameter space iteration, which can be avoided with the *implicit* solution above. Another option is simply fitting data in the phase plane.[20] This method also does not involve the solution of Eq. (25), is *explicit*, but as a trade off involves differentiation of data.

Numerical results and discussions

This section is concerned with a numerical investigation of the nonlinear system of partial differential equations, governing the evolution of the concentration fields. The intention is to simulate the dynamics of real adsorption experiments in surface-based biosensors. Numerical solutions to Eqs. (8) to (10), or similarly Eqs. (16) to (18), are collectively referred to as the *simulations*. We take offset in the estimated regime for the nondimensional parameters, and to simplify matters choose to consider the case of irreversible adsorption of binders, which are immobile on the surface, hence $K = d_s = 0$. A particular aim of the investigation is to evaluate the quality of the quasi-steady theory by comparison with the simulations. Deviations between the simulations and the quasi-steady theory reveal the effects of the transient dynamics in the simulations, which of course

are also present in real adsorption experiments. To mimic the case of real adsorption experiments, being fitted by the quasi-steady theory to reveal an adsorption rate constant k_a, we fit the quasi-steady theory to the simulation with Bi as the free fitting parameter, using a least squares method. The quasi-steady theory has no chance of fitting initial data, hence the simulation time from the origin of the phase plane to the extremum (highest adsorption rate) is cut off in the fitting procedure, corresponding to typical practice of representing SPR data in the phase plane.[20] The error of the quasi-steady theory is then quantified by the relative difference between the fitted Bi number and the real Bi number used for the simulation. Strictly speaking, we define the error as $(\mathrm{Bi}^{\mathrm{fit}} - \mathrm{Bi})/\mathrm{Bi}$. Being interested in the kinetics of adsorption the results are most naturally presented and analyzed in the phase plane, spanned by the mean surface concentration $\Gamma \equiv (1/l_c)\int_{sensor} \overline{\gamma} dx$, and its time derivative $\dot{\Gamma} \equiv (1/l_c)\int_{sensor} \partial\overline{\gamma}/\partial\bar{t}\, dx$. This representation clearly illustrates the transient regime, and is the most straightforward approach to analyze deviations from linear adsorption kinetics due to mass transport. The choice of parameters span both kinetically limited and convection-diffusion limited dynamics. Results are presented using both kinetic and diffusion scaling of time, the former leading to universality for kinetically limited dynamics, and the latter leading to universality for convection-diffusion limited dynamics. Note in particular that purely kinetically limited dynamics, i.e. the linear kinetics in Eq. (5), is represented by a linear curve in the phase plane. For kinetic scaling this linear curve is the diagonal from the point $(0,1)$ on the ordinate to the point $(1,0)$ on the abscissa. The universality characteristic obtained with kinetic scaling is that this curve represents the dynamics independent of $\overline{c}_0$ and Pe for large enough Bi.

Kinetic scaling

Figure 2 contains a representative collection of phase plane curves using kinetic scaling, i.e. $\bar{t}^{\mathrm{ks}} = k_a c_0 t$. Four different simulations for the combinations of concentrations $\overline{c}_0 \in \{1, 20\}$, $\mathrm{Bi} \in \{1, 10\}$, and $\mathrm{Pe} = 500$ are presented (full black line), each in a separate plot, along with the prediction of the quasi-steady theory for identical parameters (dashed black line), as well as a fit of the quasi-steady theory to the simulations (dashed gray line). Importantly, the quasi-steady theory scales linearly

with $\overline{c}_0$, taken into account in the kinetic scaling of time in Eq. (25). Hence the quasi-steady theory does not explicitly include the $\overline{c}_0$ - degree of freedom, whereby essentially only two distinctive predictions occur in Figure 2. In this way, the dashed black curves denoted (QST) are identical in Figure 2 (a) and (b) respectively (c) and (d). Several points are immediately apparent from the simulations. The simulation curves start at the origin of the phase plane, whereas the quasi-steady theory has the finite initial adsorption rate given in Eq. (28). It is important to note that the kinetic

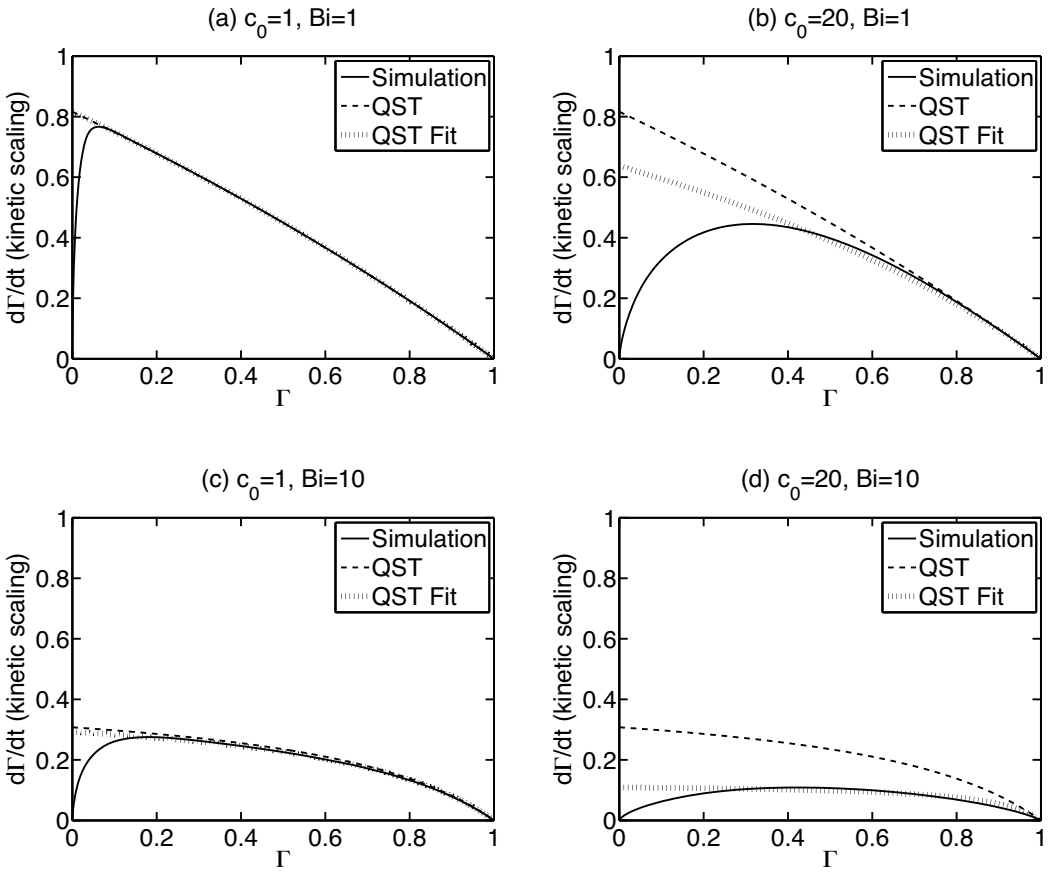

Figure 2: Phase plane dynamics using kinetic scaling. Simulation (full black line): numerical solution of Eqs. (8) to (10). QST (dashed black line): quasi-steady theory (Eq. (25)) for corresponding value of Da through Eq. (30). QST Fit (dashed gray line): fit of the quasi-steady theory to simulation with Da as free fitting parameter. Parameters: $\overline{c}_0 \in \{1, 20\}$, Bi $= \{1, 10\}$, Pe $= 500$.

scaling of time implicitly includes a linear scaling of the adsorption rate with both Bi and $\overline{c}_0$. The decrease in adsorption rate for both increasing Bi and increasing $\overline{c}_0$ in Figure 2, amounts to a sublinear increase with both Bi and $\overline{c}_0$ in dimensional variables. The sublinear scaling naturally arises from convection-diffusion limitation in the nonlinear dynamics of the system. Apart from in the initial phase, predictions of the quasi-steady theory practically coincides with the simulations, and thereby also the fits, for $\overline{c}_0 = 1$. Increasing the concentration to $\overline{c}_0 = 20$ leads to significant alteration of the simulation curves. Since there are no knobs to turn for the kinetically scaled quasi-steady theory, regarding changes in concentration $\overline{c}_0$, this leads to equally significant deviations between the simulations and predictions of the quasi-steady theory. The observed dependency of $\overline{c}_0$ is expected since $\overline{c}_0$ parameterizes time dependency in Eq. (8), and hence transient behavior in the system dynamics, which is not taken into account in the quasi-steady theory. Physically speaking, the surface simply saturates faster than a steady-state can be achieved in the bulk.

Diffusion scaling

Figure 3 contains a representative collection of phase plane curves using diffusion scaling, i.e. $\bar{t}^{\mathrm{ds}} = Dt/h^2$. Four different simulations for the combination of parameters $\overline{c}_0 \in \{20\}$, $\mathrm{Bi} = \{1, 10, 50, 100\}$, and $\mathrm{Pe} = 2500$ are presented, each in a separate plot, along with the prediction of the quasi-steady theory for identical parameters, as well as a fit of the quasi-steady theory to the simulations. The universality characteristic obtained with diffusion scaling of time is that the simulations approach a limiting curve, representing predominantly convection-diffusion limited dynamics, for large Biot numbers. This limiting curve in Figure 3 (d) is observed to have a very symmetric, parabolic-like, characteristic form. Inconsistent with the simulations, quasi-steady theory predicts a linear scaling of adsorption rate with concentration, which is explicit when using diffusion scaling as in Figure 3. This naturally leads to an increasing deviation between quasi-steady theory and simulations for increasing Bi.

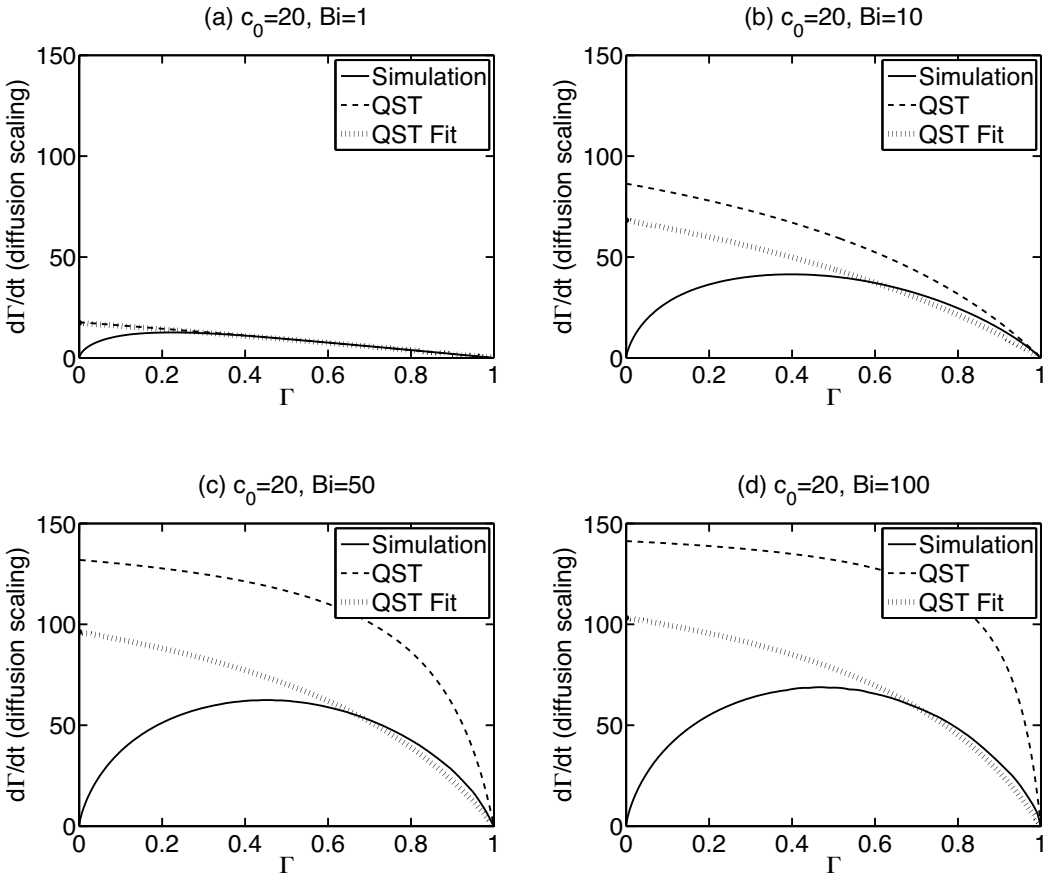

Figure 3: Phase plane dynamics using diffusion scaling. Simulation (full black line): numerical solution of Eqs. (8) to (10). QST (dashed black line): quasi-steady theory (Eq. (25)) for corresponding value of Da through Eq. (30). QST Fit (dashed gray line): fit of the quasi-steady theory to simulation with Da as free fitting parameter. Parameters: $\bar{c}_0 = 20$, Bi $= \{1, 10, 50, 100\}$, Pe $= 2500$.

Flow rate dependency

The nature of the Péclet number dependency is presented in Figure 4, containing four different simulations for the combination of parameters $\bar{c}_0 = 10$, Bi $= \{1, 100\}$, and Pe $= \{500, 10000\}$. Again, the simulations are presented, each in a separate plot, along with the prediction of the quasi-steady theory for identical parameters, as well as a fit of the quasi-steady theory to the sim-

ulations. Kinetic scaling, i.e. $\bar{t}^{\mathrm{ks}} = k_{\mathrm{a}} c_0 t$ is applied. Clearly the increase of Péclet number leads to less convection-diffusion limitation. Thereby the simulations approach the diagonal in Figure 4, representing purely adsorption limited linear kinetics, for increasing Pe. This behavior is very clear for $\mathrm{Bi} = 1$, where the dynamics is predominantly kinetically limited. For $\mathrm{Bi} = 100$, where the dynamics is much more convection-diffusion limited, we again observe increased agreement between quasi-steady theory and simulations as the Péclet number is increased. The agreement is

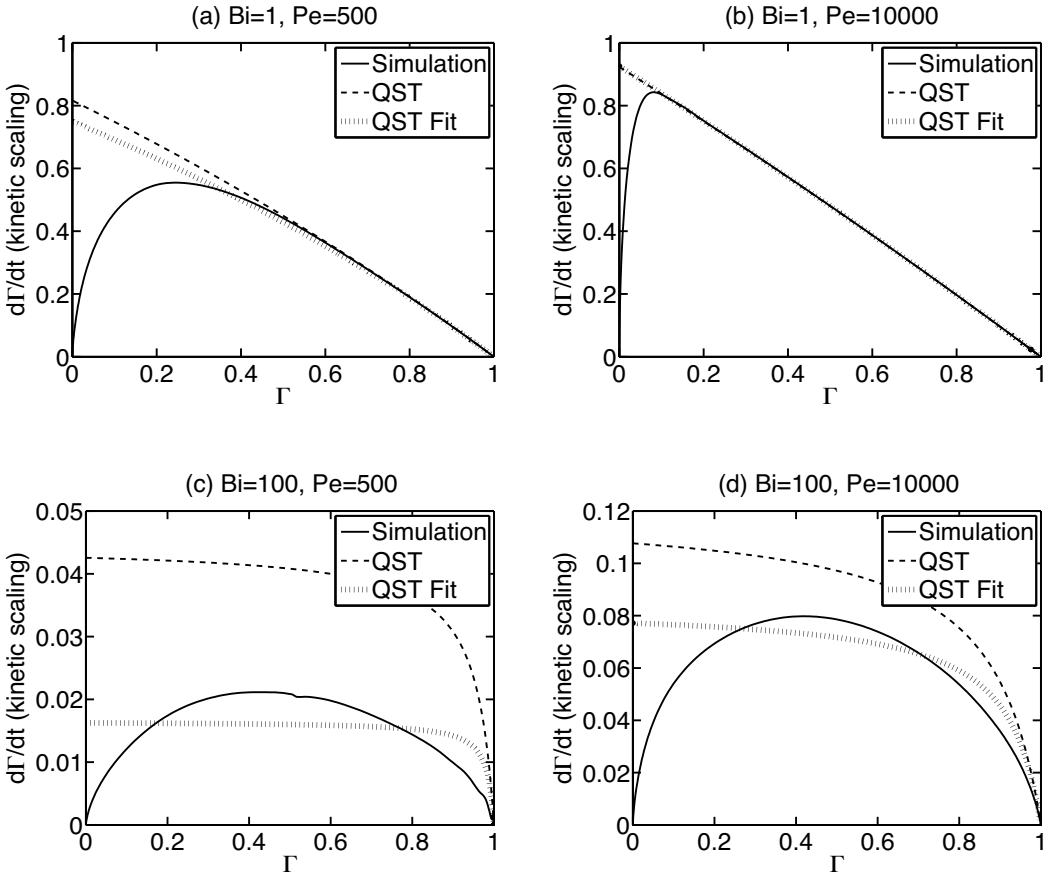

Figure 4: Phase plane dynamics using kinetic scaling. Simulation (full black line): numerical solution of Eqs. (8) to (10). QST (dashed black line): quasi-steady theory (Eq. (25)) for corresponding value of Da through Eq. (30). QST Fit (dashed gray line): fit of the quasi-steady theory to simulation with Da as free fitting parameter. Parameters: $\bar{c}_0 = 10$, $\mathrm{Bi} = \{1, 100\}$, $\mathrm{Pe} = \{500, 10000\}$.

however not as good as for $\mathrm{Bi} = 1$. Note that the ordinate axis are different in Figure 4 (c) and (d) where $\mathrm{Bi} = 100$. The specific case in Figure 4 (c), where $\bar{c}_0 = 10$, $\mathrm{Bi} = 100$, $\mathrm{Pe} = 500$, is clearly in a regime where the quasi-steady theory has little value, and little ability to fit data well. The approach to adsorption limited dynamics is consistent with a decrease in the Damköhler number as $\mathrm{Da} \sim \mathrm{Pe}^{-1/3}$ from Eq. (30). Figure 4 also serves to show that, due to this slow cubic root dependency, experimental practicalities often precludes to cope with convection-diffusion limitation by simply increasing the flow rate for systems with a high Biot number.

In summary, Figures 2 to 4 stress some nonlinearities present in the real system dynamics, which are not well captured in the approximate quasi-steady theory.

Error of the quasi-steady theory

The numerical investigation concludes with a quantification of the error of the quasi-steady theory, measured as the relative difference between the Biot number used to fit the quasi-steady theory to simulations, and the Biot number used for the simulation itself. The nondimensional parameter space is spanned by $\mathrm{Bi} \in \{1, \ldots, 100\}$, $\mathrm{Pe} \in \{500, \ldots, 10000\}$, for $\bar{c}_0 = \{1, 10, 20\}$. Figure 5 (a)-(c) present the relative error $(\mathrm{Bi}^{\mathrm{fit}} - \mathrm{Bi})/\mathrm{Bi}$, by contour lines in the nondimensional parameter space $(\mathrm{Pe}, \mathrm{Bi})$, for $\bar{c}_0 = \{1, 10, 20\}$ respectively. Every contour is labelled with the matching error. Equal for all values of $\bar{c}_0$ is that the error is largest for slow flows of strong binders, i.e. small Pe and large Bi numbers. For $\bar{c}_0 = 1$ only relatively minor errors, up to around 0.2 (20%), are observed in the spanned parameter space. However, the quantitative increase of the error with $\bar{c}_0$ is significant. For $\bar{c}_0 = 20$ the errors increase to above 2.5 (250%), which amounts to a factor of 3-4, in the spanned parameter space. Importantly, the quasi-steady theory consequently overestimates the Biot number, and thereby the adsorption rate constant, as long as the error is over a few percent. (Below errors of a few percent the fit and the prediction are so close that this is not always the case.) Hence, the parameter planes showed in Figure 5 provide a tool to quantitatively correct experimentally obtained adsorption rate constants, which are derived by fitting data with the quasi-steady theory.

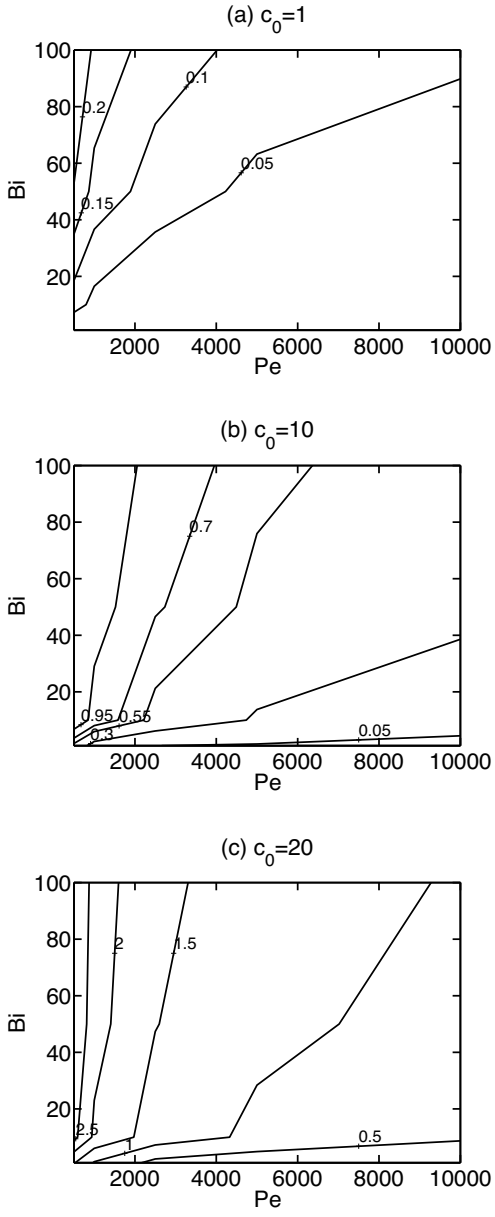

Figure 5: Contour lines of the relative error $(\mathrm{Bi}^{\mathrm{fit}} - \mathrm{Bi})/\mathrm{Bi}$, in the parameter space $(\mathrm{Pe}, \mathrm{Bi})$, for $\overline{c}_0 \in \{1, 10, 20\}$. The errors increase with increasing Bi, increasing $\overline{c}_0$, and decreasing Pe.

Conclusion

This paper presented theoretical and computational investigations of convection, diffusion, and adsorption dynamics in microfluidic surface-based biosensors. The nondimensional Damköhler number $\mathrm{Da} = k_\mathrm{a}\gamma_\mathrm{m}/k_\mathrm{L}$, inherent in the quasi-steady theory, was expressed in terms of the Biot number $\mathrm{Bi} = k_\mathrm{a}\gamma_\mathrm{m}h/D$, the Péclet number $\mathrm{Pe} = v_m h/D$, and the model geometry. In addition, an analytical solution to the quasi-steady theory was derived. The results provided the regimes of both reliable and unreliable use of the quasi-steady theory for experimental data analysis, by quantifying the error of the quasi-steady theory in the space of parameters. This can be used as a tool to correct adsorption rate constants obtained by fitting the quasi-steady theory to experimental data. We deduced a critical importance of the inlet concentration, and the maximum surface capacity, combined in the nondimensional inlet concentration.

References

(1) Stenberg, E.; Persson, B.; Roos, H.; Urbaniczky, C. *Journal of Colloid and Interface Science* **1991**, *143*, 513 – 526.

(2) Homola, J.; Yee, S.; Gauglitz, G. *SENSORS AND ACTUATORS B-CHEMICAL* **1999**, *54*, 3–15.

(3) Homola, J. *Chem Rev* **2008**, *108*, 462–93.

(4) Schuck, P.; Minton, A. *ANALYTICAL BIOCHEMISTRY* **1996**, *240*, 262–272.

(5) Myszka, D. G.; He, X.; Dembo, M.; Morton, T. A.; Goldstein, B. *Biophys J* **1998 Aug**, *75*, 583–594.

(6) Schuck, P. *Biophys J* **1996**, *70*, 1230–49.

(7) Schuck, P.; Minton, A. P. *Anal Biochem* **1996**, *240*, 262–72.

(8) Mason, T.; Pineda, A. R.; Wofsy, C.; Goldstein, B. *Math Biosci* **1999**, *159*, 123–44.

(9) Noinville, S.; Vidic, J.; Déjardin, P. *Colloids Surf B Biointerfaces* **2010**, *76*, 112–6.

(10) Goldstein, B.; Coombs, D.; He, X.; Pineda, A. R.; Wofsy, C. *J Mol Recognit* **1999 Sep-Oct**, *12*, 293–299.

(11) Rich, R. L.; Myszka, D. G. *J Mol Recognit* **2011**, *24*, 892–914.

(12) Rich, R. L.; Myszka, D. G. *J Mol Recognit* **2010**, *23*, 1–64.

(13) Rich, R. L.; Myszka, D. G. *J Mol Recognit* **2008**, *21*, 355–400.

(14) Rich, R. L.; Myszka, D. G. *J Mol Recognit* **2007**, *20*, 300–66.

(15) Besenicar, M.; Macek, P.; Lakey, J. H.; Anderluh, G. *Chem Phys Lipids* **2006**, *141*, 169–78.

(16) Brody, J. P.; Yager, P.; Goldstein, R. E.; Austin, R. H. *Biophys J* **1996**, *71*, 3430–41.

(17) Gervais, T.; Jensen, K. F. *Chemical Engineering Science* **2006**, *61*, 1102 – 1121.

(18) Alvarez, N. J.; Walker, L. M.; Anna, S. L. *Phys. Rev. E* **2010**, *82*, 011604.

(19) Squires, T. M.; Messinger, R. J.; Manalis, S. R. *Nat Biotechnol* **2008**, *26*, 417–26.

(20) Goren, M.; Galley, N.; Lennox, R. B. *Langmuir* **2006 Jan 31**, *22*, 1048–1054.

[P2]

Rheol Acta (2010) 49:555–562
DOI 10.1007/s00397-010-0434-0

ORIGINAL CONTRIBUTION

Constitutive equations for the Doi–Edwards model without independent alignment

Ole Hassager · Rasmus Hansen

Received: 25 October 2009 / Accepted: 12 January 2010 / Published online: 6 March 2010

Abstract We present two representations of the Doi–Edwards model without Independent Alignment explicitly expressed in terms of the Finger strain tensor, its inverse and its invariants. The two representations provide explicit expressions for the stress prior to and after Rouse relaxation of chain stretch, respectively. The maximum deviations from the exact representations in simple shear, biaxial extension and uniaxial extension are of order 2%. Based on these two representations, we propose a framework for Doi–Edwards models including chain stretch in the memory integral form.

Keywords Constitutive equation · Nonlinear viscoelasticity · Orientation tensor · Strain energy density · Second normal stress difference · Tube model

Introduction

Representing a landmark in our understanding of the dynamics of entangled polymeric systems, the Doi–Edwards model (DE) model (Doi and Edwards 1986) is based on a set of remarkably simple model assumptions (Doi 1995). The basic DE model for the nonlinear viscoelastic properties contains two key assumptions about how the central axis of the tube deforms under a macroscopic deformation. It is assumed that the tube axis deforms affinely with the deformation, and that after a time τ_R, the tube length returns to its equilibrium value.

The basic DE model is found in two versions, one with the so-called Independent Alignment (IA) approximation and one without this approximation (Doi and Edwards 1978). Both models require the calculation of an integral over the unit sphere for each stress evaluation. Methods for fast stress evaluation are therefore interesting (Mead et al. 1995). Especially convenient expressions have been presented by Currie (1982a, b), who formulated BKZ memory integral models (Bird et al. 1987) intended to approximate the constitutive equation for the DE model both with (Currie 1982a) and without (Currie 1982b) IA invoked.

The Currie equation with IA has been used and tested extensively in modeling and simulation of polymer flow (Marin and Rasmussen 2009; Wapperom and Keunings 2001; Blackwell et al. 2000; Olley 2005; Mead 2007; Peters et al. 2000; Olley and Wagner 2006; Wagner 1990). The Currie equation without IA has received much less attention, nor does the accuracy of approximation seem to have been systematically tested, possibly because Currie states that it "differs little in its predictions" from the approximation to the IA version. This latter statement, however does seem in contrast to the observations that the nonlinear rheological properties of the DE model with and without IA differ markedly in specific flow situations. Thus, the DE model with IA predicts a negative Weissenberg effect (Hassager 1985) while the version without IA predicts a positive Weissenberg effect as pointed out by

Paper presented at the 5th Annual European Rheology Conference, April 15–17, 2009, Cardiff, United Kingdom.

O. Hassager (✉) · R. Hansen
Danish Polymer Center, Department of Chemical and Biochemical Engineering, Technical University of Denmark, 2800 Kgs. Lyngby, Denmark
e-mail: OH@kt.dtu.dk

Marrucci and Grizzuti (1986) who performed a careful comparison of the two versions at second order.

The purpose of this work is to derive constitutive equations for the DE model without IA both prior to and after Rouse relaxation (Doi and Edwards 1986) and to evaluate the accuracy of the approximations in simple shear, biaxial extension and uniaxial extension. To fix ideas and notation we briefly recapitulate the derivation of the relevant equations starting from the expression for the free energy of deformation of an entanglement network (Doi 1995; Hansen et al. 2008)

$$A = \frac{3}{2} n_c Z k T \langle |\mathbf{E} \cdot \boldsymbol{u}| \rangle_{\boldsymbol{u}}^2 \tag{1}$$

Here n_c is the number density of chains, Z the number of entanglements per chain, k Boltzmanns constant, and T the absolute temperature. Furthermore, $\mathbf{E}$ is the deformation gradient (Bird et al. 1987) from the stress-free state to the current state, $\boldsymbol{u}$ is a unit vector, and $\langle \cdots \rangle_{\boldsymbol{u}}$ denotes an average over the orientation of the 3-dimensional unit vector $\boldsymbol{u}$, i.e., an isotropic distribution. From this expression, it is straightforward to derive (e.g. Hansen et al. 2008) the corresponding expression for the macroscopic stress tensor,

$$\sigma_{ij}^{net} = G_0 \frac{15}{4} \langle |\mathbf{E} \cdot \boldsymbol{u}| \rangle_{\boldsymbol{u}} \left\langle \frac{E_{im} u_m E_{jn} u_n}{|\mathbf{E} \cdot \boldsymbol{u}|} \right\rangle_{\boldsymbol{u}} \tag{2}$$

where the elastic modulus $G_0 = (4/5) n_c Z k T$. The combination of factors after the modulus is sometimes referred to as a strain tensor, since it reduces to the infinitesimal strain tensor in the small strain limit. The decoration "net" signifies that the expression relates to an entanglement network without relaxation of the overall chain length.

Consider now an entangled polymer melt subject to a single fast deformation given by the deformation gradient $\mathbf{E}$. For time $t > \tau_R$ when the tube has relaxed to its equilibrium value, the stress is reduced by the square of the initial chain stretch to obtain,

$$\sigma_{ij} = G_0^N \frac{15}{4} \langle |\mathbf{E} \cdot \boldsymbol{u}| \rangle_{\boldsymbol{u}}^{-1} \left\langle \frac{E_{im} u_m E_{jn} u_n}{|\mathbf{E} \cdot \boldsymbol{u}|} \right\rangle_{\boldsymbol{u}} \tag{3}$$

where the plateau modules $G_0^N = (4/5) n_c Z k T$ is unchanged since the average stretch is unity in the small strain limit. To simplify further, Doi and Edwards introduced the Independent Alignment Assumption, which effectively replaces the ratio of averages with the average of the ratio. Such a replacement is problematic as Doi and Edwards were well aware (Doi and Edwards 1986). Thus for small deformations, the ratio of the averages and the average of the ratio are expanded in the infinitesimal strain tensor ϵ_{ij} respectively as follows:

$$\langle |\mathbf{E} \cdot \boldsymbol{u}| \rangle_{\boldsymbol{u}}^{-1} \left\langle \frac{E_{im} u_m E_{jn} u_n}{|\mathbf{E} \cdot \boldsymbol{u}|} \right\rangle_{\boldsymbol{u}} = \delta_{ij} + \frac{4}{15} \epsilon_{ij} + O\left(\epsilon_{ij}^2\right) \tag{4}$$

$$\left\langle \frac{E_{im} u_m E_{jn} u_n}{|\mathbf{E} \cdot \boldsymbol{u}||\mathbf{E} \cdot \boldsymbol{u}|} \right\rangle_{\boldsymbol{u}} = \delta_{ij} + \frac{1}{5} \epsilon_{ij} + O\left(\epsilon_{ij}^2\right) \tag{5}$$

In other words, the only term correctly reproduced in the IA approximation is the unit tensor. But the unit tensor has no rheological significance. The linear term in ϵ_{ij} is under-predicted by a factor of 3/4. This factor is not a problem in practical applications, since one can simply scale the modulus accordingly (Mead 2007). But the difference between the $O(\epsilon_{ij}^2)$ terms in Eqs. 4 and 5 is at the heart of the difference between negative and positive Weissenberg effects (Marrucci and Grizzuti 1986).

From the above it appears that we need to approximate $\langle |\mathbf{E} \cdot \boldsymbol{u}| \rangle_{\boldsymbol{u}}^2$ in terms of the invariants of the Finger and Cauchy strain tensors of nonlinear elasticity. Following Currie, we consider in turn an exact expression, an asymptotic form, and the small strain expansion. The final approximation is arrived at by matching the asymptotic form with the small strain expansion.

Evaluation of potential function

For uniaxial and biaxial deformation one may utilize the axial symmetry to obtain the simple analytical expressions for the desired integral (Urakawa et al. 1995). We list the expressions for future reference. For uniaxial extension $\lambda_1 = \lambda$ and $\lambda_2 = \lambda_3 = \lambda^{-1/2}$ the exact expression is

$$\langle |\mathbf{E} \cdot \boldsymbol{u}| \rangle = \frac{1}{2} \lambda + \frac{1}{4} \frac{\lambda^{-1}}{\sqrt{\lambda^2 - \lambda^{-1}}} \log \frac{\lambda + \sqrt{\lambda^2 - \lambda^{-1}}}{\lambda - \sqrt{\lambda^2 - \lambda^{-1}}} \tag{6}$$

For biaxial extension $\lambda_1 = \lambda_2 = \lambda$ and $\lambda_3 = \lambda^{-2}$ the exact expression is

$$\langle |\mathbf{E} \cdot \boldsymbol{u}| \rangle = \frac{1}{2} \left(\lambda^{-2} + \frac{\lambda}{\sqrt{1 - \lambda^{-6}}} \sin^{-1} \sqrt{1 - \lambda^{-6}} \right) \tag{7}$$

For general deformations we need to compute

$$\langle |\mathbf{E} \cdot \boldsymbol{u}| \rangle = \left\langle \sqrt{\bar{B}_{ij} u_i u_j} \right\rangle \tag{8}$$

where $\bar{B}_{ij} = E_{mi} E_{mj}$ is not the same as the Finger strain tensor $B_{ij} = E_{im} E_{jm}$ but the two matrices have the same eigenvalues λ_i^2 for $i = 1, 2, 3$. Without loss of generality we can order the eigenvalues $\lambda_1^2 \geq \lambda_2^2 \geq \lambda_3^2$.

Then

$$\langle|\mathbf{E}\cdot\boldsymbol{u}|\rangle = \frac{1}{4\pi}\int_{\theta=0}^{\pi}\int_{\phi=0}^{2\pi} \times\sqrt{\lambda_1^2\cos^2\theta + (\lambda_2^2\cos^2\phi + \lambda_3^2\sin^2\phi)\sin^2\theta}\,\sin\theta\,\mathrm{d}\theta\,d\phi \tag{9}$$

The integration on θ can be performed to obtain the exact forms

$$\langle|\mathbf{E}\cdot\boldsymbol{u}|\rangle = \frac{1}{2}\lambda_1 + \frac{1}{2\pi}\int_0^{\pi/2}\frac{a^2}{b}\log\frac{\lambda_1+b}{\lambda_1-b}\mathrm{d}\phi \tag{10}$$

$$= \frac{1}{2}\lambda_1 + \frac{1}{\pi}\int_0^{\pi/2}\frac{a^2}{b}\sinh^{-1}B\mathrm{d}\phi \tag{11}$$

where $a^2 = \lambda_2^2\cos^2\phi + \lambda_3^2\sin^2\phi$ and $b^2 = \lambda_1^2 - a^2$. The notation $B = b/a$ is the same as introduced by Currie.

Asymptotic behavior

We now follow Currie and let $\lambda_1 \to \infty$ while assuming that λ_2 stays finite. This covers simple shear flow ($\lambda_2 = 1$) and uniaxial extension ($\lambda_2 \to 0$). Since $\sinh^{-1}x \sim \log(2x)$ for $x \to \infty$ we have that

$$\langle|\mathbf{E}\cdot\boldsymbol{u}|\rangle \sim \frac{1}{2}\lambda_1 + \frac{1}{4}\frac{\lambda_2^2+\lambda_3^2}{\lambda_1}(\log 2 + \log\lambda_1) \tag{12}$$

Secondly, we consider the situation in which $\lambda_2 = \alpha\lambda_1$ for $\alpha \in]0;1]$ as $\lambda_1 \to \infty$. The corresponding asymptotic form is now

$$\langle|\mathbf{E}\cdot\boldsymbol{u}|\rangle \sim \frac{1}{2}\lambda_1 + \frac{\lambda_2^2}{\lambda_1}F(\alpha) \tag{13}$$

where

$$F(\alpha) = \frac{1}{2\pi}\int_0^{\pi/2}\frac{\cos^2\phi}{\sqrt{1-\alpha^2\cos^2\phi}}\log\frac{1+\sqrt{1-\alpha^2\cos^2\phi}}{1-\sqrt{1-\alpha^2\cos^2\phi}}\mathrm{d}\phi \tag{14}$$

The function $F(\alpha)$ may be closely approximated by a function of the form $\frac{1}{4}(0.87 + 0.28\alpha - \log\alpha)$ as shown in Fig. 1.

This suggests therefore an asymptotic behavior of the form,

$$\langle|\mathbf{E}\cdot\boldsymbol{u}|\rangle \sim \frac{1}{2}\lambda_1 + \frac{1}{4}\frac{\lambda_2^2}{\lambda_1}\left(c_0 + c_1\alpha + \log\frac{\lambda_1}{\lambda_2}\right) \tag{15}$$

where c_0 and c_1 are adjustable constants related to the asymptotic behavior.

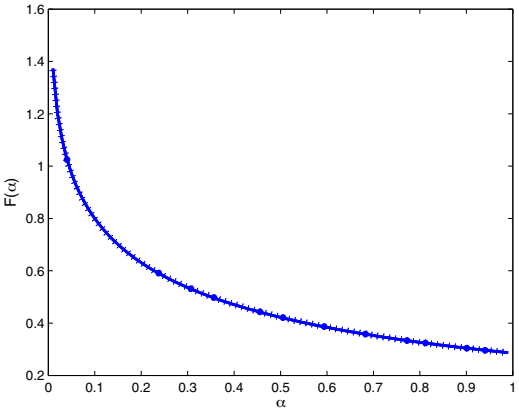

Fig. 1 Comparison of exact integral $F(\alpha)$ from Eq. 14 (*full line*) with approximation $(0.87 + 0.28\alpha - \log\alpha)/4$ (*dashed line*). The two functions are practically indistinguishable

The leading term in Eq. 15 will always be the largest one. This suggests that we may approximate the asymptotic behavior of the square by

$$\langle|\mathbf{E}\cdot\boldsymbol{u}|\rangle^2 \sim \frac{1}{4}\lambda_1^2 + \frac{1}{4}\lambda_2^2\left(c_0 + c_1\frac{\lambda_2}{\lambda_1} + \log\frac{\lambda_1}{\lambda_2}\right) \tag{16}$$

The three eigenvalues are not independent since they are tied by the incompressibility relation $\lambda_1\lambda_2\lambda_3 = 1$. We therefore need to convert the expression to a function of the strain invariants $I_1 = \lambda_1^2 + \lambda_2^2 + \lambda_3^2$ and $I_2 = \lambda_1^{-2} + \lambda_2^{-2} + \lambda_3^{-2}$. For $\lambda_1 \to \infty$ we use $\lambda_1^2 + \lambda_2^2 \sim I_1$ and $\lambda_1^2\lambda_2^2 \sim I_2$. Hence we substitute for the eigenvalues $\lambda_1^2 = I_1 - I_2/I_1$ and $\lambda_2^2 = I_2/I_1$ to obtain

$$\langle|\mathbf{E}\cdot\boldsymbol{u}|\rangle^2 \sim \frac{1}{4}I_1 + \frac{1}{4}\frac{I_2}{I_1}\left(c_0 - 1 + c_1\frac{I_2^{1/2}}{I_1} + \log I_1 - \frac{1}{2}\log I_2\right) \tag{17}$$

We retain the value of c_0 from the comparison in Fig. 1 but keep the value of c_1 as an adjustable constant. Following Currie, however we use rational fractions leading to $c_0 - 1 = -\frac{1}{8}$. The asymptotic behavior in uniaxial extension and shear is unaffected by c_1. In biaxial extension, we note from Eq. 7 that $\langle|\mathbf{E}\cdot\boldsymbol{u}|\rangle^2 \sim (\pi\lambda/4)^2$ as $\lambda \to \infty$. This behavior is closely matched by $c_1 = 3/4$.

Small strain expansion

For small strains it is convenient to rewrite the stretch factor in the form

$$|\mathbf{E}\cdot\boldsymbol{u}| = \sqrt{1 + \boldsymbol{\epsilon} : \boldsymbol{uu}} \tag{18}$$

where $\boldsymbol{\epsilon} = \mathrm{diag}(\lambda_1^2 - 1, \lambda_2^2 - 1, \lambda_3^2 - 1) = \mathrm{diag}(\epsilon_1, \epsilon_2, \epsilon_3)$. The ϵ_i are not independent due to the incompressibility condition. But we may choose ϵ_1 and ϵ_2 as free parameters. Then to third order,

$$\epsilon_3 = -\epsilon_1 - \epsilon_2 + \epsilon_1^2 + \epsilon_2^2 + \epsilon_1\epsilon_2 - \epsilon_1^3 - \epsilon_1^2\epsilon_2 - \epsilon_1\epsilon_2^2 - \epsilon_2^3 + O(\epsilon^4) \tag{19}$$

where $O(\epsilon^4)$ indicates terms $\epsilon_1^i\epsilon_2^j$ with $i + j \geq 4$. Likewise the two strain invariants need to be expanded

$$I_1 - 3 = \epsilon_1^2 + \epsilon_2^2 + \epsilon_1\epsilon_2 - \epsilon_1^3 - \epsilon_1^2\epsilon_2 - \epsilon_1\epsilon_2^2 - \epsilon_2^3 + O(\epsilon^4) \tag{20}$$

$$I_2 - 3 = \epsilon_1^2 + \epsilon_2^2 + \epsilon_1\epsilon_2 - \epsilon_1^3 - \epsilon_2^3 + O(\epsilon^4) \tag{21}$$

By expansion of Eq. 18 for small strains one obtains

$$|\mathbf{E}\cdot\boldsymbol{u}| = 1 + \frac{1}{2}\epsilon_{ij}u_iu_j - \frac{1}{8}\epsilon_{ij}\epsilon_{kl}u_iu_ju_ku_l + \frac{3}{48}\epsilon_{ij}\epsilon_{kl}\epsilon_{mn}u_iu_ju_ku_lu_mu_n + \cdots \tag{22}$$

It is now straightforward but somewhat tedious to obtain the expansion for $\langle|\mathbf{E}\cdot\boldsymbol{u}|\rangle$ to third order in the ϵ_i by utilizing the expression for averages of products of unit vectors over the unit sphere. Explicit expression to sixth order in the u_i as needed here may be found in Bird et al. (1977). By matching the resulting expression with Eqs. 20 and 21 one obtains to first order in the strain invariants,

$$\langle|\mathbf{E}\cdot\boldsymbol{u}|\rangle = 1 + \frac{2}{105}(6(I_1 - 3) + (I_2 - 3)) + \cdots \tag{23}$$

Hence the potential becomes

$$\langle|\mathbf{E}\cdot\boldsymbol{u}|\rangle^2 = 1 + \frac{4}{105}(6(I_1 - 3) + (I_2 - 3)) + \cdots \tag{24}$$

Matching expression

We now wish to construct a function $U(I_1, I_2)$ that matches the asymptotic behavior of $\langle|\mathbf{E}\cdot\boldsymbol{u}|\rangle^2$ in Eq. 17 with the small strain behavior in Eq. 24. In particular we propose

$$U(I_1, I_2) = \frac{1}{4}I_1 + \frac{1}{4}\frac{I_2}{I_1}\left(-\frac{1}{8} + \frac{3}{4}\frac{I_2^{1/2}}{I_1} + \log I_1 - \frac{1}{2}\log I_2\right) + \frac{a_1}{I_1} + \frac{a_2}{I_2} + a_3 \tag{25}$$

for some constants a_i $(i = 1, 2, 3)$ that are determined by the requirements

$$U(3, 3) = 1 \tag{26}$$

$$\frac{\partial U}{\partial I_1}(3, 3) = \frac{8}{35} \tag{27}$$

$$\frac{\partial U}{\partial I_2}(3, 3) = \frac{4}{105} \tag{28}$$

The following results are obtained,

$$a_1 = +\frac{1161}{1120} - \frac{3\sqrt{3}}{8} - \frac{3}{8}\log 3 \doteq -0.0249 \tag{29}$$

$$a_2 = -\frac{909}{1120} + \frac{9\sqrt{3}}{32} + \frac{3}{8}\log 3 \doteq +0.0875 \tag{30}$$

$$a_3 = +\frac{33}{160} - \frac{1}{32}\sqrt{3} - \frac{1}{8}\log 3 \doteq +0.0148 \tag{31}$$

The small numerical values of the constants a_i indicates that the asymptotic form is already a reasonable good approximation to the potential. We may check the function $U(I_1, I_2)$ along the two types of deformation that span the available invariant space, namely uniaxial (Fig. 2) and biaxial (Fig. 3) extension.

It appears that the potential in Eq. 25 approximates the exact potential to better than 2.5% in uniaxial and biaxial deformations. Since these two types of deformation bound the available space for the invariants I_1 and I_2 we use it as approximation in the entire invariant space.

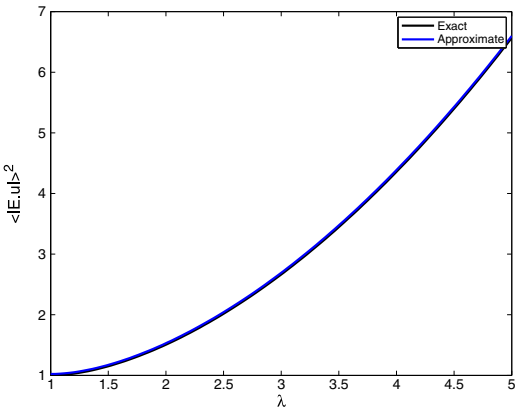

Fig. 2 Plot of approximate potential U from Eq. 25 and exact potential Eq. 6 in uniaxial deformation as function of λ. The two curves practically overlap. The maximum relative deviation (2.3%) occurs at intermediate λ values

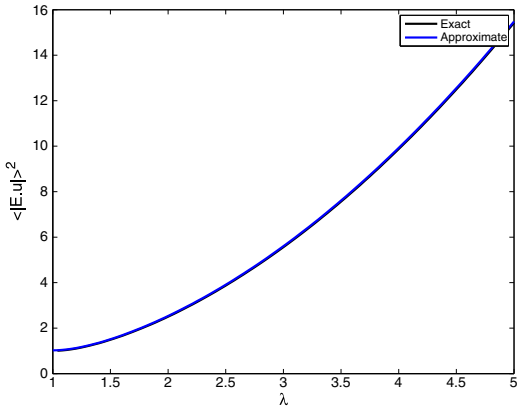

Fig. 3 Plot of approximate potential U from Eq. 25 with exact potential Eq. 7 in biaxial deformation. The two curves practically overlap. The maximum relative deviation (2.3%) occurs at intermediate λ values

DE Constitutive equations

To arrive at the corresponding constitutive equation one substitutes Eq. 25 into Eq. 1 to arrive at the free energy,

$$A = \frac{3}{2} n_c Z k T U(I_1, I_2) \tag{32}$$

From this one arrives by standard procedure (Bird et al. 1987) at the constitutive relation for the unrelaxed entanglement network prior to Rouse relaxation,

$$\sigma_{ij}^{net} = G_0 \left(f_1 B_{ij} - f_2 B_{ij}^{-1} \right) \tag{33}$$

$$f_1 = \frac{15}{16} \left(1 - \frac{3}{2} \frac{I_2^{3/2}}{I_1^3} + \frac{I_2}{I_1^2} \left(\frac{9}{8} - \log I_1 + \frac{1}{2} \log I_2 \right) - \frac{4 a_1}{I_1^2} \right) \tag{34}$$

$$f_2 = \frac{15}{16} \left(\frac{9}{8} \frac{I_2^{1/2}}{I_1^2} + \frac{1}{I_1} \left(-\frac{5}{8} + \log I_1 - \frac{1}{2} \log I_2 \right) - \frac{4 a_2}{I_2^2} \right) \tag{35}$$

where $B_{ij} = E_{in} E_{jn}$ are the components of the Finger strain tensor and B_{ij}^{-1} are the components of the Cauchy strain tensor. The expression for the modulus is $G_0 = (4/5) n_c Z k T$ as in the exact DE model. It is now also simple to construct a memory integral expansion that approximates the Doi-Edwards model with instantaneous chain retraction (that is after Rouse relaxation) but without the Independent Alignment Assumption.

$$\sigma_{ij} = \int_{t'=-\infty}^{t} M(t - t') \left(\phi_1 B_{ij} - \phi_2 B_{ij}^{-1} \right) \mathrm{d}t' \tag{36}$$

where M is the memory function, $\phi_i = f_i / U$ and U is the square of the average stretch.

Simple shear

Uniaxial and biaxial stretching form the bounding curves for the available part of the invariant space (I_1, I_2) (Bird et al. 1987). As a final test we consider simple shear of shear magnitude γ so that $x_1 = x_1' + \gamma x_2'$, where the primed and unprimed coordinates are before respectively after deformation. Now for simple shear $I_1 = I_2 = 3 + \gamma^2$ so the deformations lie in the middle of the available invariant space. We compute the damping function $h(\gamma)$ and the normal stress ratio $-N_2/N_1$ defined below

$$h(\gamma) = \frac{\sigma_{12}}{\gamma G_0^N} = \phi_1 + \phi_2 \tag{37}$$

$$-\frac{N_2}{N_1} = -\frac{\sigma_{22} - \sigma_{33}}{\sigma_{11} - \sigma_{22}} = \frac{\phi_2}{\phi_1 + \phi_2} \tag{38}$$

Exact values for the two functions were reported by Osaki and coworkers in Osaki et al. (1982) and Osaki et al. (1981). In Figs. 4 and 5 we compare the predictions from Eqs. 37 and 38 with the exact values computed from Eq. 3. It may be shown that Eqs. 37 has the

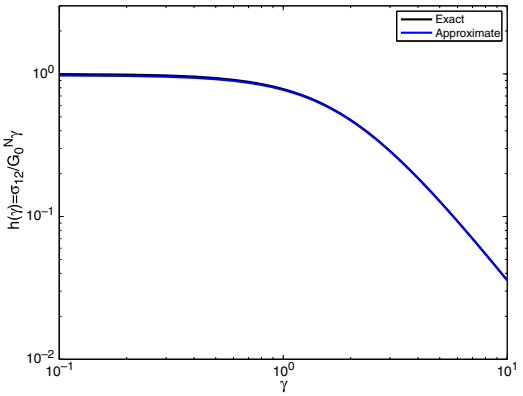

Fig. 4 Plot of the damping function in simple shear for the DE model without IA. Predictions from the approximate constitutive equation and exact values are identical in the limits of large and small strain. The maximum relative deviation (2.2%) occurs at intermediate λ values

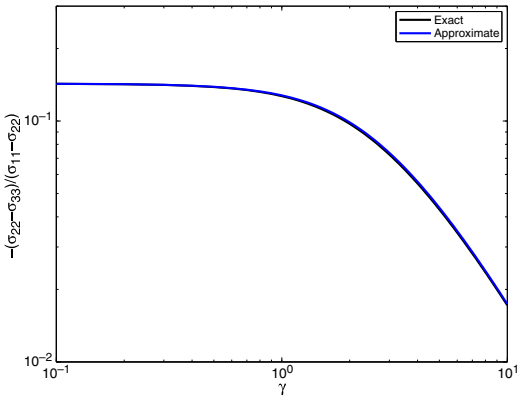

Fig. 5 Plot of the normal stress ratio in simple shear for the DE model without IA. Predictions from the approximate constitutive equation and exact values are identical in the limits of large and small strain. The maximum relative deviation (1.8%) occurs at intermediate λ values

behavior $h(\gamma) \sim (15/4)\gamma^{-2}$ as $\gamma \to \infty$ which is exactly the same asymptotic behavior as for the exact equation in 3. For comparison, the IA version has the asymptotic behavior $h(\gamma) \sim 5\gamma^{-2}$ as $\gamma \to \infty$ which departs from the correct behavior by 33%. Also the asymptotic form of the normal stress ratio from Eq. 38 is $-N_2/N_1 \sim \gamma^{-2}\log\gamma$ which is identical to the asymptotic behavior of the exact expression (as shown in the Appendix). By contrast the IA approximation changes the asymptotic behavior to $-N_2/N_1 \sim \gamma^{-1}$. Thus the IA approximation results in marked changes in the normal stress ratio, not just in the low shear limit, but more drastically in the asymptotic behavior.

In closing we note that Currie approximation for the DE model without independent alignment (Currie 1982b) approximates the damping function and the small shear behavior of $-N_2/N_1$ closely but fails to approximate the asymptotic behavior of the normal stress ratio. The Currie approximation yields $-N_2/N_1 \sim (2\sqrt{3}\gamma)^{-1}$ for $\gamma \to \infty$, which apart from the numerical factor is the same as the behavior for the IA version, but not the correct behavior.

Constitutive equations with stretch relaxation

The DE melt model in form Eq. 36 contains the assumption of instantaneous relaxation of the chains to their equilibrium length. However it was recognized early that chain stretching in uncrosslinked entangled polymer systems will occur at deformation rates faster than the inverse Rouse time (Maruucci and Grizzutti 1988; Pearson et al. 1989). The concept of chain stretching is now standard in reptation-based models (Fang et al. 2000; Mead et al. 1998; Schieber et al. 2003). Given the stretch function $U(I_1, I_2)$ it is straightforward to formulate models with Rouse dynamics for the chain stretch. For example assuming that stretch relaxation is dominated by a single Rouse relaxation time, a possible description (Lyhne et al. 2009) would be:

$$\lambda^2(t,t') = \left[1 + (\sqrt{U(t,t')} - 1)\exp(-(t-t')/\tau_R)\right]^2 \quad (39)$$

where the stretch relaxation time τ_R is the Rouse time. The corresponding constitutive equation is then,

$$\sigma_{ij} = \int_{t'=-\infty}^{t} \lambda^2(t,t')\, M(t-t') \left(\phi_1 B_{ij} - \phi_2 B_{ij}^{-1}\right) \mathrm{d}t'. \quad (40)$$

Conclusions

The key to the constitutive equations is the development of an accurate representation of the unrelaxed entanglement network in terms of the invariants of the Finger strain tensor. Based on this representation it has been possible to formulate constitutive equations for the unrelaxed network and for the completely relaxed network both without the independent alignment approximation. The representations have the exact behavior for small strain and show the correct asymptotic behavior in simple shear, biaxial and uniaxial deformations. In the intermediate range, the maximum deviations from the exact behavior in the deformations investigated is of order 2%. In closing, a model is proposed for a network with partial relaxation, corresponding to a DE model with chain stretch. It is formulated in a form with a single stretch relaxation time, but may easily be generalized to multiple relaxation times.

Acknowledgements The authors would like to thank Stig Wedel and Jose Marin for critical and constructive comments. Rasmus Hansen is supported by the Danish Agency for Science, Technology and Production and by Novozymes A/S.

Appendix on asymptotic normal stress ratio in shear

Given a shear deformation of magnitude γ, the length of the deformed unit vector may be written in the form

$$|\mathbf{E}\cdot\boldsymbol{u}| = \left(1 + \sin^2\theta f(\phi)\right)^{1/2} \quad (41)$$

where $f(\phi)$ is given by

$$f(\phi) = \frac{1}{2}\left(1+\gamma^2\right)(1-\cos 2\phi) + \gamma\sin 2\phi \quad (42)$$

It follows that $f(\phi)$ has a minimum at

$$\phi_m = -\frac{1}{2}\tan^{-1}\frac{2\gamma}{1+\gamma^2} \sim -\gamma^{-1} \text{ for } \gamma \to \infty \tag{43}$$

It may be shown that $f(\phi)$ has the Taylor expansion

$$f(\phi) = \left(-1+2\gamma^{-2}\right) + \left(\phi+\gamma^{-1}\right)^2\gamma^2 + \cdots \tag{44}$$

around $\phi = -\gamma^{-1}$. It follows that in this region we may approximate

$$|\mathbf{E}\cdot\boldsymbol{u}| = \gamma\sin\theta\left(a^2+x^2\right)^{1/2} \tag{45}$$

where

$$a^2 = \gamma^{-2}\left(\cot^2\theta + 2\gamma^{-2}\right)$$

and $x = \phi + \gamma^{-1}$.

The negative of the second normal stress is computed from

$$(\sigma_{zz}-\sigma_{yy})/G_0 = I = \frac{1}{4\pi}\int_{\theta=0}^{\pi}\int_{\phi=0}^{2\pi} \times\frac{\left(\cos^2\theta-\sin^2\theta\sin^2\phi\right)\sin\theta\,\mathrm{d}\theta\,\mathrm{d}\phi}{|\mathbf{E}\cdot\boldsymbol{u}|} \tag{46}$$

The periodicity of the harmonic functions may be utilized to show that

$$I = \frac{1}{\pi}\int_{\theta=0}^{\pi/2}\int_{\phi=0}^{\pi}\frac{\left(\cos^2\theta-\sin^2\theta\sin^2\phi\right)\sin\theta\,\mathrm{d}\theta\,\mathrm{d}\phi}{|\mathbf{E}\cdot\boldsymbol{u}|} \tag{47}$$

$$= \frac{1}{\pi}\int_{\theta=0}^{\pi/2}\int_{\phi=-\gamma^{-1}}^{\pi-\gamma^{-1}}\frac{\left(\cos^2\theta-\sin^2\theta\sin^2\phi\right)\sin\theta\,\mathrm{d}\theta\,\mathrm{d}\phi}{|\mathbf{E}\cdot\boldsymbol{u}|} \tag{48}$$

$$\approx \frac{2}{\pi\gamma}\int_{\theta=0}^{\pi/2}\int_{x=0}^{A}\frac{\left(\cos^2\theta-\sin^2\theta\ \sin^2\left(x-\gamma^{-1}\right)\right)\mathrm{d}\theta\,\mathrm{d}x}{\left(a^2+x^2\right)^{1/2}} \tag{49}$$

In going from Eqs. 48 to 49 we have used that the major contribution to the integral will occur near $x = 0$ and that the maximum becomes symmetric around $x = 0$. We therefore integrate up to some limit $A \in [0;\pi/2]$, the exact value of which does not influence the asymptotic behavior. Moreover $\sin^2(x-\gamma^{-1}))$ will be of order γ^{-2} near $x = 0$ so the term with $\sin^2\theta$ in the numerator of Eq. 49 may be neglected in the limiting process. We now use that

$$\int_0^A \frac{\mathrm{d}x}{\left(a^2+x^2\right)^{1/2}} = \log|x+\sqrt{a^2+x^2}|_0^A$$

Examination of the leading terms shows that eventually

$$(\sigma_{zz}-\sigma_{yy})/G_0 \sim \frac{1}{2}\gamma^{-1}(C+\log\gamma) \tag{50}$$

where the constant C is included to indicate the order of the terms neglected.

The first normal stress difference is much easier to compute with the result

$$(\sigma_{xx}-\sigma_{yy})/G_0 \sim \frac{1}{2}\gamma \text{ for } \gamma \to \infty \tag{51}$$

The combined result is

$$-\frac{N_2}{N_1} \sim \gamma^{-2}(\log\gamma + C) \text{ for } \gamma \to \infty \tag{52}$$

Numerical computations show that $C \approx -0.6$.

References

Bird RB, Hassager O, Armstrong RC, Curtiss CF (1977) Dynamics of polymeric liquids: kinetic theory, vol 2, 1st edn. Wiley, New York

Bird RB, Armstrong RC, Hassager O (1987) Dynamics of polymeric liquids: fluid mechanics, vol 1. Wiley, New York

Blackwell RJ, McLeish TCB, Harlen OG (2000) Molecular drag-strain coupling in branched polymer melts. J Rheol 44:121–136

Currie PK (1982a) Constitutive equations for polymer melts predicted by the Doi-Edwards and Curtiss-Bird kinetic theory models. J Non-Newtonian Fluid Mech 11:53–68

Currie PK (1982b) Relationship between extensional and shear properties of polymer melts as predicted by the Doi–Edwards model. Polymer Preprints 23:6–7

Doi M (1995) Introduction to polymer physics. Oxford University Press, New York

Doi M, Edwards SF (1978) J Chem Soc Faraday Trans 2:74 1802

Doi M, Edwards SF (1986) The theory of polymer dynamics. Oxford University Press, New York

Fang J, Kröger M, Öttinger HC (2000) J Rheol 44:1293–1317

Hansen R, Skov AL, Hassager O (2008) Constitutive equation for polymer networks with phonon fluctuations. Phys Rev E 77:011802

Hassager O (1985) J Rheol 29:361

Lyhne A, Rasmussen HK, Hassager O (2009) Phys Rev Lett 102:138301

Marin JMR, Rasmussen HK (2009) Lagrangian finite-element method for the simulation of K-BKZ fluids with third order accuracy. J Non-Newtonian Fluid Mech 156:177–188

Marrucci G, Grizzuti N (1986) The Doi–Edwards model in slow flows. Predictions of the Weissenberg effect. J Non-Newtonian Fluid Mech 21:319–328

Maruucci G, Grizzutti N (1988) Gazz Chim Ital 118:179–185

Mead DW (2007) Development of the binary interaction theory for entangled polydisperse linear polymers. Rheol Acta 46:369–395

Mead DW, Yavich D, Leal LG (1995) The reptation model with segmental stretch II Steady flow properties. Rheol Acta 34:360–383

Mead DW, Larson RG, Doi M (1998) Macromolecules 31:7895–7914

Olley P (2005) A study of the quadratic molecular stress function constitutive model in simulation. J Non-Newtonian Fluid Mech 125:171

Olley P, Wagner MH (2006) A modification of the convective constraint release mechanism in the molecular stress function model giving enhanced vortex growth. J Non-Newtonian Fluid Mech 135:68–81

Osaki K, Kimura S, Kurata M (1981) J Polym Sci Pol Phys 19:517–527

Osaki K, Koji N, Kurata M (1982) Macromolecules 15:1068–1071

Pearson DS, Kiss Fetters LJ, Doi M (1989) J Rheol 33:517–535

Peters EAJF, van Heel APG, Hulsen MA, van den Brule BHAA (2000) Generalization of the deformation field method to simulate advanced reptation models in complex flow. J Rheol 44:811–829

Schieber J, Neergaard J, Gupta S (2003) J Rheol 47:213–233

Urakawa O, Takahashi M, Masuda T, Ebrahimi NG (1995) Damping functions and chain relaxation in uniaxial and biaxial extensions: comparison with the Doi–Edwards theory. Macromolecules 28:7196–7201

Wagner MH (1990) The nonlinear strain measure of polyisobutylene melt in general biaxial flow and its comparison to the Doi-Edwards model. Rheol Acta 29:594–603

Wapperom P, Keunings R (2001) Numerical simulation of branched polymer melts in transient complex flow using pom-pom models. J Non-Newtonian Fluid Mech 97:267–281

[P3]

J. Fluid Mech. (2009), *vol.* 636, *pp.* 371–396.
doi:10.1017/S002211200900799X

Osmotically driven pipe flows and their relation to sugar transport in plants

KÅRE H. JENSEN[1,2], EMMANUELLE RIO[1,3], RASMUS HANSEN[1], CHRISTOPHE CLANET[4] AND TOMAS BOHR[1]†

[1]Center for Fluid Dynamics, Department of Physics, Technical University of Denmark, Building 309, 2800 Kgs. Lyngby, Denmark

[2]Center for Fluid Dynamics, Department of Micro- and Nanotechnology, Technical University of Denmark, DTU Nanotech Building 345 East, 2800 Kgs. Lyngby, Denmark

[3]Laboratoire de Physique des Solides, Univ. Paris-Sud, CNRS, UMR 8502, F-91405 Orsay Cedex, France

[4]IRPHE, Universités d'Aix-Marseille, 49 Rue Frédéric Joliot-Curie BP 146, F-13384 Marseille Cedex 13, France

(Received 28 May 2008; revised 28 April 2009; accepted 28 April 2009)

In plants, osmotically driven flows are believed to be responsible for translocation of sugar in the pipe-like phloem cell network, spanning the entire length of the plant – the so-called Münch mechanism. In this paper, we present an experimental and theoretical study of transient osmotically driven flows through pipes with semi-permeable walls. Our aim is to understand the dynamics and structure of a 'sugar front', i.e. the transport and decay of a sudden loading of sugar in a water-filled pipe which is closed in both ends. In the limit of low axial resistance (valid in our experiments as well as in many cases in plants) we show that the equations of motion for the sugar concentration and the water velocity can be solved exactly by the method of characteristics, yielding the entire flow and concentration profile along the tube. The concentration front decays exponentially in agreement with the results of Eschrich, Evert & Young (*Planta* (*Berl.*), vol. 107, 1972, p. 279). In the opposite case of very narrow channels, we obtain an asymptotic solution for intermediate times showing a decay of the front velocity as $M^{-1/3}t^{-2/3}$ with time t and dimensionless number $M \sim \eta\kappa L^2 r^{-3}$ for tubes of length L, radius r, permeability κ and fluid viscosity η. The experiments (which are in the small M regime) are in good quantitative agreement with the theory. The applicability of our results to plants is discussed and it is shown that it is probable that the Münch mechanism can account only for the short distance transport of sugar in plants.

1. Introduction

The translocation of sugar in plants, which takes place in the phloem sieve tubes, is not well understood on the quantitative level. The current belief, called the pressure-flow hypothesis (Nobel 1999), is based on the pioneering work of Ernst Münch in the 1920s (Münch 1930). It states, that the motion in the phloem is purely passive, due to the osmotic pressures that build up relative to the neighbouring xylem in response to

† Email address for correspondence: tbohr@fysik.dtu.dk

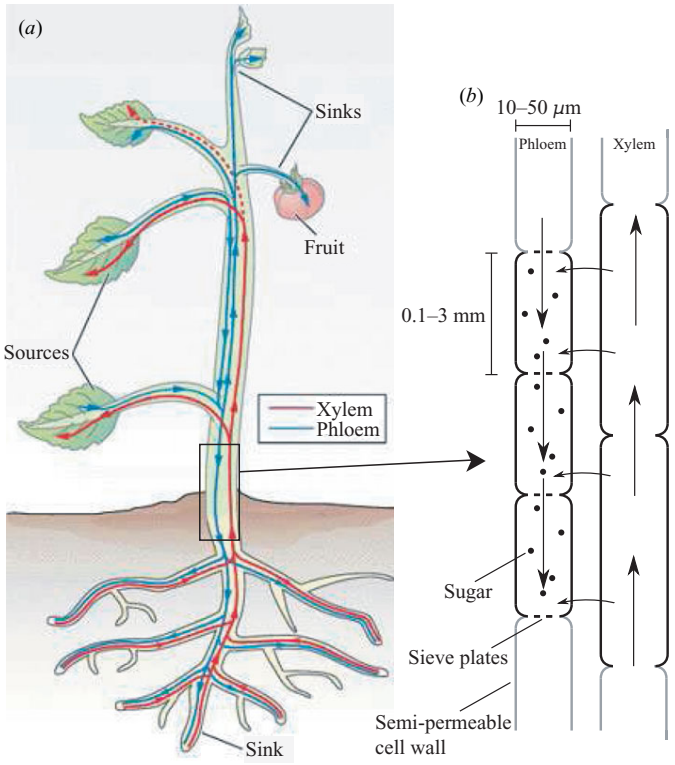

FIGURE 1. In plants, two separate pipe-like systems are responsible for the transport of water and sugar. The xylem conducts water from the roots to the shoot while the phloem conducts sugar and other nutrients from places of production to places of growth and storage. The mechanism believed to be responsible for sugar translocation in the phloem, called the Münch mechanism or the pressure-flow hypothesis (Nobel 1999), states the following: As sugar is produced via photosynthesis in sources it is actively loaded into the tubular phloem cells. As it enters the phloem, the chemical potential of the water inside is lowered compared to the surrounding tissue, thereby creating a net flux of water into the phloem cells. This influx of water in turn creates a bulk flow of sugar and water towards the sugar sink shown in (*b*), where active unloading takes place. As the sugar is removed, the chemical potential of the water inside the phloem is raised resulting in a flow of water out of the sieve element.

loading and unloading of sugar in different parts of the plant, as shown in figure 1. This mechanism is much more effective than diffusion, since the osmotic pressure differences caused by different sugar concentrations in the phloem create a bulk flow directed from large concentrations to small concentrations, in accordance with the basic need of the plant. Such flows are often called osmotically driven pressure flows (Thompson & Holbrook 2003), or osmotically driven volume flows (Eschrich, Evert & Young 1972).

To study the osmotically driven flows, Eschrich *et al.* (1972) conducted simple model experiments. Their set-up consisted of a semi-permeable membrane tube submerged in a water reservoir, modelling a phloem sieve element and the surrounding water-filled tissue. At one end of the tube a solution of sugar, water and dye was introduced to mimic the sudden loading of sugar into a phloem sieve element. In the case of the closed tube, they found that the sugar front velocity decayed exponentially in

time as it approached the far end of the tube. Also, they found the initial velocity of the sugar front to be proportional to concentration of the sugar solution. Through simple conservation arguments, they showed that for a flow driven according to the pressure-flow hypothesis, the velocity of the sugar front is given by

$$u_f = \frac{L}{t_0}\exp\left(-\frac{t}{t_0}\right) \quad \text{where} \quad t_0 = \frac{r}{2\kappa\Pi}, \tag{1.1}$$

where t is time, L is the length of the sieve element and r its radius, κ is the permeability of the membrane and Π is the osmotic pressure of the sugar solution. For dilute solutions, $\Pi \approx RTc$ (Landau & Lifshitz 1980), where R is the gas constant, T the absolute temperature and c the concentration in moles per volume. The conservation argument for (1.1) is the following: for incompressible flow in a wide rigid semi-permeable tube of length L imbedded in water, we imagine part of the tube initially filled with sugar solution and the rest with pure water. For a wide tube with slow flow, viscous effects and thus the pressure gradient along the tube is negligible and the pressure is simply equal to the osmotic pressure Π averaged over the tube, i.e. $RT\bar{c}$ where $\bar{c}$ is the constant average sugar concentration. The water (volume) flux through the part of the tube ahead of the sugar front x_f (where there is no osmosis) is $-2\pi r\kappa RT\bar{c}(L - x_f)$, where κ is the permeability of the tube and the flow is negative since water flows out. This will be equal to the rate of change of volume ahead of x_f and thus, due to incompressibility, is equal to $-\pi r^2 \mathrm{d}x_f/\mathrm{d}t$. Putting these two expressions together we get

$$\frac{\mathrm{d}x_f}{\mathrm{d}t} = \frac{2L_p RT\bar{c}}{r}(L - x_f) = \frac{1}{t_0}(L - x_f) \tag{1.2}$$

leading to $u_f = \mathrm{d}x_f/\mathrm{d}t$ given by (1.1).

In the experiments performed by Eschrich *et al.* (1972) good qualitative agreement with (1.1) was obtained, but on the quantitative level the agreement was rather poor. We thus chose to perform independent experiments along the same lines. Eschrich *et al.* (1972) used dye to track the sugar, and in one of our set-ups we can check this method by directly following the sugar without using dye. Also, we make independent measurements of the membrane properties, which then allow detailed comparison with the predictions showing good quantitative agreement.

Simultaneously with the experiments, we develop the theory for osmotic flows. The above derivation of the front propagation is simplified by the lack of viscosity and diffusion and, indeed, by the very assumption that a well-defined sugar front exists. To go beyond this we must use the coupled equations for the velocity and concentration fields as they vary along the tubes and in time. Here we follow the footsteps of a large number of authors, as discussed later. Our main contribution is the analysis of the decay of an initially localized sugar concentration in a channel closed in both ends described by (4.9) and (4.10). Here we point out that the main dimensionless number (termed as *Münch number*) can be chosen as

$$M = \frac{16\eta L^2\kappa}{r^3}, \tag{1.3}$$

where η is the fluid viscosity. We show how to simplify the equations and obtain exact solutions in the regimes $M \ll 1$ (the regime of the experiments in this paper and of those of Eschrich *et al.*) and asymptotic solutions for $M \gg 1$. Both regimes are found in plants and we propose an effective way for numerical integration of the equations in the general case using Green's functions. In the regime $M \ll 1$ the solubility of the

Quantity	Magnitude	Reference
Radius (μm)	4.5 (Fava bean), 4 (Winter squash), 6–25	Knoblauch & van Bel (1998), Taiz & Zeiger (2002), Nobel (1999)
Length (mm)	0.09 (Fava bean), 0.1–3	Knoblauch & van Bel (1998), Nobel (1999)
Flow velocity ($m\,h^{-1}$)	0.5–1, 0.2–2	Knoblauch & van Bel (1998), Nobel (1999)
Elastic modulus (MPa)	17, 5.6–7.4 (Ash)	Thompson & Holbrook (2003*a*), Niklas (1992)
Permeability ($10^{-11}\,m\,s^{-1}\,Pa^{-1}$)	5,1.1 (Zitella translucence)	Thompson & Holbrook (2003*a*), Eschrich *et al.* (1972)
Sucrose concentration (M)]	0.3–0.9	Taiz & Zeiger (2002)

TABLE 1. Characteristic properties of phloem sieve elements.

equations is shown by mapping them to a damped Burgers equation (5.6), which can be solved by the method of characteristics. An analogous relation was pointed out earlier by Frisch (1976), but for a different boundary condition (open in one end) where the damping term disappears. Some results for $M \ll 1$ were also given by Weir (1981), but the lack of generality of his approach to the time-dependent problem makes his results hard to extend.

In table 1 we show characteristic data for single sieve elements, which build up the phloem conducts in plants. If one naively applies these results to the flow inside such sieve elements, taking $L = 1\,\mathrm{mm}$, $r = 10\,\mu\mathrm{m}$, $\kappa = 10^{-11}\,\mathrm{m\,s^{-1}\ Pa^{-1}}$ and concentration $\bar{c} = 0.5\,\mathrm{M}$, one gets a characteristic velocity from (1.1) of $9\,\mathrm{m\,h^{-1}}$, almost an order of magnitude larger than the range of velocities given in the table. Here one has to remember that the characteristic velocity from (1.1) is valid for a *transient* flow caused by an initial sudden sugar loading, whereas the velocities quoted in the table are characteristic for the normal steady-state operation of the plants. For large distances (e.g. those occurring in tall trees), the viscous effects embodied in (1.3) become large. Thus the value of M for the single sieve element considered above is $M \approx 1.6 \times 10^{-4}$ whereas the value for a phloem tube spanning a distance of 10 m would be greater by a factor 10^8, i.e. $M \approx 1.6 \times 10^4$ (see also table 3 for characteristic values for M). In this regime (1.1) is no longer valid and, in fact, as seen in § 5.2 (5.46), the characteristic velocity will be reduced by a factor $M^{-1/3}$, now making it an order of magnitude *smaller* than the velocities quoted in the table. This seems to indicate that large distance transport in trees cannot rely solely on the Münch mechanism and indeed the sieve elements are living cells and active transport may play a key role (see, e.g. Taiz & Zeiger 2002). For future studies in this direction it is important to be able to separate these effects clearly and thus to understand the passive osmotic component as clearly and simply as possible, which is the aim of the present paper.

The layout of the paper is as follows: §§ 2 and 3 describe our experimental set-ups and the experimental results obtained. In § 4, the flow equations are developed and in § 5 we present solutions for the cases $M \ll 1$ and $M \gg 1$. Finally, § 6 contains a detailed comparison between theory and experiments. After the conclusions (§ 7), two appendices follow. Appendix A provides information about the experimental materials used and appendix B discusses the numerical methods (based on Green's functions) used for solving the flow equations in the general case.

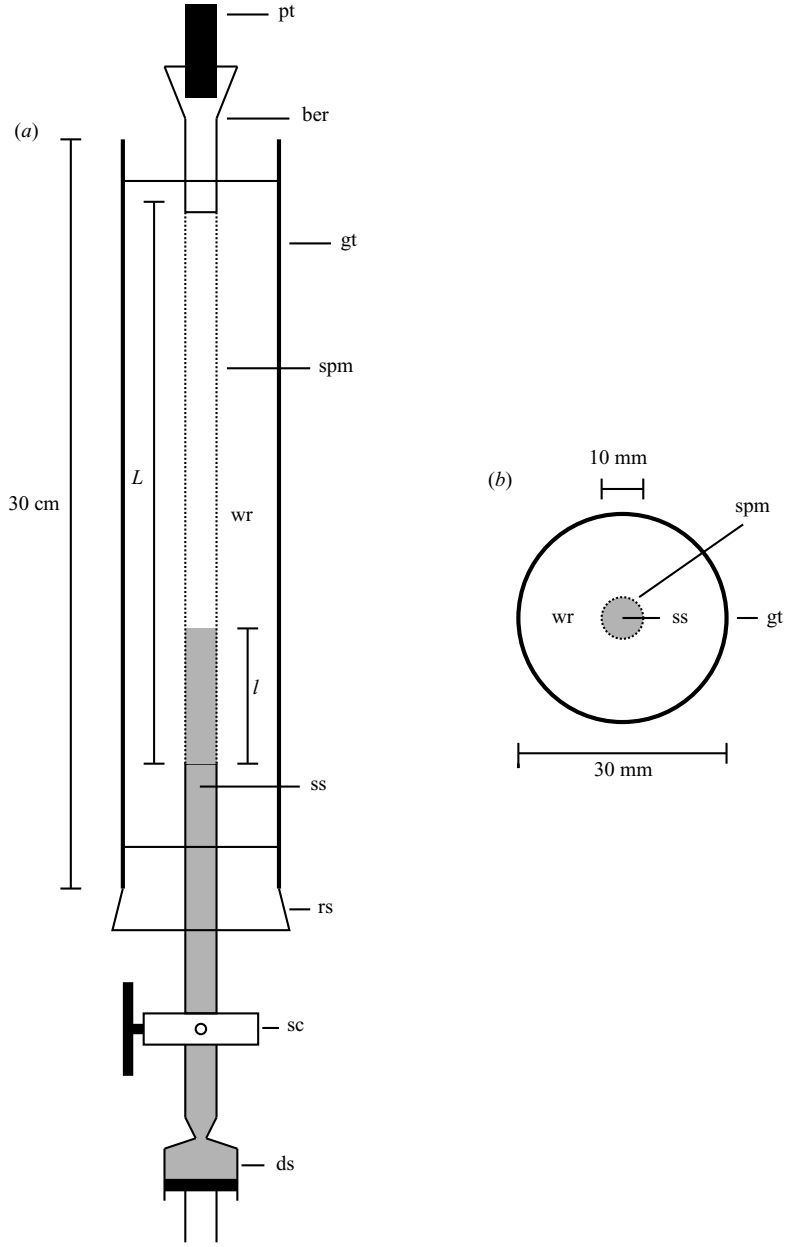

FIGURE 2. Set-up I used to observe the movement of a sugar–dye solution (ss) inside a semi-permeable membrane tube (spm). L: length of membrane tube; l: initial sugar front height; ds: disposable syringe; gt: glass tube; rs: rubber stopper; sc: stopcock; wr: water reservoir; bc: brass cylinder; pt: pressure transducer.

2. First experimental set-up

2.1. *Set-up and methods*

Set-up I is presented in figure 2. It is based on the design by Eschrich *et al.* with the addition of a pressure transducer that allows us to measure the gauge pressure

	1	2	3	4	5
Mean sugar concentration, $\bar{c}$ (mM)	1.5 ± 0.3	2.10 ± 0.03	2.4 ± 0.2	4.2 ± 0.7	6.8 ± 0.1
Osmotic pressure, Π (bar)	0.14 ± 0.02	0.15 ± 0.01	0.31 ± 0.03	0.39 ± 0.01	0.68 ± 0.02
Membrane tube length, L (cm)	28.5	20.8	28.5	28.5	20.6
Initial front height, l (cm)	4.9	3.7	6.6	6.5	4.8

TABLE 2. Data for the experimental runs shown in figure 3.

(which is what we from now on will refer to as 'pressure') inside the membrane tube continuously. More precisely, it consisted of a 30 cm long, 30 mm wide glass tube in which a semi-permeable membrane tube of equal length and a diameter of 10 mm was inserted. At one end, the membrane tube was fitted over a glass stopcock equipped with a rubber stopper. On the other end, the membrane tube was fitted over a brass cylinder equipped with a holder to accommodate a pressure transducer for measuring the pressure inside the membrane tube.

After filling the 30 mm wide glass tube with water, water was pressed into the semi-permeable tube with a syringe. Care was taken so that no air bubbles were stuck inside the tube. For introducing the sugar solution into the tube, a syringe was filled with the solution and then attached to the lower end of the stopcock which was kept closed. After fitting the syringe, the stopcock was opened and the syringe piston was very slowly pressed in, until a suitable part of the tube had been filled with the solution. Care was also taken to avoid any mixing between the sugar solution and the water already present in the semi-permeable tube. The physical characteristics of the membranes and of the sugar we used are discussed in appendix A. To track the movement of the sugar solution it was mixed with a red dye and data was recorded by taking pictures of the membrane tube at intervals of 15 min using a digital camera.

2.2. *Experimental results obtained with set-up I*

An example of a set of data is shown in figure 3. In figure 3(a) are the raw images, which after processing give figure 3(b) showing the position of the sugar front, x_f, as a function of time. The error bars on x_f are estimated to be ± 1 mm, but are too small to be seen. Finally, figure 3(c) shows the pressure inside the tube as a function of time. At first, a linear motion of the front is observed with a front velocity of ~ 1 cm h^{-1}. This is then followed by a decrease in the front velocity as the front approaches the end of the tube. The pressure is seen to rise rapidly during the first hour before settling to a constant value, indicated by the dashed line. This constant value is taken to be the osmotic pressure Π of the sugar solution. Looking at figure 3(a), one observes that diffusion has the effect of dispersing the front slightly as time passes. Below the front, the concentration seems to be uniform throughout the cross-section of the tube, and there is no indication of large boundary layers forming near the membrane walls.

Similar experiments with different sugar concentrations were made and a plot of the results can be seen in figure 3(d,e). The experimental conditions for the five different sets of experiments are given in table 2. Qualitatively the motion of the front and the pressure increase follows the same pattern. One notices that the speed with which the fronts move is related to the mean sugar concentration inside the membrane tube, with the high-concentration solutions moving faster than the low-concentration ones.

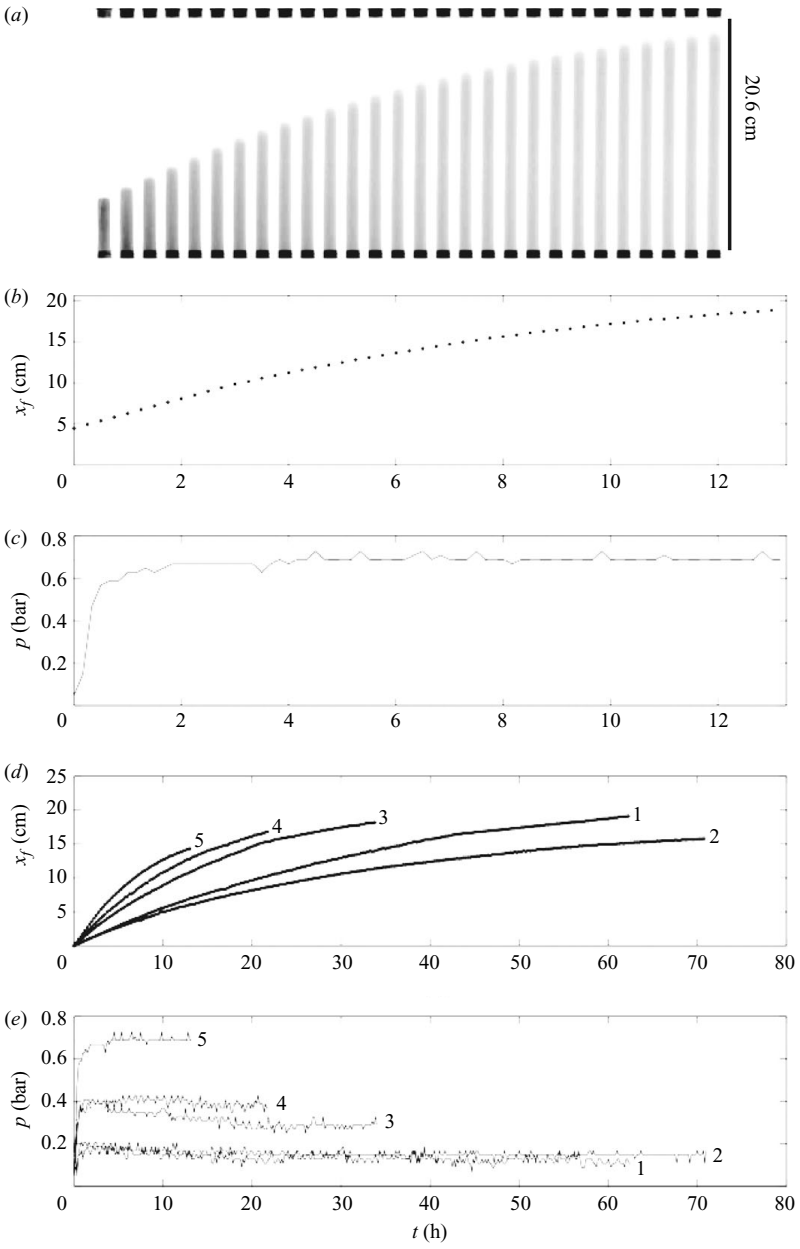

FIGURE 3. Experimental results from set-up I. (*a*) Time series of pictures taken in experiment 5. Time increases from left to right in steps of 30 min. See details of the sugar solutions used in table 2. (*b*) Plot of the front position versus time obtained from the images above. (*c*) Plot of the gauge pressure inside the tube versus time. The dashed line is the osmotic pressure of the solution, taken to be the average value of the pressure from $t = 2$ h until the end of the experiment. (*d*) Plots of the sugar front position versus time for different sugar concentrations, as indicated in table 2. (*e*) Plots of the pressure inside the membrane tube for different sugar concentrations.

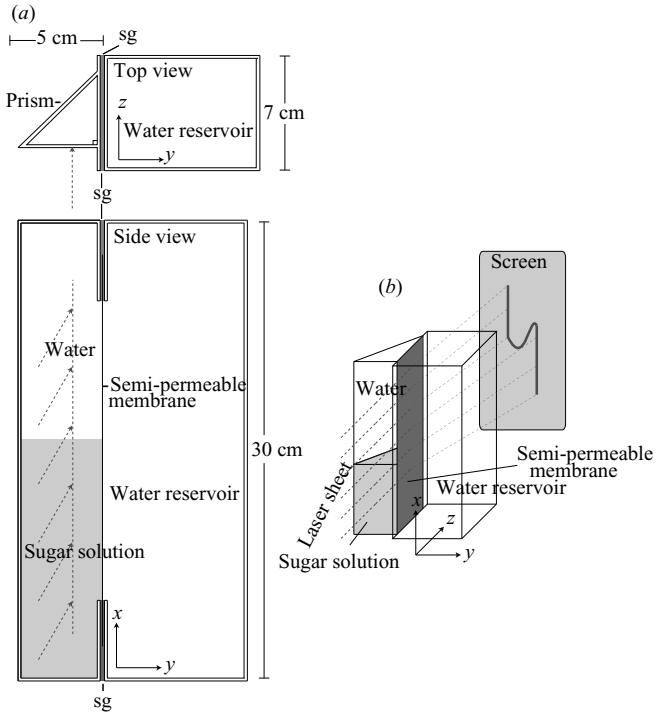

FIGURE 4. Set-up II dedicated to the tracking of the sugar front via index of refraction changes. It consists of a hollow isosceles glass prism and a Plexiglas cuboid in osmotic contact through a membrane. A pressure transducer was attached to the top of the glass prism to measure the pressure inside.

The reason why 2 is moving slower than 1 is that experiment 2 was conducted in a slightly shorter membrane tube than the one used in experiment 1, thereby decreasing the characteristic velocity as we shall see later.

3. Second experimental set-up

3.1. *Set-up and methods*

Set-up II is presented in figure 4. This set-up allows us to track the real front location, without the use of colorant, directly via the variation of the index of refraction. It consisted of a hollow isosceles glass prism and a Plexiglas cuboid in osmotic contact through a membrane. To track the time evolution of the sugar front inside the prism, we used the refraction of a laser sheet passing through it. The laser sheet was generated by shining a laser beam, generated by a Melles Griot 3.1 mW laser, through a glass rod. When passing through the prism, light would deviate depending on the local index of refraction, producing a typical S shape as shown in figure 4. The index of refraction varies linearly with sugar concentration and thus by looking at the refracted laser sheet projected onto a screen, we were able to reconstruct the concentration profile inside the prism. A camera recorded images of the screen at regular intervals to track the moving concentration profile.

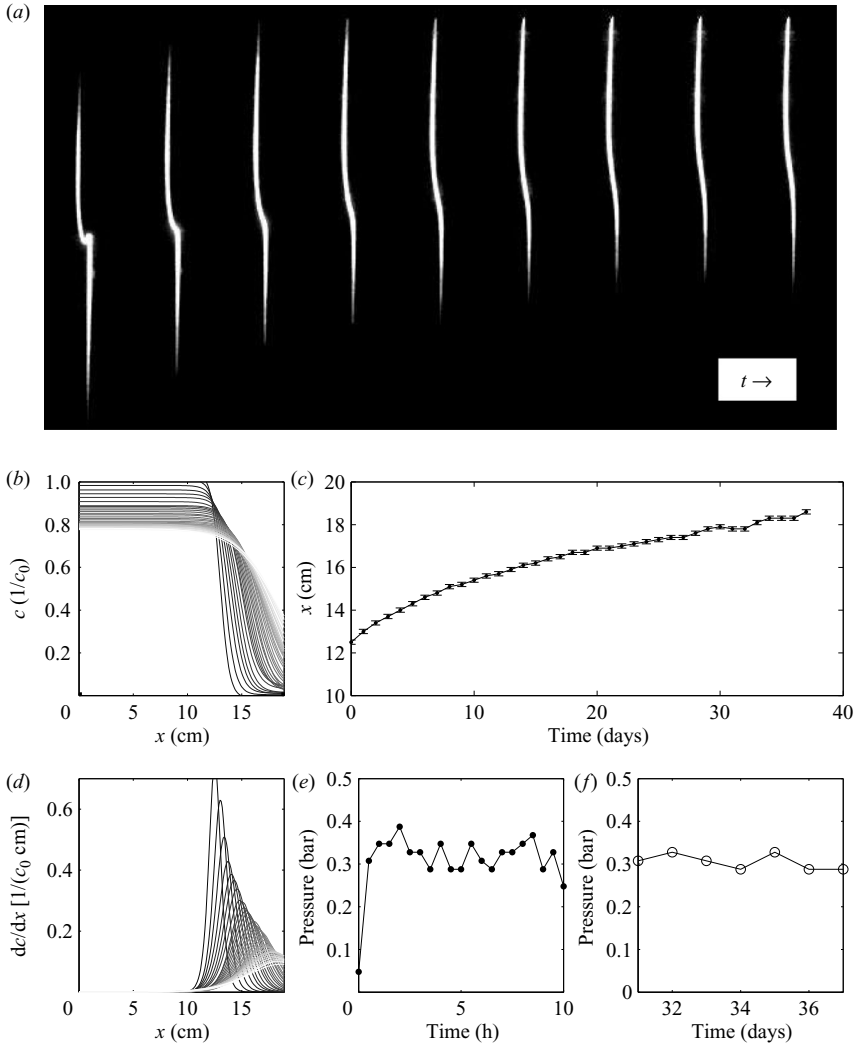

FIGURE 5. Results from set-up II. In (*a*) the raw data images are shown. In (*b*) the concentration profile extracted from (*a*) is shown. (*c*) shows the front position extracted from (*b*) by finding the maximum of the concentration gradient, shown in (*d*). Finally, (*e*, *f*) show the pressure inside the prism.

3.2. *Experimental results obtained with set-up II*

3.2.1. *Effect of osmosis*

Figure 5 shows the data collected using set-up II. In figure 5(*a*), a time series of pictures is depicted showing the refracted laser-light projected onto a screen, the time gap between each image being 1 day. Comparing the upper and lower parts of each picture, one generally observes a deflection to the right at the bottom, corresponding to a high sugar concentration at the bottom of the prism. In the intermediate region one sees a dip in the refracted light, corresponding to a strong concentration gradient. The dip gradually flattens while it advances upwards, representing a sugar front which advances while it broadens. This process can be seen directly in figure 5(*b*),

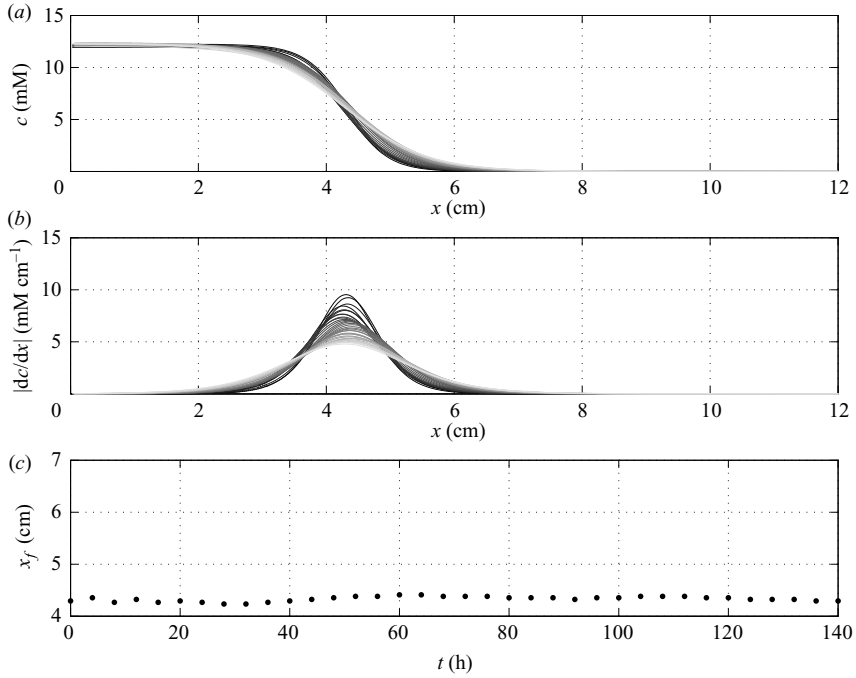

FIGURE 6. Results from a control experiment with set-up II, where concentration varies only due to diffusion. (*a*) Time evolution of the concentration profile, (*b*) time evolution of the profile of concentration gradient and (*c*) time evolution of the sugar front location.

which shows the time evolution of the sugar concentration obtained from the images. Starting from a steep concentration profile, we see that the front moves upwards while it flattens. In figure 5(*d*) the time evolution of the concentration gradient is depicted, clearly showing a peak which broadens while it moves forward. Finally, in figure 5(*e*, *f*), the position of the sugar front and the pressure inside the prism is plotted as a function of time. The error bars on x_f are ± 1 mm, as discussed below.

3.2.2. *Effect of diffusion*

To study the effect of diffusion on the dynamics of the sugar front separately, an experiment was made with set-up II, in which the water reservoir was not filled. The experiment was then conducted in the usual way, and the motion of the front was recorded. The results of this are shown in figure 6. Starting from a steep concentration gradient, we observe that the front flattens but otherwise does not move much.

Comparing figures 5 and 6 we observe, that while the front moves 2 cm due to osmosis in 6 days, it does not seem to move at all in 6 days due to diffusion. Thus, while diffusion has a flattening effect, it plays little role in the forward motion of the front.

Since the front did not move due to diffusion, the fluctuations in the front position seen in figure 6(*c*) gives a measure of the uncertainty of a single measurement of the front position. Taking the standard deviation of the fluctuations gives an uncertainty of ± 1 mm, shown as error bars in figure 5(*c*).

More details on this second experiment can be found in Jensen (2007).

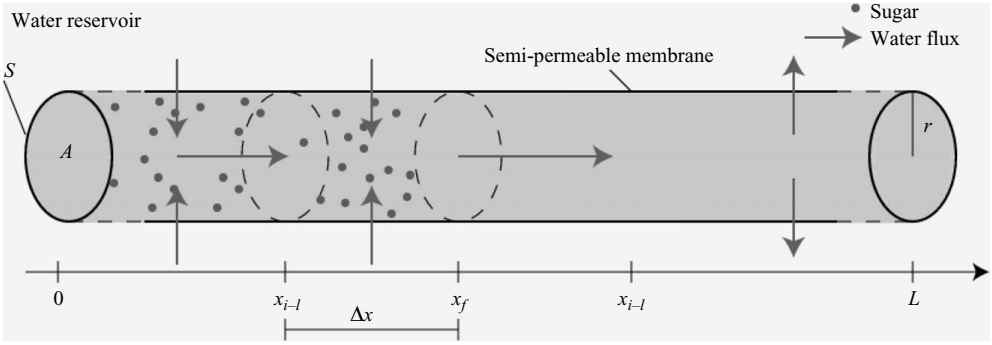

FIGURE 7. Sketch of the tube.

4. Theoretical analysis

4.1. *Front propagation via flow equations*

The equations of motion for osmotically driven flows have been derived and analysed thoroughly several times in the literature (Weir 1981) and have been studied carefully numerically (Henton 2002; Thompson & Holbrook 2003*a*, *b*). For the sake of completeness, we shall include a short derivation of these.

We consider a tube of length L and radius r, as shown in figure 7. The tube has a constant cross-section of area $A = \pi r^2$ and circumference $S = 2\pi r$ and its walls are made of a semi-permeable membrane with permeability κ. Inside the tube is a solution of sugar in water with concentration $c(x) = c(x, t)$. Throughout this paper, we study the transient dynamics generated by an asymmetrical initial concentration distribution, where the sugar is initially localized to one end of the tube with a concentration level c_0. The tube is surrounded by a water reservoir, modelling the water surrounding the membrane tube in set-up I.

We shall assume that $L \gg r$ and that the radial component of the flow velocity inside the tube is much smaller than the axial component, as is indeed the case in the experiments. With these assumptions, we will model the flow in the spirit of lubrication theory and consider only a single average axial velocity component $u(x, t)$. Also, we will assume that the concentration c is independent of the radial position ρ an assumption that can be verified experimentally in set-up II.

Let us now consider the equation for volume conservation by looking at a small section of the tube between x_{i-1} and x_i. The volume flux into the section due to advection is

$$A(u_{i-1} - u_i), \tag{4.1}$$

where the axial flow velocities are taken to be u_{i-1} and u_i at x_{i-1} and x_i, respectively. The volume flux inwards across the membrane due to osmosis (Schultz 1980) is

$$S\Delta x\kappa(RTc(x, t) - p(x, t)), \tag{4.2}$$

where p is the local difference of pressure across the membrane and c is the local concentration. For clarity we use the van't Hoff value $\Pi = RTc$ for the osmotic pressure, which is valid only for dilute (ideal) solutions. In appendix A.3, we show that the linear relation between Π and c is verified experimentally as $\Pi = (0.1 \pm 0.01\,\text{bar mM}^{-1})c$. Assuming conservation of volume, we get

$$A(u_{i-1} - u_i) + S\Delta x\kappa(RTc - p) = 0. \tag{4.3}$$

Letting $\Delta x \to 0$ and using that the cross-section to perimeter ratio reduces to $r/2$, this becomes

$$\frac{r}{2}\frac{\partial u}{\partial x} = \kappa(RTc - p). \tag{4.4}$$

For these very slow and slowly varying flows, the time dependence of the Navier–Stokes equation can be neglected and the velocity field is determined by the instantaneous pressure gradient through the Poiseuille or Darcy relation (for a circular tube)

$$u = -\frac{r^2}{8\eta}\frac{\partial p}{\partial x}, \tag{4.5}$$

where η is the dynamic viscosity of the solution, typically $\sim 1.5 \times 10^{-3}$ Pa s in our experiments.

Differentiating (4.4) with respect to x and inserting the result from (4.5) we get for the conservation of water that

$$RT\frac{\partial c}{\partial x} = \frac{r}{2\kappa}\frac{\partial^2 u}{\partial x^2} - \frac{8\eta}{r^2}u. \tag{4.6}$$

The final equation expresses the conservation of sugar advected with velocity u and diffusing with molecular diffusivity D

$$\frac{\partial c}{\partial t} + \frac{\partial uc}{\partial x} = D\frac{\partial^2 c}{\partial x^2}. \tag{4.7}$$

The set of equations (4.6) and (4.7) is equivalent to those of Thompson & Holbrook (2003*b*) except for the fact that we have removed the pressure by substitution, and that we do not consider elastic deformations of the tube.

4.1.1. *Non-dimensionalization of the flow equations*

To non-dimensionalize (4.6) and (4.7), we introduce the following scaling

$$c = c_0 C, \qquad u = u_0 U, \qquad x = LX, \qquad t = t_0 \tau,$$

L has been chosen such that the spatial domain is now of the unit interval $X \in [0, 1]$, $u_0 = L/t_0$ and c_0 is the initial concentration level in one end of the tube. Choosing further

$$t_0 = \frac{r}{2\kappa RTc_0}, \quad M = \frac{16\eta L^2\kappa}{r^3} \quad \text{and} \quad \bar{D} = \frac{D}{u_0 L} = \frac{Dr}{2RTc_0L^2\kappa}, \tag{4.8}$$

and inserting in (4.6) and (4.7), we get the non-dimensional flow equations

$$\frac{\partial^2 U}{\partial X^2} - MU = \frac{\partial C}{\partial X}, \tag{4.9}$$

$$\frac{\partial C}{\partial \tau} + \frac{\partial UC}{\partial X} = \bar{D}\frac{\partial^2 C}{\partial X^2}. \tag{4.10}$$

The parameter M corresponds to the ratio of axial to membrane flow resistance, which we shall refer to as the *Münch number*. This is identical to the parameter $\hat{F}$ in Thompson & Holbrook (2003*b*). The second parameter $\bar{D}$ is the Peclet number. Thus, the longer the tube the less important the diffusion becomes and the more important the pressure gradient due to viscous effects becomes.

Values of the parameters M and $\bar{D}$ in different situations can be seen in table 3. The typical magnitude of the parameters M and $\bar{D}$ in plants are found from the

	M	$\bar{D}$
Set-up I	2×10^{-8}	6×10^{-5}
Set-up II	10^{-9}	2×10^{-2}
Single sieve element ($L = 1$ mm)	5×10^{-4}	5×10^{-4}
Leaf ($L = 1$ cm)	5×10^{-2}	5×10^{-5}
Branch ($L = 1$ m)	5×10^{2}	5×10^{-7}
Small tree ($L = 10$ m)	5×10^{4}	5×10^{-8}

TABLE 3. Values of the parameters M and $\bar{D}$ in various situations.

following values (also given in table 3):

$$r = 10\,\mu\text{m}, \quad \eta = 1.5 \times 10^{-3}\,\text{Pa s}, \quad u_0 = 2\,\text{m h}^{-1}, \quad \kappa = 2 \times 10^{-11}\,\text{m (Pa s)}^{-1}.$$

We observe, that M and $\bar{D}$ are small in both experiments, and that for short distance transport in plants this is also the case. However, over length scales comparable to a branch ($L = 1$ m) or a small tree ($L = 10$ m) M is large, so in this case the pressure gradient is not negligible.

When deriving the equations for osmotically driven flows, we have assumed that the concentration inside the tube was a function of x and t only. However, the real concentration inside the tube will also depend on the radial position ρ in the form of a concentration boundary layer near the membrane, in the literature called an *unstirred layer* (Pedley 1983). Close to the membrane, the concentration c_m is lowered compared to the bulk value c_b because sugar is advected away from the membrane by the influx of water. This, in turn, results in a lower influx of water, ultimately causing the axial flow inside the tube to be slower than expected. In our experiments we see no signs of such boundary layers and apparently their width and their effect on the bulk flow are very small.

5. Solutions of the flow equations

We will now analyse (4.9) and (4.10). We will show that they can be solved quite generally for $M = \bar{D} = 0$ by the method of characteristics. For an arbitrary initial condition, this method will generally yield an implicit solution.

For arbitrary values of M and $\bar{D}$, we cannot solve the equations of motion analytically and thus have to incorporate numerical methods. This topic has been the focus of much work both in the steady-state case (Thompson & Holbrook 2003*a*) and in the transient case (Henton 2002). However, no formulation fully exploiting the partially linear character of the equations capable of handling all different boundary conditions has so far been presented. Therefore, we show that using Green's functions, the equations of motion can be transformed into a single integro-differential equation, which can be solved using standard numerical methods with very high precision. This technical numerical part is detailed in appendix B.

5.1. *Results for small Münch number*

In the limit $M = \bar{D} = 0$ the equations become

$$\frac{\partial^2 U}{\partial X^2} = \frac{\partial C}{\partial X}, \tag{5.1}$$

$$\frac{\partial C}{\partial \tau} + \frac{\partial UC}{\partial X} = 0. \tag{5.2}$$

By integrating (5.1) with respect to X, we get

$$\frac{\partial U}{\partial X} = C + F(\tau). \tag{5.3}$$

If we choose $U(0) = U(1) = 0$, $F(\tau)$ becomes

$$F(\tau) = -\int_0^1 C \, \mathrm{d}X \equiv -\bar{C}(\tau). \tag{5.4}$$

Using (5.3) in (5.2) gives

$$\frac{\partial}{\partial X}\left[\frac{\partial U}{\partial \tau} + U\left(\frac{\partial U}{\partial X} + \bar{C}\right)\right] = -\frac{\mathrm{d}\bar{C}}{\mathrm{d}\tau} = 0, \tag{5.5}$$

where the last equality follows from integrating X from 0 to 1, observing that all terms in the square bracket vanish at the end points due to the boundary condition $u(X=0,\tau) = u(X=1,\tau) = 0$. Thus $\bar{C}$ is a constant in time since the tube is closed. Integrating with respect to X and using the boundary conditions on U, this becomes

$$\frac{\partial U}{\partial \tau} + U\frac{\partial U}{\partial X} = -\bar{C}U. \tag{5.6}$$

Equation (5.6) is a damped Burgers equation (Gurbatov, Malakhov & Saichev 1991), which can be solved using Riemann's method of characteristics. The characteristic equations are

$$\frac{\mathrm{d}U}{\mathrm{d}\tau} = -\bar{C}U \tag{5.7}$$

$$\frac{\mathrm{d}X}{\mathrm{d}\tau} = U. \tag{5.8}$$

Equation (5.7) has the solution

$$U = U_0(\xi)\exp(-\bar{C}\tau), \tag{5.9}$$

where the parametrization $\xi(X,\tau)$ of the initial velocity has to be found from

$$X = \xi + \frac{1}{\bar{C}}U_0(\xi)(1 - \exp(-\bar{C}\tau)), \tag{5.10}$$

where $\xi = X$ at $\tau = 0$.

5.1.1. *Exact solutions for simple initial conditions*

An experimental condition close to that of our experiments is to use a Heaviside step function as initial condition on C, making C initially constant in some interval $[0, \lambda]$

$$C(X, \tau = 0) = C_I H(\lambda - X) = \begin{cases} C_I & \text{for} \quad 0 \leqslant X \leqslant \lambda. \\ 0 & \text{for} \quad \lambda < X \leqslant 1. \end{cases} \tag{5.11}$$

Equation (5.3) now enables us to find the initial condition on the velocity

$$U(X, \tau = 0) = \int_0^X (C(X',0) - \bar{C}) \, \mathrm{d}X' = \int_0^X (C(X',0) - \lambda C_I) \, \mathrm{d}X' \tag{5.12}$$

$$= \begin{cases} (C_I - \bar{C})X & \text{for} \quad 0 \leqslant X \leqslant \lambda. \\ \bar{C}(1 - X) & \text{for} \quad \lambda < X \leqslant 1. \end{cases} \tag{5.13}$$

From (5.13), we have

$$U_0(\xi) = \begin{cases} (C_I - \bar{C})\xi & \text{for} \quad 0 \leqslant \xi \leqslant \lambda. \\ \bar{C}(1-\xi) & \text{for} \quad \lambda < \xi \leqslant 1. \end{cases} \tag{5.14}$$

Then, solving for $\xi(X, \tau)$ in (5.10) gives

$$\xi(X,\tau) = \begin{cases} \dfrac{X}{1 + (1/\lambda)(1-\lambda)(1-\exp(-\bar{C}\tau)} & \text{for} \quad X \in I_1, \\ \dfrac{X - 1 + \exp(-\bar{C}\tau)}{\exp(-\bar{C}\tau)} & \text{for} \quad X \in I_2, \end{cases} \tag{5.15}$$

where the intervals I_1 and I_2 are defined by

$$I_1 = [0, 1 - (1-\lambda)\exp(-\bar{C}\tau)], \tag{5.16}$$

$$I_2 = [1 - (1-\lambda)\exp(-\bar{C}\tau), 1]. \tag{5.17}$$

Finally, $U(X, \tau)$ is calculated from (5.9)

$$U(X,\tau) = \begin{cases} \dfrac{(C_I - \bar{C})\exp(-\bar{C}\tau)X}{(1/\lambda)(1-\lambda)(1-\exp(-\bar{C}\tau))} & \text{for} \quad X \in I_1, \\ \bar{C}(1-X) & \text{for} \quad X \in I_2, \end{cases} \tag{5.18}$$

which is equivalent to the result obtained by Weir (1981). The solution is plotted in figure 8(a, b). We can now calculate the instantaneous sugar front position X_f and velocity U_f using the right boundary of I_1 from (5.16)

$$X_f(\tau) = 1 - (1-\lambda)\exp(-\bar{C}\tau), \tag{5.19}$$

$$U_f(\tau) = \frac{\mathrm{d}X_f}{\mathrm{d}\tau} = \bar{C}(1-\lambda)\exp(-\bar{C}\tau). \tag{5.20}$$

Similarly, $C(X, \tau)$ is given by

$$C(X,\tau) = \frac{\bar{C}}{1 - (1-\lambda)\exp(-\bar{C}\tau)} H(X_f - X). \tag{5.21}$$

Going back to dimensional variables, (5.19) and (5.20) become

$$x_f(t) = L - (L-l)\exp\left(-\frac{t}{t_0}\right) \quad \text{and} \tag{5.22}$$

$$u_f(t) = \frac{L}{t_0}\exp\left(-\frac{t}{t_0}\right), \tag{5.23}$$

where L is the length of the membrane tube, l is the initial front position and the decay time t_0 is in accordance with the simple argument given in § 1.

As noted earlier we can use the method of characteristics on arbitrary initial conditions, including the more realistic case, where the initial jump in concentration is replaced by a continuous variation, say, a linear decrease from C_I to 0 taking place between λ_1 and λ_2, i.e.

$$C(X, \tau = 0) = \begin{cases} C_I & \text{for} \quad 0 \leqslant X \leqslant \lambda_1. \\ C_I \dfrac{\lambda_2 - X}{\lambda_2 - \lambda_1} & \text{for} \quad \lambda_1 \leqslant X \leqslant \lambda_2. \\ 0 & \text{for} \quad \lambda_2 < X \leqslant 1. \end{cases} \tag{5.24}$$

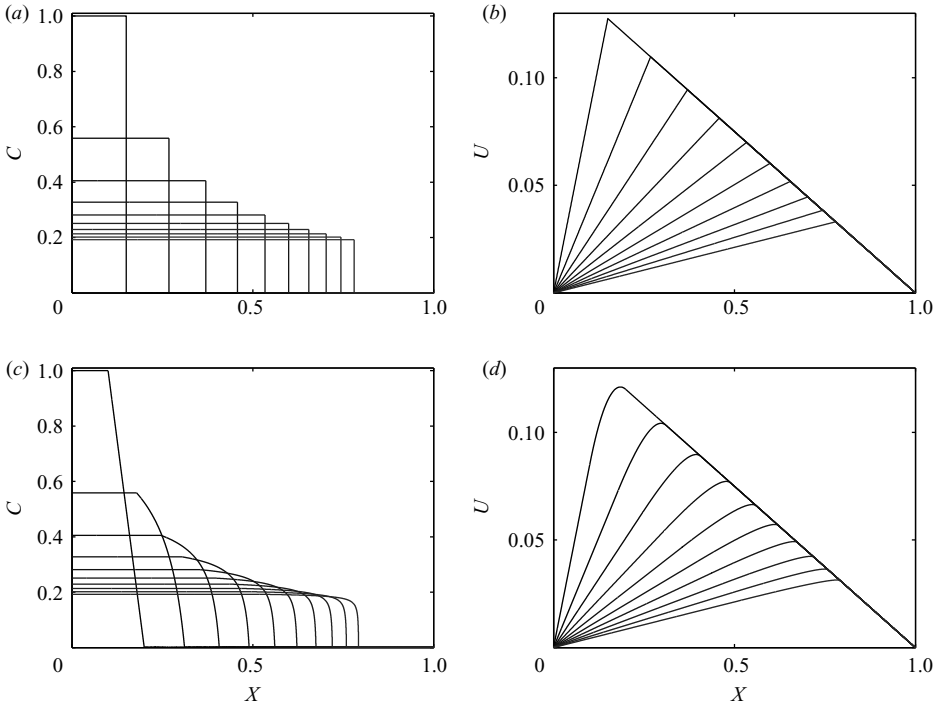

FIGURE 8. (a, b) Plot of the analytical solution for a piecewise constant initial concentration. $\lambda = 0.1$, $C_I = 1$ and $\bar{C} = 0.1$. (c, d) Plot of the analytical solution for a piecewise linear initial concentration. $\lambda_1 = 0.05$, $\lambda_2 = 0.15$, $C_I = 1$ and $\bar{C} = 0.1$. Time increases from black to gray in steps of one unit of time.

Using (5.3) yields the initial velocity

$$U(X, \tau = 0) = \begin{cases} (C_I - \bar{C})X & \text{for} \quad 0 \leqslant X \leqslant \lambda_1, \\ A_1 X^2 + B_1 X + C_1 & \text{for} \quad \lambda_1 \leqslant X \leqslant \lambda_2, \\ \bar{C}(1 - X) & \text{for} \quad \lambda_2 < X \leqslant 1, \end{cases} \tag{5.25}$$

where $\bar{C} = C_I(\lambda_1 + \lambda_2)/2$, and the constants are given by

$$A_1 = -\frac{C_I}{2(\lambda_2 - \lambda_1)}, \quad B_1 = \frac{C_I \lambda_2}{\lambda_2 - \lambda_1} - \bar{C}, \quad C_1 = C_I \lambda_1 + \frac{C_I}{\lambda_2 - \lambda_1}\left(\lambda_1 \lambda_2 + \lambda_1^2/2\right). \tag{5.26}$$

Finding $\xi(X, \tau)$ from (5.10) now gives

$$\xi(X, \tau) = \begin{cases} \dfrac{X}{1 + (1/\lambda)(1 - \lambda)(1 - \exp(-\bar{C}\tau)} & \text{for} \quad X \in I_1, \\ A_2 \xi_2^2 + B_2 \xi_2^2 + C_2 & \text{for} \quad X \in I_2, \\ \dfrac{X - 1 + \exp(-\bar{C}\tau)}{\exp(-\bar{C}\tau)} & \text{for} \quad X \in I_3, \end{cases} \tag{5.27}$$

where

$$A_2 = \frac{A_1}{\bar{C}}(1 - \exp(-\bar{C}\tau)), \quad B_2 = 1 + \frac{B_1}{\bar{C}}(1 - \exp(-\bar{C}\tau)), \quad C_2 = \frac{C_1}{\bar{C}}(1 - \exp(-\bar{C}\tau)). \tag{5.28}$$

Here

$$\xi_2 = \frac{-B_2 + \sqrt{B_2^2 - 4A_2(C_2 - X)}}{2A_2}, \tag{5.29}$$

where the plus solution has been chosen to ensure that $\xi \to X$ as $\tau \to 0$. Finally,

$$I_1 = \left[0, \lambda_1 + \frac{\lambda_1}{\bar{C}}(C_I - \bar{C})(1 - \exp(-\bar{C}\tau))\right], \tag{5.30}$$

$$I_2 = \left[\lambda_1 + \frac{\lambda_1}{\bar{C}}(C_I - \bar{C})(1 - \exp(-\bar{C}\tau)), 1 + (\lambda_2 - 1)\exp(-\bar{C}\tau)\right], \tag{5.31}$$

$$I_3 = \left[1 + (\lambda_2 - 1)\exp(-\bar{C}\tau), 1\right]. \tag{5.32}$$

Plugging into (5.9) gives $U(X, \tau)$ as

$$U(X,\tau) = \begin{cases} \dfrac{(C_I - \bar{C})\exp(-\bar{C})X}{1 + (1/\lambda)(1-\lambda)(1 - \exp(-\bar{C}\tau)} & \text{for} \quad X \in I_1, \\ \left(A_1\xi_2^2 + B_1\xi_2^2 + C_1\right)\exp(-\bar{C}\tau) & \text{for} \quad X \in I_2, \\ \bar{C}\,(1 - X) & \text{for} \quad X \in I_3, \end{cases} \tag{5.33}$$

as shown in figure 8 along with C found from (5.3), i.e.

$$C = \frac{\partial U}{\partial X} + \bar{C}. \tag{5.34}$$

Note that the interval I_2 does not shrink to 0 in time ($I_2 \to [\lambda_1 C_1/\bar{C}, 1]$ for $\tau \to \infty$), but the curvature around the right-hand end point grows without bound so that the limiting shape of the concentration profile again becomes a discontinuous Heaviside function.

5.2. *Results for large Münch number*

In the limit of large $M \gg 1$ we cannot neglect the pressure gradient along the channel and this term dominates the advective term in (4.9), i.e. the second derivative in U. Thus

$$\frac{\partial C}{\partial X} = -MU \tag{5.35}$$

$$\frac{\partial C}{\partial \tau} + \frac{\partial CU}{\partial X} = \bar{D}\frac{\partial^2 C}{\partial X^2} \tag{5.36}$$

giving the nonlinear diffusion equation

$$\frac{\partial C}{\partial \tau} = M^{-1}\frac{\partial}{\partial X}\left[C\frac{\partial C}{\partial X}\right] + \bar{D}\frac{\partial^2 C}{\partial X^2}. \tag{5.37}$$

If we neglect molecular diffusion the resulting universal nonlinear diffusion equation can be written as

$$\frac{\partial C}{\partial \tau} = M^{-1}\frac{\partial}{\partial X}\left[C\frac{\partial C}{\partial X}\right]. \tag{5.38}$$

This can be done as long as $M^{-1}C \gg \bar{D} \approx 10^{-5}$. If M becomes even larger normal diffusion will take over. Equation (5.38) belongs to a class of equations which have been studied, e.g. in the context of intense thermal waves by Zeldovich *et al.* and flow through porous media by Barenblatt (1996) in the 1950s. The Münch number M can be removed by rescaling the time according to $\tau = Mt$, so when M is large we get

very slow motion with a time scale growing linearly with M. Equation (5.38) admits scaling solutions of the form

$$C(X,\tau) = \left(\frac{\tau}{M}\right)^{\alpha} \Phi(\xi) \quad \text{with} \quad \xi = X\left(\frac{\tau}{M}\right)^{\beta} \tag{5.39}$$

as long as $\alpha + 2\beta + 1 = 0$. The total amount of sugar is, however, conserved. In our rescaled units

$$\int_0^1 C(X,\tau)\,\mathrm{d}X = \lambda, \tag{5.40}$$

where, as before, λ is the fraction of the tube initially containing the sugar. We can only hope to find a scaling solution in the intermediate time regime, where the precise initial condition has been forgotten, but the far end ($X = 1$) is not yet felt. Thus we can replace integral (5.40) with

$$\int_0^{\infty} C(X,\tau)\,\mathrm{d}X = \lambda \tag{5.41}$$

which implies that $\alpha = \beta = -1/3$ and

$$C(X,\tau) = \left(\frac{\tau}{M}\right)^{-1/3} \Phi(\xi) \quad \text{with} \quad \xi = X\left(\frac{\tau}{M}\right)^{-1/3}. \tag{5.42}$$

Inserting this form into (5.38), we obtain the differential equation for Φ

$$\frac{1}{2}\frac{\mathrm{d}^2\Phi^2}{\mathrm{d}\xi^2} + \frac{1}{3}\frac{\mathrm{d}(\xi\Phi)}{\mathrm{d}\xi} = 0 \tag{5.43}$$

which can be integrated once to

$$\Phi\frac{\mathrm{d}\Phi}{\mathrm{d}\xi} + \frac{1}{3}\xi\Phi = \text{constant}. \tag{5.44}$$

Due to the boundary condition $\partial C/\partial X = 0$ in the origin, the constant has to vanish and we find the solution

$$\Phi(\xi) = \frac{1}{6}(b^2 - \xi^2) \tag{5.45}$$

which is valid only for ξ smaller than the constant b. For $\xi > b$, Φ is identically 0. The fact that the solution – in contrast to the linear diffusion equation – has *compact support*, is an interesting characteristic of a large class of nonlinear diffusion equations (Barenblatt 1996). The value of b is determined by conservation integral (5.41) giving $\int_0^{\infty} \Phi\,\mathrm{d}\xi = 1$, and thus $b = (9\lambda)^{1/3}$.

The final solution thus has the form

$$C(X,\tau) = \begin{cases} \dfrac{M}{6\tau}((X_f(\tau))^2 - X^2) & \text{for} \quad X < X_f(\tau) = \left(9\lambda\dfrac{\tau}{M}\right)^{1/3} \\ 0 & \text{for} \quad X > X_f(\tau) \end{cases} \tag{5.46}$$

which shows that the sugar front moves as $X_f(\tau) \sim \tau^{1/3}$ and the concentration at the origin decays as $C(0,\tau) \sim \tau^{-1/3}$. To check the validity of this solution, also when the initial condition has support in a finite region near the origin, we plot $(\tau/M)^{1/3}C(X,\tau)$ against $\xi = X(\tau/M)^{-1/3}$ in figure 9(*c*). The corresponding solution for U is found from

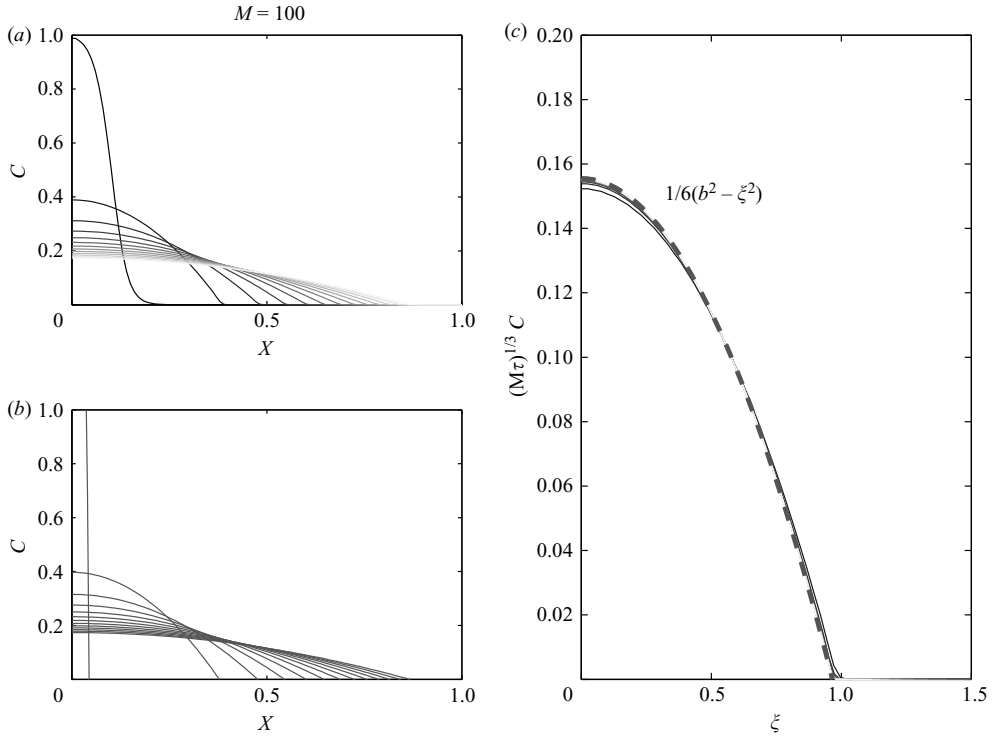

FIGURE 9. (*a*) Numerical simulation of (5.38) compared with (*b*) scaling solution (5.46) and (*c*) (5.45), which is shown as a dashed line. The initial condition has the form $C(X,0)=1-[1+\exp(-(X-\lambda)/\epsilon)]^{-1}$, where $\lambda=0.1$ and $\epsilon=2\times10^{-2}$ and the curves are equidistant in time. When λ controlling the size of the region of non-zero initial sugar concentration becomes larger, a more accurate scaling solution is found by letting $\tau\to\tau+\tau_0$ and treating τ_0 as an unknown parameter. In (*c*), we have omitted the first curve (the initial condition).

(5.35) as

$$U(X,\tau)=\begin{cases}\dfrac{X}{3\tau} & \text{for} \quad X<X_f(\tau)\\ 0 & \text{for} \quad X>X_f(\tau)\end{cases} \tag{5.47}$$

and $\partial^2U/\partial X^2=0$ justifying the neglect of $\partial^2U/\partial X^2$ in going from (4.9) to (5.35) for large M. It is seen that the velocity of the sugar front $X_f'(\tau)=(\lambda/(3M))^{1/3}\tau^{-2/3}$ is identical to $U(X_f(\tau),\tau)$ from (5.47).

6. Comparison between theory and experiment

In §§ 2.2 and 3.2, we have presented experiments demonstrating the movement of a sugar solution inside a membrane tube surrounded by a reservoir of water. We now wish to consider whether the theory is in agreement with the experimental results.

6.1. *Set-up I*

The plot in figure 10 shows the relative front position, $(L-x_f)/(L-l)$, plotted against time for five different experiments conducted with set-up I. The numbers 1–5 indicate the sugar concentrations used (cf. table 2). One clearly sees, that the relative front position approaches zero faster for high concentrations than for low. Typical

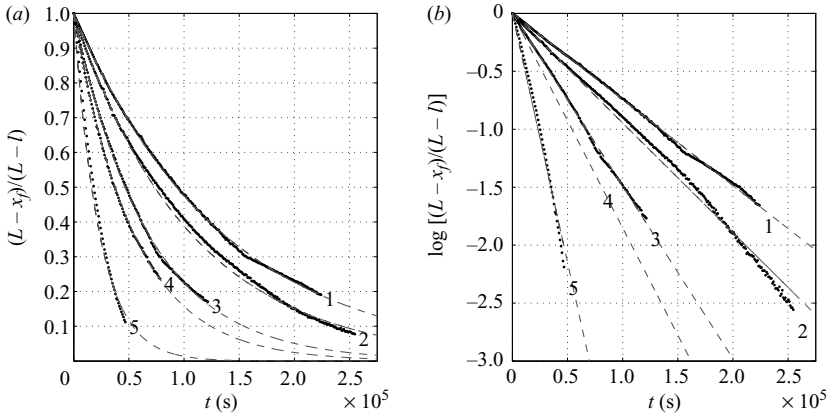

FIGURE 10. (*a*) Experimental (black dots) and fits to (5.22) for the relative front position versus time, shown as dashed lines. (*b*) Semi-logarithmic version of (*a*).

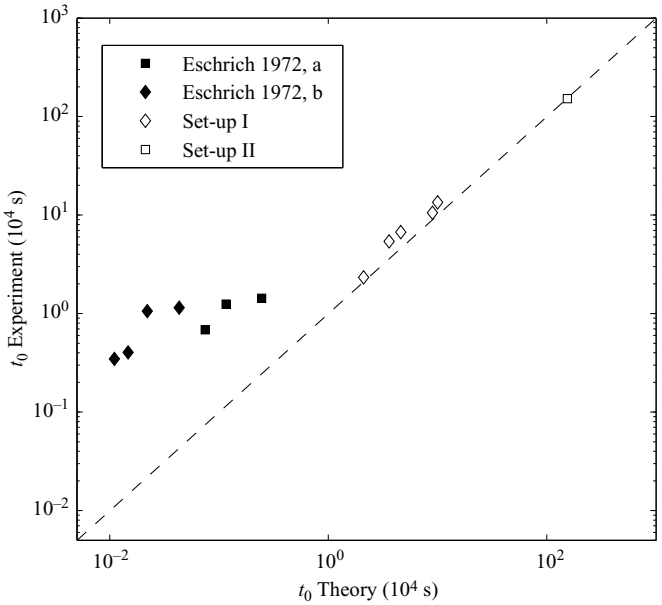

FIGURE 11. Our experimentally obtained values of t_0 plotted together with the results found by Eschrich *et al.* (1972). Data points marked with an 'a' represent results from closed tube experiments and points marked with a 'b' represent results from semi-closed experiments taken from figures 8 and 9 of the original paper.

values of M and $\bar{D}$ are $M \sim 10^{-8}$ and $\bar{D} \sim 10^{-5}$, so it is reasonable to assume that we are in the domain where the analytical solution for $M = \bar{D} = 0$ is valid. To test the result from (5.19) against the experimental data, the plot in figure 10 shows the logarithm of the relative front position plotted against time. For long stretches of time the curves are seen to approximately follow straight lines in good qualitative agreement with theory. The dashed lines are fits to (5.19), and we interpret the slopes as $-\frac{1}{t_0}$, the different values plotted in figure 11 against the theoretical values. The theoretically and experimentally obtained values of t_0 are in good quantitative

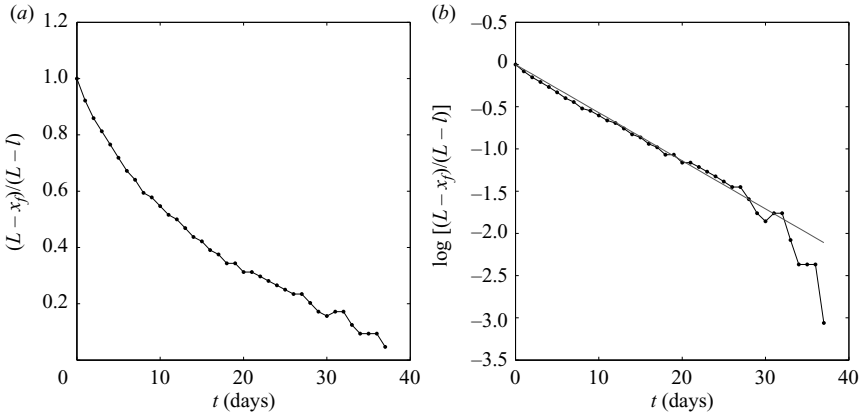

FIGURE 12. (*a*) Experimental data obtained using set-up II showing the relative front position (black dots) as a function of time. (*b*) Lin–log plot of the experimental data shown on the left. The solid line is a fit to (5.22) with $t_0 = 1.6 \times 10^6$ s.

agreement, within 10 %–30 %. Generally, theory predicts somewhat smaller values of t_0 than observed, implying that the observed motion of the sugar front is a little slower than expected from the pressure-flow hypothesis. Nevertheless, as can be seen in figure 11 these results are a considerable improvement to the previous results obtained by Eschrich *et al.* as we find much better agreement between experiment and theory.

6.2. *Set-up II*

The plot in figure 12 shows the relative front position, $(L - x_f)/(L - l)$, plotted against time for the experiment conducted with set-up I. On the semi-logarithmic plot, the curves are seen to follow straight lines in good qualitative agreement with the simple theory for $M = \bar{D} = 0$. As can be seen in figure 11, we also found very good quantitative agreement between the experiment and theory for set-up II.

To test how well the motion of the sugar front observed in the experiments with set-up II was reproduced by our model, we solved the equations of motion numerically starting with the initial conditions from figure 5. For $M = \bar{D} = 0$, the results are shown in figure 13(*b*). While the front positions are reproduced relatively well, the shape of the front is not, so diffusion must play a role. This can be seen in figure 13(*c*) which shows the result of simulation with $M = 10^{-9}$, $D = 6.9 \times 10^{-11}$ m^2 s^{-1}. Clearly, the model which includes diffusion reproduces the experimental data significantly better.

To study the shape of the front in greater detail, consider the plots in figure 13(*d–f*). Here the gradient of the concentration curves on the left in figure 13 is shown. In figure 13(*d*) we clearly see a peak moving from left to right while it gradually broadens and flattens. In figure 13(*e*) also we see the peak advancing, but the flattening and broadening is much less pronounced. In figure 13(*f*) we see that the model which includes diffusion reproduces the gradual broadening and flattening of the front very well.

7. Conclusion

In this paper we have studied osmotically driven transient pipe flows. The flows are generated by concentration differences of sugar in closed tubes, fully or partly

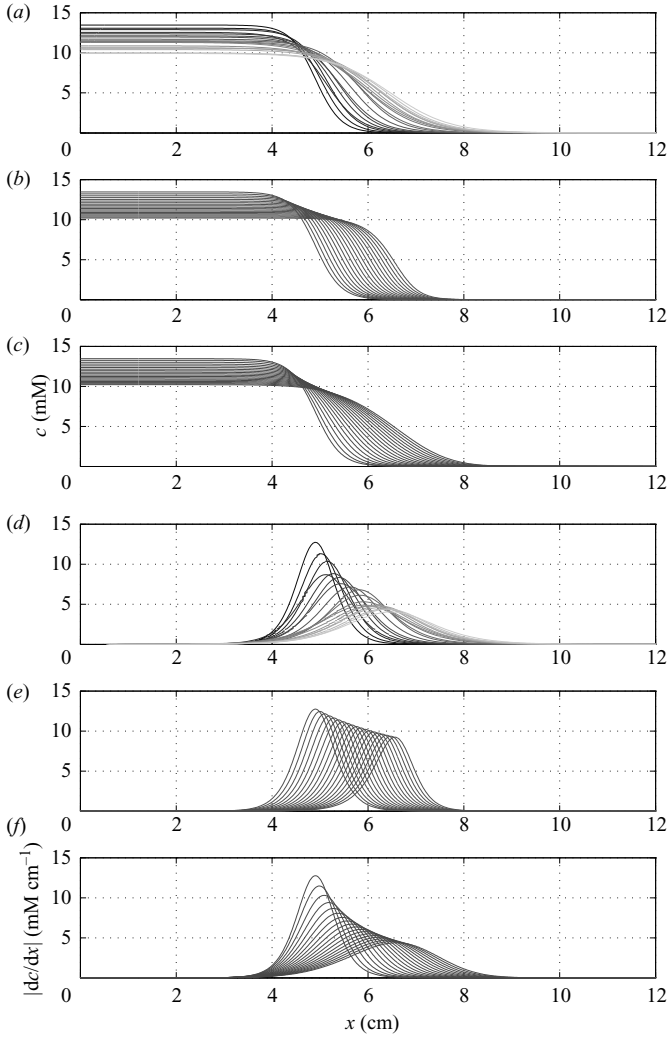

FIGURE 13. Results from set-up II showing the experimental data (a, d) and the numerical model for $M = D = 0$ (b, e) and for $M = 10^{-9}$, $D = 6.9 \times 10^{-11}$ m^2 s^{-1} (c, f).

enclosed by semi-permeable membranes surrounded by pure water. The flows are initiated by a large concentration in one end of the tube and we study the approach to equilibrium, where the sugar is distributed evenly within the tube. Experimentally, we have used two configurations: the first is an updated version of the set-up of Eschrich *et al.* where the flow takes place in a dialysis tube and the sugar is followed by introducing a dye. The advantage is the relatively rapid motion, due to the large surface area. The disadvantage is that the sugar concentration cannot be inferred accurately by this method and for this reason we have introduced our second set-up, where the sugar concentration can be followed directly by refraction measurements.

On the theoretical side, we first re-derive the governing flow equations and introduce the dimensionless Münch number M. We then show that analytical solutions can be obtained in the two important limits of very large and very small M. In the general case we show how numerical methods based on Green's functions are very effective.

Finally, we compare theory and experiment with very good agreement. In particular the results or the velocity of the front (as proposed by Eschrich *et al.*) can be verified rather accurately.

Concerning the application to sap flow, the quantitative study we performed leads to the following conclusions: for a large tree it seems improbable that sugar transport, e.g. from leaf to root by this sole passive mechanism would be sufficiently efficient. In this case active transport processes might play an important role. On the other hand, transport over short distances, e.g. locally in leaves or from a leaf to a nearby shoot might be more convincingly described by the pressure-flow hypothesis.

It is a pleasure to thank Francois Charru, Marie-Alice Goudeau-Boudeville, Herv Cochard, Pierre Cruiziat, Alexander Schulz, N. Michele Holbrook and Vakhtang Putkaradze for many useful discussions. Much appreciated technical assistance was provided by Erik Hansen. This work was supported by the Danish National Research Foundation, Grant No. 74.

Appendix A. Materials: sugar and membrane

A.1. *Sugar*

The sugar used was a dextran (Sigma-Aldrich, St Louis, MO, USA, type D4624) with an average molecular weight of 17.5 kDa. The dye used was a red fruit dye (Flachsmann Scandinavia, Rød Frugtfarve, type 123000) consisting of an aqueous mixture of the food additives E-124 and E-131 with molecular weights of 539 Da and 1159 Da, respectively (PubChem-Database 2007). Even though the molecular weights are below the MWCO of the membrane, the red dye was not observed to leak through the membrane. This, however, was observed when using another type of dye, Methylene blue, which has a molecular weight of 320 Da.

A.2. *Membrane*

The membrane used in both set-ups was a semi-permeable dialysis membrane tube (Spectra/Por Biotech cellulose ester dialysis membrane) with a radius of 5 mm, a thickness of 60 μm and a MWCO (molecular weight cut off) of 3.5 kDa. The permeability L_p was determined by applying a pressure and measuring the flow rate across the membrane

$$L_p = (1.8 \pm 0.2) \times 10^{-12}\,\mathrm{m\ (Pa\,s)^{-1}}. \tag{A 1}$$

A.3. *Osmotic strength of dextran*

Figure 14(left) shows the relation between dextran concentration and osmotic pressure found from the experiments shown in figure 3. A linear fit gives

$$\Pi = (0.1 \pm 0.01\ \mathrm{bar\ mM^{-1}})c \tag{A 2}$$

where Π has unit bar, and c is measured in mM. This is in good agreement with values given by Jonsson (1986).

Appendix B. Numerical methods for non-zero M and $\bar{D}$

For non-zero values of M and $\bar{D}$, the equations of motion,

$$\frac{\partial^2 U}{\partial X^2} - MU = \frac{\partial C}{\partial X} \tag{B 1}$$

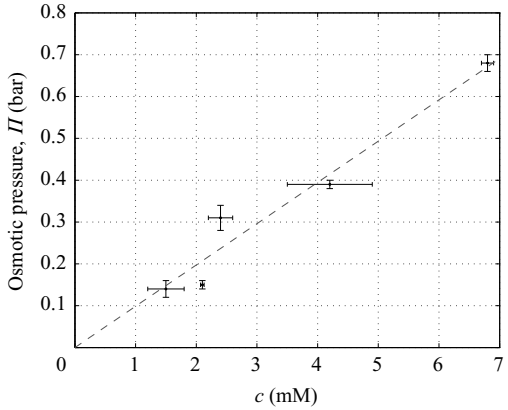

FIGURE 14. van't Hoff relation for 17.5 kDa dextran.

and

$$\frac{\partial C}{\partial \tau} + \frac{\partial CU}{\partial X} = \bar{D}\frac{\partial^2 C}{\partial X^2} \tag{B 2}$$

cannot be solved analytically. However, they can be written as a single integro-differential equation, which is straightforward to solve on a computer. If we choose a set of linear boundary conditions, $B_X[U] = a_i$, for (B 1), the solution can be written as

$$U = \int_0^1 G(X,\xi)\frac{\partial C}{\partial \xi}\mathrm{d}\xi + U_2. \tag{B 3}$$

Here, $G(X,\xi)$ is the Green's function for the differential operator $\partial^2/\partial X^2 - M$ with boundary conditions $B_X[U] = 0$ and U_2 fulfils the homogeneous version of (B 1) with $B_X[U] = a_i$. Plugging this into (B 2) yields

$$\frac{\partial C}{\partial \tau} + \frac{\partial}{\partial X}\left(C\left(\int_0^1 G(X,\xi)\frac{\partial C}{\partial \xi}\mathrm{d}\xi + U_2\right)\right) = \bar{D}\frac{\partial^2 C}{\partial X^2}. \tag{B 4}$$

For the closed tube, i.e. for the boundary conditions $U(0,\tau) = U(1,\tau) = 0$, $G(X,\xi)$ is given by

$$G(X,\xi) = \begin{cases} -\dfrac{\sinh(a(1-X))}{a\sinh a}\sinh a\xi & \text{for} \quad \xi < X, \\ -\dfrac{\sinh aX}{a\sinh a}\sinh(a(1-\xi)) & \text{for} \quad \xi > X, \end{cases} \tag{B 5}$$

and $U_2 = 0$. To increase numerical accuracy, it is convenient to transform (B 4) by defining

$$\frac{\partial f}{\partial X} = C - \bar{C} \tag{B 6}$$

and choosing $f(0) = f(1) = 0$ such that $f(X) = \int_0^X (C - \bar{C})\mathrm{d}\xi$. Inserting in (B 4), we get

$$\frac{\partial f}{\partial t} = \bar{D}\frac{\partial^2 f}{\partial X^2} - \left(f(X) - \int_0^1 \frac{\partial K(X,\xi)}{\partial \xi} f(\xi)\mathrm{d}\xi\right)\left(\frac{\partial f}{\partial X} + \bar{C}\right), \tag{B 7}$$

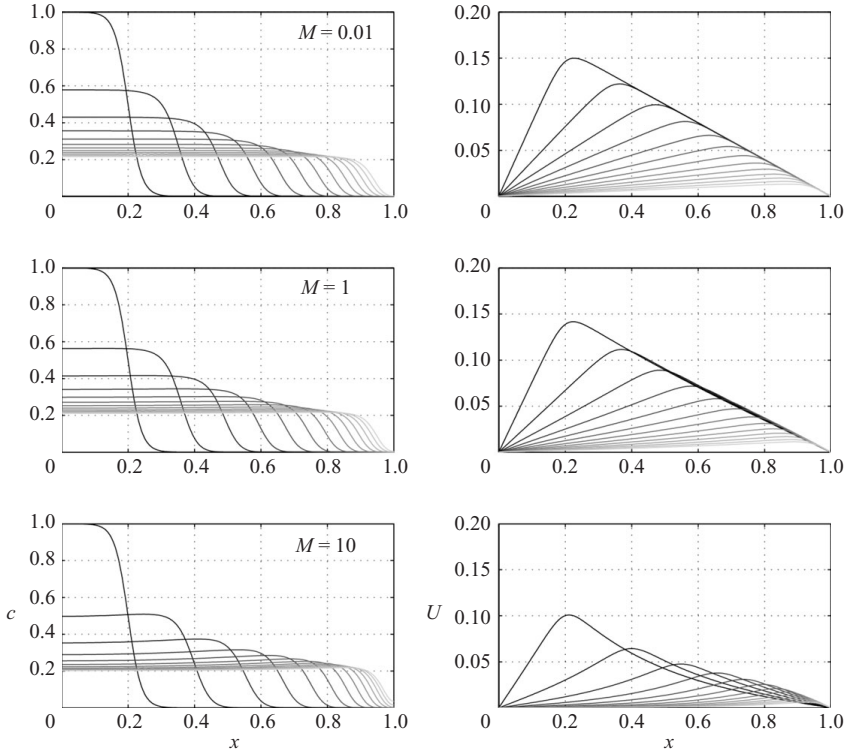

FIGURE 15. Results of numerical simulation of (B 4) using the boundary conditions $U(0,\tau)=U(1,\tau)=0$ for different values of M. $\bar{D}$ is kept constant at 10^{-5}. The initial condition was $C(X,0)=1-1/(1+\exp(-(X-\lambda)/\epsilon))$ where $\lambda=0.2$ and $\epsilon=2\times10^{2}$.

where

$$\frac{\partial K(X,\xi)}{\partial \xi}=\begin{cases}-a\dfrac{\sinh(a(1-X))}{\sinh a}\sinh a\xi & \text{for} \quad \xi < X,\\ -a\dfrac{\sinh aX}{\sinh a}\sinh(a(1-\xi)) & \text{for} \quad \xi > X.\end{cases} \tag{B 8}$$

To solve (B 7) we used MATLAB's built-in time solver `ode23t` which is based on an explicit Runge–Kutta formula along with standard second-order schemes for the first- and second-order derivatives. For the spatial integration, the trapezoidal rule was used (Press 2001). Results of a numerical simulation for different values of M are shown in figure 15.

REFERENCES

BARENBLATT, G. I. 1996 *Scaling, Self-Similarity, and Intermediate Asymptotics*. Cambridge University Press.

ESCHRICH, W., EVERT, R. F. & YOUNG, J. H. 1972 Solution flow in tubular semipermeable membranes. *Planta(Berl.)* **107**, 279–300.

FRISCH, H. L. 1976 Osmotically driven flow in narrow channels. *Trans. Soc. Rheol.* **20**, 23–27.

GURBATOV, S. N. MALAKHOV, A. N. & SAICHEV, A. I. 1991 *Nonlinear Random Waves and Turbulence in Nondispersive Media: Waves, Rays, Particles*. Manchester University Press.

Henton, S. M. 2002 Revisiting the Münch pressure-flow hypothesis for long-distance transport of carbohydrates: modelling the dynamics of solute transport inside a semipermeable tube. *J. Exp. Bot.* **53**, 1411–1419.

Jonsson, G. 1986 Transport phenomena in ultrafiltration: membrane selectivity and boundary layer phenomena. *J. Pure Appl. Chem.* **58**, 1647–1656.

Jensen, K. H. 2007 Osmotically driven flows and their relation to sugar transport in plants. MSc Thesis, The Niels Bohr Institute, University of Copenhagen.

Knoblauch, M. & van Bel, A. J. E. 1998 Sieve tubes in action. *The Plant Cell* **10**, 35–50.

Landau, L. D. & Lifshitz, E. M. 1980 *Statistical Physics*. Pergamon Press.

Münch, E. 1930 *Die Stoffbewegung in der Pflanze*. Verlag von Gustav Fisher.

Niklas, K. J. 1992 *Plant Biomechanics – An Engineering Approach to Plant Form and Function*. The University of Chicago Press.

Nobel, P. S. 1999 *Physicochemical & Environmental Plant Physiology*. Academic Press.

Pedley, T. J. 1983 Calculation of unstirred layer thickness in membrane transport experiments: a survey. *Quart. Rev. Biophys.* **16**, 115–150.

Press, W. H. 2001 *Numerical Recipes in Fortran 77*, Vol. 1 Cambridge University Press.

PubChem–Database 2007 http://pubchem.ncbi.nlm.nih.gov/ *National Library of Medicine*

Schultz, S. G. 1980 *Basic Principles of Membrane Transport*. Cambridge University Press.

Taiz, L. & Zeiger, E. 2002 *Plant Physiology*. Sinauer Associates.

Thompson, M. V. & Holbrook, N. M. 2003*a*, Application of a single-solute non-steady-state phloem model to the study of long-distance assimilate transport. *J. Theor. Biol.* **220**, 419–455.

Thompson, M. V. & Holbrook, N. M. 2003*b*, Scaling phloem transport: water potential equilibrium and osmoregulatory flow. *Plant, Cell Environ.* **26**, 1561–1577.

Weir, G. J. 1981 Analysis of Münch theory. *Math. Biosci.* **56**, 141–152.

The Danish Polymer Centre
Department of Chemical and Biochemical Engineering
Technical University of Denmark
Søltofts Plads, Building 227
DK-2800 Kgs. Lyngby
Denmark

Phone: +45 4525 6801
Web: www.dpc.kt.dtu.dk

ISBN : 978-87-92481-75-7